UNIVERSIDADE DE BRASÍLIA – UNB
FACULDADE DE TECNOLOGIA / FACULDADE DO GAMA

PROGRAMA DE PÓS-GRADUAÇÃO EM INTEGRIDADE DE MATERIAIS DA ENGENHARIA

EXPERIMENTAL INVESTIGATION OF TURBULENT FLOW AND HEAT TRANSFER AROUND A SINGLE ROD FOR DIFFERENT ROD-WALL SPACINGS

FÁBIO MATOS KAYSER

ORIENTADOR: PROF. DR. JHON NERO VAZ GOULART

COORIENTADOR: PROF. PHD. MOHAMED SADOK GUELLOUZ

UNIVERSIDADE DE BRASÍLIA – UNB

FACULDADE DE TECNOLOGIA / FACULDADE DO GAMA

EXPERIMENTAL INVESTIGATION OF TURBULENT FLOW AND HEAT TRANSFER AROUND A SINGLE ROD FOR DIFFERENT ROD-WALL SPACINGS

FÁBIO MATOS KAYSER

ORIENTADOR: PROF. DR. JHON NERO VAZ GOULART

COORIENTADOR: PROF. PHD MOHAMED SADOK GUELLOUZ

DISSERTAÇÃO DE MESTRADO EM

INTEGRIDADE DE MATERIAIS DA ENGENHARIA

PUBLICAÇÃO: 098A/2021

BRASÍLIA/DF, NOVEMBRO DE 2021

UNIVERSIDADE DE BRASÍLIA - UNB

FACULDADE DE TECNOLOGIA / FACULDADE DO GAMA

PROGRAMA DE PÓS-GRADUAÇÃO EM INTEGRIDADE DE MATERIAIS DA ENGENHARIA

EXPERIMENTAL INVESTIGATION OF TURBULENT FLOW AND HEAT TRANSFER AROUND A SINGLE ROD FOR DIFFERENT ROD-WALL SPACINGS

FÁBIO MATOS KAYSER

DISSERTAÇÃO DE MESTRADO SUBMETIDA AO PROGRAMA DE PÓS-GRADUAÇÃO EM INTEGRIDADE DE MATERIAIS DA ENGENHARIA DA FACULDADE DE TECNOLOGIA DA UNIVERSIDADE DE BRASÍLIA, COMO PARTE DOS REQUISITOS NECESSÁRIOS PARA A OBTENÇÃO DO GRAU DE MESTRE.

APROVADA POR:

PROF. DR. JHON NERO VAZ GOULART, UNB
(ORIENTADOR)

DR. MARCUS VINICIUS GIRÃO DE MORAIS, UNB
(EXAMINADOR INTERNO)

PROF. DR. LUIZ ALBERTO ROCHA, UNISSINOS
(EXAMINADOR EXTERNO)

BRASÍLIA/DF, NOVEMBRO DE 2021

FICHA CATALOGRÁFICA

MATOS KAYSER, FÁBIO
EXPERIMENTAL INVESTIGATION OF TURBULENT FLOW AND HEAT TRANSFER AROUND A SINGLE ROD FOR DIFFERENT ROD-WALL SPACINGS [Distrito Federal], 2021.
xvii, 119p. 210 x 297 mm (FGA/FT/UnB, Mestre, Integridade de Materiais da Engenharia, 2020).
Dissertação de Mestrado – Universidade de Brasília. Faculdade de Tecnologia.
Faculdade do Gama.
1. Heat Transfer 2. Coherent Structures
3. Rod Bundles 4. Hot-wire Anemometry
5. Reynolds-Colburn Analogy
I. FGA/FT/UnB II. Mestre (série)

Referência
Matos Kayser, Fábio (2021). EXPERIMENTAL INVESTIGATION OF TURBULENT FLOW AND HEAT TRANSFER AROUND A SINGLE ROD FOR DIFFERENT ROD-WALL SPACINGS. Dissertação de mestrado em Integridade de Materiais da Engenharia, Publicação 098A/2021, Programa de Pós-Graduação, Faculdade de Tecnologia, Universidade de Brasília, Brasília, DF, 119p.

Cessão de Direitos

Autor: Fábio Matos Kayser

Título: EXPERIMENTAL INVESTIGATION OF TURBULENT FLOW AND HEAT TRANSFER AROUND A SINGLE ROD FOR DIFFERENT ROD-WALL SPACINGS.

Grau: Mestre

Ano: 2021

---

fabio_mk_66@hotmail.com

Brasília, DF – Brasil

At first, to God, for the opportunity.

To my mother, for giving me support and strength to carry on.

AKNOWLEDGEMENTS

To God, for providing me this amazing opportunity and allowing me to conclude it.

To my mother, Regina, for advising me, supporting me and for being by my side to overcome all challenges that I have in my life.

To my lovely girlfriend, Camila, for staying right by my side no matter what happen, for believing me and for encouraging me to become a better person.

To my friend, Gilvan, for all the supporting words.

To Alexandre Alencar de Melo for his extremely important support during the experiments.

To my advisor, Prof. Dr. Jhon Nero Vaz Goulart, and to my coadvisor, Prof. PhD Mohamed Sadok Guellouz, for the trust, for the patience, for the understanding, for spending a lot of their time helping me and sharing their extensive knowledge.

To all the friends of GMEC and from other groups that I have met during this journey.

Also, I would like to thanks CAPES and FAP-DF for the financial support.

ABSTRACT

Turbulent flows through rod bundles or compound channels are characterized by the presence of large-scale structures that transport energy and momentum and can strongly affect the mixing and the heat transfer in the subchannels. This kind of turbulent structures can be identified by instabilities in the fluctuation quantities of the flow and by energy peaks with a characteristic frequency in the spectral analysis. Turbulent flows in rod bundles or compound channels are mainly seen in nuclear reactors and heat exchangers and even, in open channels with lateral floodplains. In this sense, the appropriate understanding of the large-scale motions in the mentioned channels is important to correctly predict the heat transfer and possible structural consequences generated by the flow inducing vibration.

The present work aims to experimentally assess the influence of the W/D - ratio on the flow dynamics and the convective heat transfer in a compound rectangular channel containing a single cylindrical rod with both sides closed. W is the sum between the rod's diameter and the gap width, D is the rod's diameter. The rod is heated locally by a specially design cell powered by a cartridge resistance. A single hot-wire anemometry probe was employed to gather the data of mean average velocity, velocity fluctuation and spectra. The heat transfer coefficients were determined by using the temperature measured by thermocouples at the heated cell surface. The local skin friction coefficient was measured around the rod by a Preston tube and employed to verify the Reynolds-Colburn analogy. The experiments were performed for a Reynolds number, Re_{Dh}, around 40000 and the dimensionless gap spacings W/D = 1.050, 1.100, 1.150 and 1.200.

The mean velocity isocontours were very similar in shape to those observed in the previous literature. The lower values, of these quantities, were found near the gap vicinity and the highest are in the subchannel center. For W/D = 1.050, 1.100 and 1.200 the maximum mean veleocity was $\bar{U}/Ub$ = 1.30. In the case of W/D = 1.150, the maximum mean axial velocity was $\bar{U}/Ub$ = 1.20, a little bit lower in comparison to the other gaps. The u-RMS presented their highest values in the gap vicinity and lowest in the wider region of the channel.

The spectral density and autocorrelation functions evaluated in the vicinity of the gap indicate that the flow dynamics in the lowest gaps (W/D = 1.050 and 1.100) is under strong influence of large-scale coherent structures, as observed through the pronounced peaks in the spectra and the oscillations in the autocorrelation function up to the position z/D = 0.30.

For the closed rod, the obtained Strouhal number was higher than the literature values. However, when a new experimental campaign was carried out using a hollow rod the obtained frequency and the Strouhal number are in quite good agreement with the open literature.

The temperature and the Nusselt number distributions were similar to those presented by previous authors. The lowest value for the Nusselt number was found in the gap vicinity. As *W*/*D* became wider, the location of the minimum Nusselt number became closer to the narrow gap. The location of the minimum convection in the channel seems to be influenced by the coherent structures. The heat transfer was also assessed by determining the *J*-factor, which presented good agreement with the experimental results found in the literature.

It was observed that the values of the skin friction coefficient strongly change as the *W*/*D* – ratio increases and has almost the same distribution of the Nusselt number. The Reynolds-Colburn analogy showed a linear behaviour, regardless the *W*/*D* ratio. The analogy can be used as an alternative way to determine the heat transfer coefficient.

Keywords: Heat Transfer, Coherent Structures, Rod Bundles, Hot-wire anemometry, Reynolds-Colburn Analogy.

RESUMO

Escoamentos turbulentos através de feixes de tubos ou canais compostos são caracterizados pela presença de estruturas de grande escala que transportam energia e momento, podendo afetar significamente o processo de mistura e a transferência de calor nos subcanais. Esse tipo de estrutura turbulenta pode ser identificada por instabilidades na flutuação de certas variáveis do escoamento e por picos de energia com uma frequencia característica na análise espectral. Escoamentos turbulentos em feixes de tubos ou canais compostos são vistos principalmente em reatores nucleares e trocadores de calor e, ainda, em canais abertos com margens laterais. Nesse sentido, o entendimento apropriado dos movimentos de grande escala nos canais mencionados é importante para corretamente predizer a transferência de calor e possíveis consequencias estruturais geradas por vibrações induzidas pelo escoamento.

O presente trabalho almeja avaliar experimentalmente a influência da razão *W*/*D* na dinâmica do escoamento e na transferência de calor por convecção em um canal composto rectangular que contém um tubo cilindrico com os lados fechados. *W* é soma entre o diâmetro do tubo e a largura da fenda, *D* é o diâmetro do tubo. O tubo é aquecido localmente por uma célula alimentada por uma resistência cartucho. Uma sonda simples de anemometria de fio quente foi empregada para adquirir a valocidade media, flutuação de velocidade e espectro. Os coeficientes de transferência de calor foram determinados a partir de temperaturas medidas por termopares na superfície da célula aquecida. O coeficiente de atrito local foi medido em volta do tubo por um tubo de Preston e a partir desse resultado foi possível avaliar a analogia de Reynolds-Colburn. Os experimentos foram realizados para um número de Reynolds, Re_{Dh}, em torno de 40000 e para as larguras adimensionais de fenda *W*/*D* = 1.050, 1.100, 1.150 and 1.200.

Os contornos de velocidade média apresentaram formas similares às observadas na literatura. Os menores valores foram encontrados próximos à região da fenda e os maiores estão na parte central do subcanal. Para *W*/*D* = 1.050, 1.100 and 1.200 a máxima velocidade media foi de $\bar{U}/Ub$ = 1.30. No caso de *W*/*D* = 1.150, o valor máximo de velocidade axial foi $\bar{U}/Ub$ = 1.20, um pouco menor em comparação as outras fendas. O *u*-RMS apresentou seus maiores valores na região da fenda e os menores na região mais larga do canal.

As funções de densidade espectral e autocorrelação avalidas na região da fenda indicam que a dinâmica do escoamento nas menores fendas (*W*/*D* = 1.050 and 1.100) está sob

forte influência de estruturas coerentes de grande escala, conforme observado através dos picos no espectro e das oscilações na função de autocorrelação até a posição z/D = 0.30. Para o tubo fechado, o número de Strouhal obtido foi maior do que os valores encontrados na literatura. Contudo, quando um novo experimento foi realizado usando um tubo vazado, a frequência e o número de Strouhal obtidos se mostraram de acordo com o encontrado na literatura.

As distribuições de temperatura e de numero de Nusselt foram similares ao apresentado por autores anteriores. O menor valor de número de Nusselt foi encontrado na região da fenda. Ao passo que W/D aumenta, o local de menor número de Nusselt fica mais próximo da fenda estreita. O local em que a convecção é minima parace ser influenciado pelas estruturas coerentes. A transferência de calor também foi avaliada por meio da determinação do J-factor, o qual se mostrou de acordo com os resultados experimentais encontrados na literatura.

Foi observado que os valores do coeficiente de atrito mudam substancialmente conforme a razão W/D aumenta e apresentam quase a mesma distribuição do número de Nusselt. A analogia de Reynolds-Colburn mostrou um comportamente linear, independente da razão W/D. A analogia pode ser usada como uma forma alternativa para determiner o coeficiente de transferência de calor.

Palavras-chave: Transferência de Calor, Estruturas Coerentes, Feixe de Tubos, Anemometria de Fio Quente, Analogia de Reynolds-Colburn.

CONTENTS

LIST OF TABLES

LIST OF FIGURES

LIST OF NOMENCLATURES AND ABBREVIATIONS

DES	Detached Eddy Simulation.
LES	Large Eddy Simulation.
PIV	Particle Image Velocimetry.
PSD	Power Spectra Density [(m^2/s)]
RMS	Root Mean Square
RSM	Reynolds Stress Model
URANS	Unsteady Reynolds-Average Navier-Stokes

LIST OF SYMBOLS

A_c	Cell surface exposed to convective heat transfer [m^2].
A_t	Area of the half channel's cross section [m^2]
A_V	Small area in the channel's cross section [m^2]
C_f	Skin friction coefficient [Dimensionless]
d, S	Gap width [mm]
d_p	Preston's tube diameter [mm]
D	Rod or tube diameter [mm]
D_h	Hydraulic diameter [mm]
D_i	Inner tube's diameter [mm]
ΔP	Pressure drop [Pa]
ΔP^+	Normalized pressure drop [Pa]
e	Eccentricity [mm]
f	Main/Characteristic/Fundamental frequency [Hz]
h	Heat transfer coefficient [W/m^2K]
h_ϕ	Heat transfer coefficient around the rod [W/m^2K]
$\bar{h}_{bundle}$	Average heat transfer coefficient around a tube [W/m^2K]
$\bar{h}_{\min}$	Minimal heat transfer coefficient around a rod [W/m^2K]
$\bar{h}_{tube}$	Heat transfer coefficient around a circular tube [W/m^2K]
Hc	Rectangular channel cross section height [mm]
I	$\frac{\bar{h}_{bundle}}{\bar{h}_{tube}}$ [Dimensionless]
J	$\frac{\bar{h}_{\min}}{\bar{h}_{bundle}}$ [Dimensionless]
k_{tb}	Thermal blanket thermal conductivity [W/mK]
k^+	Dimensionless turbulent kinetic energy [Dimensionless]
L_{tb}	Thermal blanket thickness [mm]
Nu	Nusselt number [Dimensionless]
P	Pitch [mm]
$P_{xx(f)}$	Power spectral densities function [m^2/s]

p	Gap depth [*mm*]
q_L	Conduction heat loss [*W*]
q_{conv}	Convective heat transfer [*W*]
q_f	Total heat provided by the electrical font [*W*]
r	Locus of a velocity for a specific angular position [*m*]
R_{tb}	Resistance between the thermal blanket and the heated cell [*K/W*]
R_{conv}	Convective resistance [*K/W*]
Re_{Dh}	Reynolds number based on the hydraulic diameter [Dimensionless]
R_{min}	Locus of the minimum velocity for a determined angular position [*m*]
R_{max}	Locus of the maximum velocity for a determined angular position [*m*]
St	Strouhal number [Dimensionless]
Stn	Stanton number [Dimensionless]
T_b	Bulk temperature [°*C*, *K*]
T_∞	Fluid temperature [°*C*, *K*]
$T_{(1\text{-}S)}$	Cell surface temperature [°*C*, *K*]
$T_{(2\text{-}RS)}$	Right side temperature [°*C*, *K*]
$T_{(3\text{-}LS)}$	Left side temperature [°*C*, *K*]
$T_{(4\text{-}F)}$	Frontal temperature [°*C*, *K*]
$T_{(5\text{-}I)}$	Temperature at the thermal blanket bottom [°*C*, *K*]
U	Mean axial velocity [*m/s*]
U_b	Bulk velocity [*m/s*]
U_{bL}	Local bulk velocity [*m/s*]
U_c	Transport velocity/ Convective velocity [*m/s*]
U_{max}	Maximum valocity for a determined angular position [*m/s*]
U_{ref}	Reference velocity [*m/s*]
U_V	Velocity in the center of a small area in the channel’s cross section [*m/s*]
u	Velocity axial componente [*m/s*]
uu^+	x-normal Reynolds stress [Dimensionless]
u^*	Friction velocity [*m/s*]
W	Sum of rod diameter and gap width [*mm*]
Wc	Rectangular channel cross section width [*mm*]
Y	Dimensionless mixing factor [Dimensionless]

GREEK LETTERS

δ	Mixing layer thickness [*m*]
Δ	Variation [Dimensionaless]
ε	Dissipation hate [m^2/s^3]
λ	Length of one period of large-scale oscillation [*m*]
ν	Kinematic viscosity [m^2/s]
θ, Φ	Azimuthal position [*degrees*]
τ_w	Wall shear stress [N/m^2]
τ^+	Normalized wall shear stress [Dimensionless]
Ψ	Dimensionless power spectra density [Dimensionless]

OTHER NOTATION

$(\bar{\ })$	Average quantity
$(\ )'$	Fluctuation quantity

1 INTRODUCTION

The cores of nuclear reactors, in general, are formed by clusters of fuel rods in a flow tube with a coolant fluid moving through the subchannels formed between the rods (Wu and Trupp, 1994). In this kind of arrangement, distinct flow phenomena occur due to the fact that the cross-section of these rod-bundles presents adjacent wide and narrow flow regions. Normally, rod bundles consist of compound channels, which are characterized by a main channel containing subchannels interconnected by gaps (Goulart et al., 2016; Melo et al., 2017). According to Guellouz and Tavoularis (2000a), the flows through compound channels are characterized by large-scale, quasi-periodic, flow structures and by a distribution of turbulent stresses not found in more simple geometries.

Hoffman (1964) was the first researcher to visualize wave-like large-scale structures in a 7-rod heated bundle. Van der Ros and Bogaardt (1970) verified by using thermocouples in their experiments in a geometry constituted by two square channels connected by a gap, that these wave structures showed a very regular pattern in amplitude and frequency for regions inside the gap. In the following years, Rowe performed experimental measurements of axial velocity, turbulence intensity and autocorrelation functions in a rod array parallel to the flow (Rowe, 1973; Rowe et al., 1974). The author observed large-scale vortices crossing the subchannels and verified that the scale, intensity and frequency of these structures increased as the rod spacing reduced. The frequencies and amplitudes of these large-scale structures, for different rod bundle geometries, have been measured by many authors during the years e.g. Hooper and Rehme (1984); Möller (1991); Guellouz and Tavoularis (2000a,b); Goulart et al., (2014, 2016); Melo et al., (2017); Candela et al., (2020).

The secondary flows were considered as a possible cause of the higher heat transfer and more uniform flow velocities in the narrow gaps, but this hypothesis was rejected by the experimental works presented by Trupp and Azad (1975); Carajilescov and Todreas (1976); Hooper (1980); Hooper and Rehme (1984). Now, it is accepted that the energy transport and flow dynamics in narrow gaps are

associated with large-scale turbulent structures, that can be termed as coherent structures (Chang and Tavoularis, 2005 and 2007). The large-scale structures have a remarkable influence on the mixing rate and on the heat transfer in a rod bundle (Möller, 1992; Guellouz and Tavoularis, 1992; Krauss and Meyer, 1998).

The scientific community has dedicated, for a long time, a lot of effort in order to properly understand the heat transfer process in channels with different geometries. The security and efficiency of engineering systems constituted by compound channels or rod-bundles, such as nuclear reactors and combustion engines, depend on the good knowledge on the heat transfer process involved.

In the 30th, Dittus and Boelter (1930) and Sieder and Tate (1935) assessed the heat transfer in annular tubes. However, at that time, the effects of large-scale structures in the narrow regions were not taken into account. Later, Palmer and Swanson (1961) and Hoffman et al., (1970) performed experimental study of the flow characteristics and the heat transfer i.e. the variation of the local and overall Nusselt numbers, in a seven-rod cluster. They also assessed variables like velocity distribution and friction factor, but did not correlate the heat transfer to turbulent structures in the narrower regions.

In the late seventies and early eighties, some efforts were directed to properly understand the heat transfer in narrow gaps. In that sense, Seale (1979) assessed analytically and experimentally the turbulent diffusion and secondary flow between subchannels in four-rod cluster. The author found that the temperature distribution in the center of the channels is not associated with secondary flows, but more likely to the high mixing rates due to the strong anisotropy in narrow gaps. Starting from these ideas, Seale (1981) concluded that the influence of the subchannel geometry on the heat transfer is directly related to the anisotropic effective diffusivities.

In the early nineties, Meyer (1991) was the first to study the turbulence and heat flux in a heated hexagonal 37-rod bundle. But, considering the previous published works, he could only compare his results to flow in tubes and unheated rod-bundles. One year later, Guellouz and Tavoularis (1992) studied heat transfer in a CANDU type (circular) 37-rod bundle and brought important statements. The authors concluded that the mixing process and the heat transfer are enhanced by the turbulent convection transport mechanism, which is associated with large-scale

eddies of the size of the geometric characteristic length and is of non-gradient type. Later Krauss and Meyer (1996,1998) assessed the turbulent flow and heat transfer in the 37-rod bundle with focus on specific regions of the channel.

Chang and Tavoularis (2006,2008) conducted numerical simulations in a rectangular channel containing a single rod by solving the unsteady Reynolds-Averaged Navier-Stokes with a Reynolds stress model. They found significant influence of the coherent vortical structures in heat transfer in a rod-wall gap region and the relationship between temperature fluctuation and the gap width. These findings were in agreement with the experimental works made during the previous decades for many kinds of channels' geometries.

The turbulent flow in rod-bundles is characterized by the influence of the gap spacing on the flow dynamics and on the heat transfer. Considering all the efforts of many researchers during the years who seek a wide understanding about the implications of the turbulent flow on the heat transfer in rod-bundles, the present work will discuss about some differences between a rectangular channel containing a closed and hollow rod in terms of spectral analysis and determine the Reynolds-Colburn analogy using local bulk velocities. For this, hot-wire anemometry was employed as flow measurement technique and a specially designed and home-made heated cell was totally built in our lab.

2 OBJECTIVES

The main objective of this work is to investigate the influence of the *W*/*D* spacing on the flow dynamics and on the convective heat transfer in a rectangular channel containing a single rod.

2.1 Specific Objectives

- Build a heated cell, powered by an electric cartridge resistance, to heat the rod suspended in the channel.
- Determine the heat losses from the heated cell that is not convected and therefore does not contribute to the Nusselt number calculation.
- Assess the mean average axial velocity and *u*-RMS in channel and its relationship with the relative gap spacing.
- Verify the frequency response of the large motion in terms of Strouhal numbers, comparing them to the open literature of the problem.
- Discuss about the difference between a rectangular channel containing a closed and hollow rod in terms of spectral analysis.
- Assess the Nusselt number between the rod's surface and the flow, turning the rod from 0° (narrow gap) up to 90° (wider gap).
- Perform experimental measurements of the local skin friction around the rod.
- Investigate the Reynolds-Colburn analogy for all *W*/*D* – ratio.

3 BIBLIOGRAPHIC REVIEW

3.1 Flow Dynamics in Rod Bundles

Hoffman (1964) studied the local heat transfer rate in a 7-rod bundle with electrically heated rods for different pitch-to-diameter ratios, *P*/*D*, being P the distance from one rod's center to another and *D* is the rod's diameter. The author added aluminum powder as a tracer and took pictures of the flow using stroboscopic lighting. Hoffman (1964) observed a wavelike movement that decreases with the growing gap width. This was the first observation through visualization of the large-scale structures in a rod-bundle.

Van Der Ros and Bogaardt (1970) carried out an experimental work to assess the mixing in two rectangular channels. Both channels have a cross-section of 10 *mm* x 10 *mm* and a gap with 4 *mm* depth (Fig. 1). The first and second channels have 1 *mm* and 2 *mm* gap width, respectively. The data were analysed by the eddy diffusivity approach. The Reynolds numbers considered ranged from 5000 up to 30000. It was observed that the mixing coefficient is inversely proportional to the gap width, confirming the results of many previous experimental works. They also observed that the wavelike movement showed a very regular pattern in amplitude and frequency inside the narrow gaps.

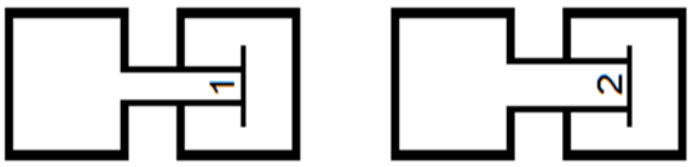

(a) (b)

Figure 1 Square channels with different gap width. (a) *d* = 1 *mm*. (b) *d* = 2 *mm*. Source: [Van Der Ros and Bogaardt 1970]

Rowe et al., (1974) performed an experimental work to investigate the effect of channel's geometry on a fully developed turbulent flow in a rod array parallel to the flow, Fig. 2. They considered two pitch-to-diameter ratios, namely 1.25 and 1.125. The working fluid was water and the Reynolds number ranged from 50000 up to 200000. The measurements were performed using a two-component laser-doppler

velocimeter. The variables assessed were the of axial velocity component, turbulence intensity and autocorrelation functions. The authors stated that the flow between the rod gap and the subchannel center seems to have periodic macroscopic flow pulsations whose scale, intensity and frequency increased as the rod spacing is reduced. The main conclusion is that the eddy diffusion in rod bundles is enhanced by macroscopic flow processes.

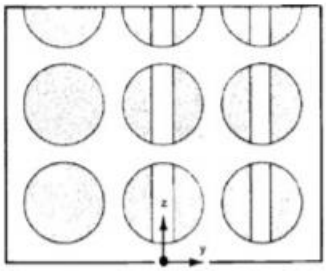

Figure 2 Rod bundle array cross-section studied by Rowe and co-workers. Source: [Rowe et al., 1974]

Hooper (1980) studied experimentally the single-phase turbulent flow through a square pitch array of rod bundles for P/D = 1.107 and 1.194 (Fig. 3). The Reynolds number used was 90 x 10^3. He measured mean velocity distribution, wall-shear stress variation and the six terms of the symmetrical Reynolds stress tensor. The velocity distributions were measured by Pitot probes and the shear stress by Preston tubes. The Reynolds stresses terms were gathered by hot-wire anemometry technique. In this work, Hooper verified that the azimuthal turbulent shear-stress markedly increases when P/D is reduced. He associated this observation to an energetic momentum interchange process in the rod gap. Also, the turbulent kinetic energy in the center of the rod gap becomes more intense as the pitch-to-diameter ratio P/D decreases.

Figure 3 Cross-section of Hooper's square pitch array of rod bundles. Source: [Hooper, 1980]

Hooper and Rehme (1984) carried out an experimental work in a 7000 mm rectangular cross section duct containing four rods with 157.5 *mm* diameter, as seen in Fig. 4. The authors studied this channel because the importance of this kind of geometry in nuclear power reactor, specially in order to reduce the azimuthal variation of the wall shear stress and the local heat transfer coefficient around the reactor's core. The hot-wire anemometry technique was used to measure the Reynolds stresses. They carried out measurements of mean axial velocity, wall shear stress variation, axial pressure distribution and Reynolds stresses. The axial and azimuthal turbulence intensities and the wall shear stress remarkably increased when the rod spacing was reduced. The azimuthal component of the Reynolds shear stress showed peaks in the rod-to-rod and rod-to-wall regions, the same locations where the azimuthal turbulence intensities showed the highest values. They concluded that there is a linear relation between the Reynolds number and the frequency of the large-scale structures found in the gap region. But they verified that the Strouhal number of these turbulent structures is independent of the Reynolds number. In closely spaced rod arrays, there are instabilities caused by parallel incompressible flows. This kind of instability generates an almost periodic azimuthal turbulent-velocity component in the gap, which is responsible for the mass, momentum and heat transfer in the gap area.

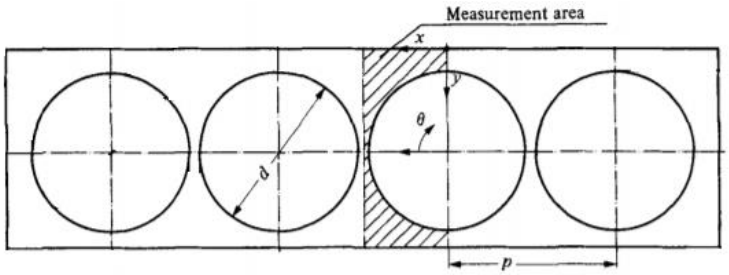

Figure 4 Experimental test section. Source: [Hooper and Rehme, 1984]

Möller (1991) proposed to determine experimentally the origin of the flow pulsations in the rod bundles and their features in function of the bundle geometry and the Reynolds number. The test section used was a 7000 *mm* rectangular channel containing four rods, according to Fig. 5. The geometrical proprieties of the test section were $1.045 \leq W/D \leq 1.183$ and $1.149 \leq P/D \leq 1.224$ for the symmetrical

arrangement. For the asymmetrical ones, the test section variables ranged $1.072 \leq W/D \leq 1.223$ and $P/D = 1.036$, being W the distance between rod to channel wall. The author used a Pitot tube to measure the flow velocity and cross-wire probes to measure the power spectra. All the measurements were gathered about 20 *mm* upstream the channel's outlet. The power spectra of the azimuthal component of the velocity fluctuation showed a fundamental frequency of 62.5 *Hz* in the center of the gap, while the axial component did not show any relevant frequency at this location. On the other hand, 20 *mm* away from the gap, the axial component of the velocity showed a pronounced peak with a fundamental frequency of 62.50 *Hz* while the azimuthal velocity component remained stressing the same characteristic frequency. The Strouhal number proposed by the author was based on the friction velocity, u^*, and the rod diameter, D, showed to be independent of the Reynolds number and function only of the gap width. Also, Möller proposed a flow model consisting of vortices street moving in the center of the gap rotating in opposite directions. The vortices are perpendicular to the rod surface and move in axial direction.

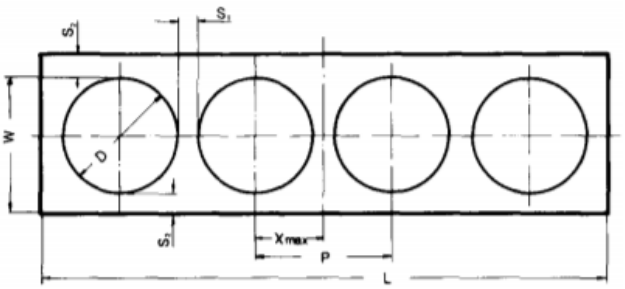

Figure 5 Test section used by Möller (1991) and (1992). Source: [Möller, 1991]

One year later, Möller (1992) investigated experimentally the interdependence between the flow pulsations, as the coherent structures were termed, and the mixing process across narrow gaps in rod bundles. The author used the hot-wire anemometry technique. The test section used can be seen in Fig. 5 and the geometrical parameters (W/D and P/D) are the same as the ones presented in the previous paragraph for Möller (1991). The results showed that the characteristic frequency of the flow pulsations is function of the bundle geometry and of the flow velocity. In narrow gaps, the large eddies generate velocity fluctuation signals with a

periodical behaviour and turbulence that enhances the mixing process. The author demonstrated that the mixing phenomena increases when the gap is reduced. This can be clearly seen in Fig. 6, where *Y* is the mixing factor and *S*/*D* is the dimensionless gap width.

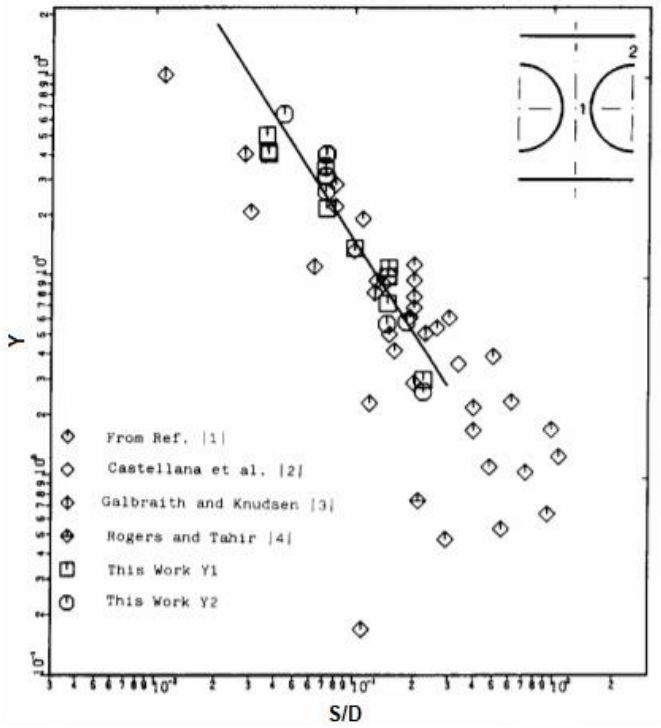

Figure 6 The mixing factor as a function of the dimensionless gap width. Source: [Möller, 1992]

Wu and Trupp (1993) assessed experimentally the turbulence phenomena in narrow gaps of a trapezoidal channel containing a rod inside, according to Fig. 7. The measurements were made using hot-wire anemometry. The hydraulic diameter of the test section is 31.44 *mm* and the Reynolds numbers were 52700, 54200 and 55200. The main parameters studied were turbulence intensity, turbulence kinetic energy, secondary flow and energy spectra.

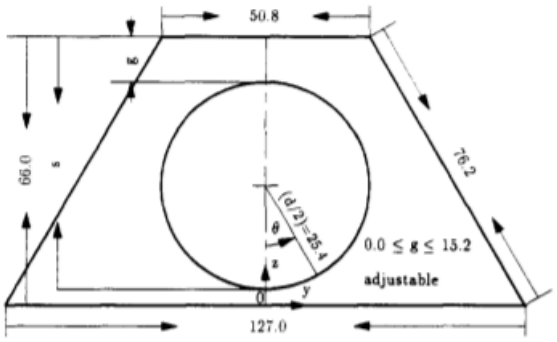

Figure 7 Test section dimensions in mm. Source: [Wu and Trupp, 1993]

The authors found an unusual region of high-magnitude turbulence intensity at the vicinity of the rod-to-wall gap. The values of this turbulence intensity increases when the wall-to-diameter ratio decreases. The azimuthal turbulence intensity distribution shows higher values than the axial component in the narrow gap. The turbulence kinetic energy increases when the gap is reduced, but substantially decreases when the gap is too small. Also, the turbulent kinetic energy is strongly influenced by the azimuthal turbulence intensity near the narrow gap. The secondary flow pattern in the corners of the channel in Fig. 7 coincided with the bulges found in the turbulent shear stress and turbulence kinetic energy distributions for the same channel. This suggests that the secondary flow is an important transport process in a given subchannel. In the spectral analysis, they found that the characteristic frequencies of the azimuthal component of the velocity measured in the center of the gap, had the same behaviour observed by Möller (1991). This indicates the presence of large-eddy motion in the azimuthal direction along the narrow gap exchanging energy with its axial component while it moves to the central area of the channel, keeping the same fundamental frequency.

Meyer and Rehme (1994) investigated experimentally the turbulent flow of air in a rectangular compound channel with variable gap and another rectangular channel with a small slot at one side, both channels with variable gap or slot width and length, shown in Fig. 8. The channel's length is 7000 *mm* and each square subchannels has a cross-section of 180 *mm* x 170 *mm*. The gap's width varied from 1.8 *mm* up to 10 *mm* and the depth between 10 *mm* and 77 *mm*. The Reynolds number, based on the bulk velocity U_b and the hydraulic diameter D_h, was 2.5 x 10^5.

A x-wire probe was employed to determine the turbulence intensities, Reynolds stresses, power spectral densities, autocorrelation and cross-correlation functions and spatial two-points cross-correlations.

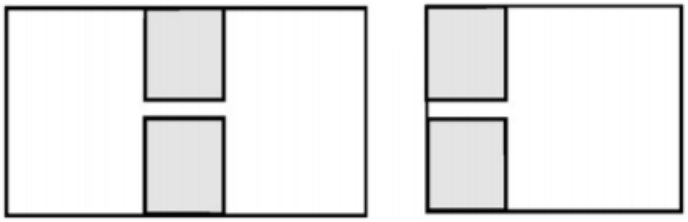

(a) (b)

Figure 8 Channels' cross section. (a) Rectangular channel with a gap. (b) Rectangular channel with a small slot at one side. Source: [Meyer and Rehme, 1994]

Meyer and Rehme (1994) found extremely high turbulence intensities and shear-stresses in and near the gap or slot. The power spectra density analysis presented high peaks at low frequencies for all velocities inside the gap and the slot, suggesting the presence of large-scale quasi-periodic structures, either inside or in the gap vicinity. Meyer and Rehme (1994) proposed a flow model for these structures that consists of two vortices on either side of the gap that are driven by the higher velocities outside the gap and that are rotating in opposite directions. These vortices are convected with a velocity U_c which was found to be approximately the average of the velocity at the center and the edge of the gap. The length of one period of large-scale oscillation is λ. The axial distance between consecutive vortices centers is $\lambda/2$, that was found to be independent of the velocity for a given geometry.

One year later, Meyer and Rehme (1995) assessed the large-scale quasi-periodic turbulent structures three in compound rectangular channels containing gaps and fins (Fig. 9). The first channel (Fig. 9a) has a lateral slot, the second (Fig. 9b) has a single fin and the third (Fig. 9c) has multiple fins. As working fluids, air was used for the first and second channels and a mixture of water and glycol for the third channel. The Reynolds numbers for the air were 4×10^4 and 2×10^5. For the water/glycol mixture, the Reynolds number ranged from 2300 to 100000. The authors carried out an experimental study employing flow visualization and hot-wire anemometry as measurement technique.

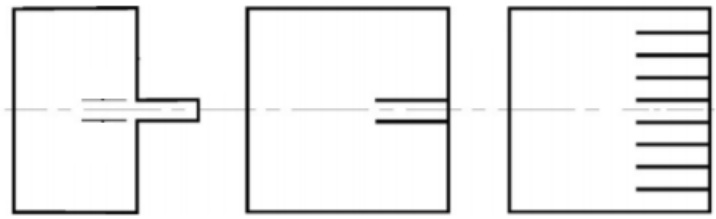

(a) (b) (c)

Figure 9 (a) First Channel: containing a lateral slot. (b) Second channel: containing a single fin. (c) Third channel: containing multiple fins. Source: [Meyer and Rehme, 1995]

Despite the different viscosities of the fluid used for each channel, the peak frequency in the power spectra did not show any significant variation. The peaks of the power spectra occurred inside the lateral gap of the first channel and inside the fins of the other channels. The visualization of the flow inside the slot of the first channel is shown in Fig. 10, where the large-scale vortices rotating in opposite directions moving axially through the gap can be seen. The same vortices have been observed inside the fins of the second and third channel. The authors concluded that there is a new type of instability for a fluid without any unsteadiness in the velocity distribution with a turning point, similar to a mixing layer between two parallel, although with different velocity streams. This instability can produce quasi-periodic vortices, which can occur in any longitudinal slot or groove parallel to a channel or in a connecting gap between two channels.

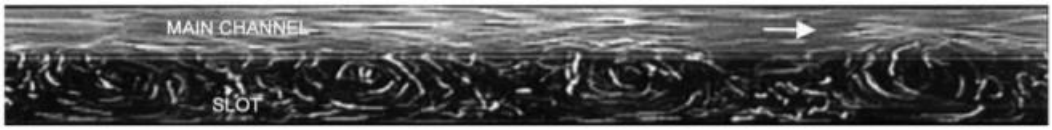

Figure 10 Visualization of vortices moving from left to right in the longitudinal of the first channel. Source: [Meyer and Rehme, 1995]

Biemüller et al. (1996) performed a numerical simulation using Large Eddy Simulation – LES in order to verify the flow model proposed by Meyer and Rehme (1994) in compound rectangular channels connected by a gap. Biemüller et al. (1996) used a rectangular channel divided in two other channels connected by a gap at one wall, which is shown in Fig. 11. The rectangular channel's cross-section is 180 *mm* x 331.6 *mm*; and the gap has a 10.2 *mm* width and 40.6 *mm* depth. The

measurements were performed at a position 30 *mm* upstream of the open outlet and at a Reynolds number of $Re = 2 \times 10^5$.

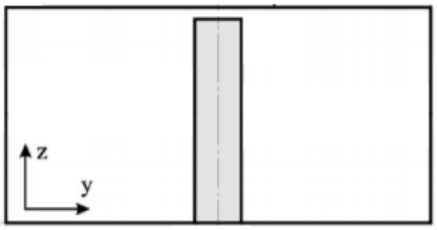

Figure 11 ***Channel's cross section.*** Source: [***Biemüller* et al.*, 1996***]

The LES simulation concluded by Biemüller et al. (1996) proved the existence of two vortices rotating in opposite directions at exactly the position predicted by the flow model proposed by Meyer and Rehme (1994). The vortices are transported in the streamwise direction with a convective velocity equal to 0.66 of the bulk velocity.

Guellouz and Tavoularis (2000a) studied experimentally the characteristics of the turbulent flow in a rectangular channel containing a rod, which can be seen in Figure 12. The authors employed the hot-wire anemometry measurement technique. The main geometrical properties were the hydraulic diameter, D_h=1.59D, and the W/D ratio 1.000 ≤ W/D ≤ 1.250. The Reynolds number ranged from 141000 to 149000 and was based on the bulk velocity, U_b, and on the hydraulic diameter. The reported measurements included the mean average axial velocity, skin friction and turbulent stresses. In order to characterize the presence of coherent structures, it was necessary to determine the frequency spectra and the convection speed of the coherent structures.

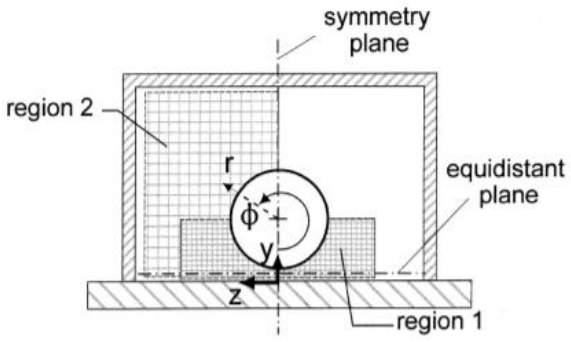

Figure 12 Test section and coordinate system. Source: [Guellouz and Tavoularis, 2000a]

Guellouz and Tavoularis (2000a) verified that the isocountours of the mean average axial velocity, *rms* (Root mean square) of the velocity fluctuations and the turbulent kinetic energy bulged towards the corner of the channel, suggesting the influence of secondary flows. The authors, however, stated that secondary flows cannot affect the turbulent stresses, but can only shift the location of their maxima. So, the presence of secondary flows cannot explain the high values of the maximum streamwise normal stress, close to the rod-wall gap. For higher values of W/D, the skin friction variations, along the bottom wall and around the rod, are not significantly high, but when the gap is reduced the skin friction strongly decreases near the channel's wall. Also, they found that the spanwise velocity fluctuation time-traces showed a highly periodical behaviour in the location z/D = 0.2, that is in the vicinity of the narrow gap. Near this location, z/D = 0.25, the spectra signal of the spanwise velocity showed a more pronounced peak for W/D = 1.050 than for W/D = 1.100. The average convective velocity, U_C/U_b, of the coherent structures increases as the W/D also increases.

For a better understanding of the coherent structures aspect, Guellouz and Tavoularis (2000a) presented a visualization of large-scale coherent structures crossing the narrow gap for W/D = 1.100 and Re_{Dh} equal to 16000, as observed in Fig. 13a. Many years later, Severino (2018) performed two visualization experiments for W/D = 1.100 and 1.200 (Fig. 13b and Fig. 13c, respectively) and a numerical visualization for W/D = 1.100 (Fig. 13d). The W/D = 1.100 case, both for Guellouz and Tavoularis (2000a) and Severino (2018), clearly shows the large-scale coherent structures across the narrow gap and a very small-scale turbulent diffusion. For W/D = 1.200 (Fig. 13c) it is not possible to observe the presence of turbulent structures, it can be seen just a developing flow. In the numerical visualization (Fig. 13d), the coherent structures can be easily seen too.

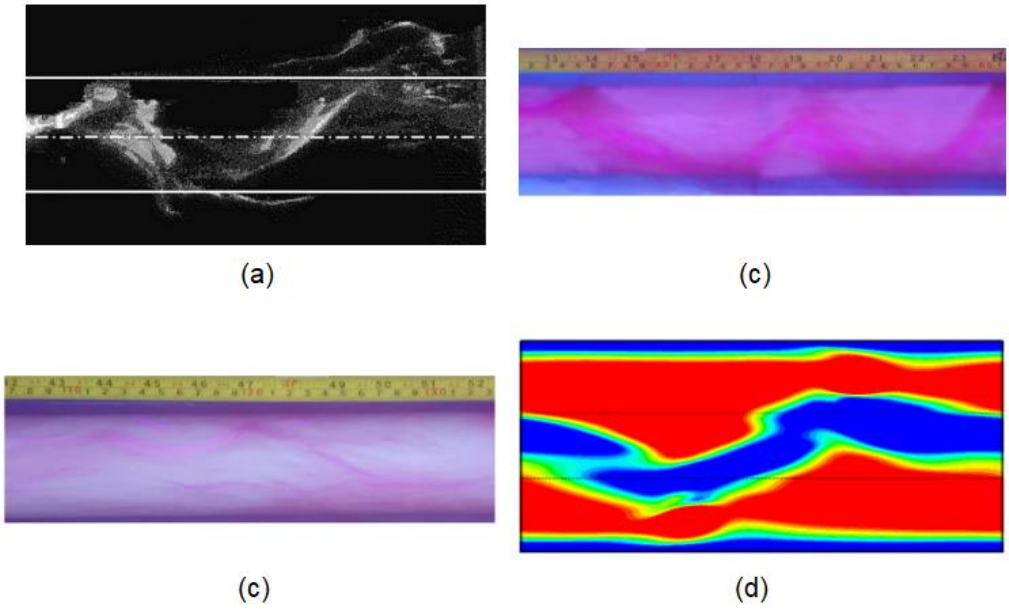

Figure 13 Coherent Structures visualization. (a) Visualization brought by Guellouz and Tavoularis (2000a) for W/D = 1.100 and Re_{Dh}= 16000. (b) Experimental visualization for W/D = 1.100 performed by Severino (2018). (c) Experimental visualization for W/D = 1.200 performed by Severino (2018). Numerical visualization for W/D = 1.100 performed by Severino (2018).

Guellouz and Tavoularis (2000b) focused on the physical conception of the coherent structures. The work was performed using the same geometry and Reynolds number assessed in Guellouz and Tavoularis (2000a). By using the conditional sampling technique, Guellouz and Tavoularis (2000b) were able to separate the large-scale structures from the smaller ones. The authors stated that, based on their physical model of the coherent structures, the relatively insensitivity of the intersubchannel mixing and heat transfer, due to the lower mean velocities in the narrow gap region and to the decreasing interfacial area between the subchannels, can be associated to the counteract and compensate effect produced by the large-scale motion.

Chang and Tavoularis (2005) studied the turbulent flow in a rectangular channel containing a single cylindrical rod, the same used by Guellouz and Tavoularis (2000a&b). They employed the Unsteady Reynolds Average Navier-Stokes – (URANS) method using a Reynolds stress model (RSM). The Reynolds number based on the bulk velocity, U_b, and on the hydraulic diamter, D_h, considered was 108000. The authors identified the presence of pairs of vortices with axes alternating on either side of the gap and transporting fluid through the gap. Also, it was

presented that about 60% the turbulent kinetic energy in the gap region is caused by the coherent structures.

Gosset and Tavoularis (2006) carried out an experimental work in a laminar flow aimed to assess the flow instability and the critical Reynolds number for the beginning of the instability appearance in a rectangular channel with a single rod inside, similar to the shown in Fig. 12, but the rod is placed in the upper region of the channel. The Reynolds number, based on the bulk velocity and on the hydraulic diameter, was considered in a range up to around 2000. The authors observed that, when the Reynolds number increases beyond a critical value, the laminar parallel flow in a rectangular channel containing a single rod inside start to present transversal instabilities across the narrow rod-wall gap. At a fixed Reynolds number, as the gap width decreases, the viscous forces are enhanced and can obstruct the local instabilities. On the other hand, for a fixed gap size, as the Reynolds number increases, the instabilities become stronger, arising quasi periodically vortical patterns on either side of the gap inducing fluid transport between the gap and the main channel.

Harbaoui and Guellouz (2006) performed an experimental campaign to investigate the onset condition for the formation of large-scale coherent structures in laminar flows through two parallel fins. The Reynolds number, based on the hydraulic diameter and bulk velocity, ranged from 433 up to 814. The authors found that the critical Reynolds number necessary for the appearance of coherent structures, when based on local parameters, showed to be constant for all assessed gap spacings. The authors also concluded that, regardless the critical Reynolds number, laminar flow through fins become unstable given rise to the formation of vortical structures. Also, the lateral extent of the structures seems to decrease if the gap size or the Reynolds number is fixed. For higher Reynolds numbers, the streamwise spacing of the structures increases linearly with the gap size and is independent of the Reynolds number. Finally, the convective velocity of the structures varies exponentially with the gap size and, when scaled by the local velocity, showed to be insensitive to the Reynolds number.

Two years later, Chang and Tavoularis (2007) used the same computational technique employed in 2005 to study the fully turbulent isothermal flow in a 60° sector of a 37-rod bundle (Fig. 14). The hydraulic diameter was $D_h = 0.29D$ and the bulk velocity $U_b = 13\ m/s$. The Reynolds number, based on the hydraulic diameter and the bulk velocity, was 40309. The authors identified, by the Q-criterion, coherent structures in the form of counter-rotating vortices forming in the regions of the rod-to-rod and the rod-to-wall gaps. The streamwise spacing between successive pairs of coherent structures was approximately equal to four rod diameters. The Strouhal number, based on the bulk velocity and the rod's diameter was found 0.27. The coherent structures were not spread randomly over the channel, but were connected to each other creating a network of vortices that surrounded all rods in the bundle. In order to avoid obsolete explanations and reach a consensus about the nomenclatures used by the research community, Tavoularis (2011) published a note to introduce a nomenclature for large-scale motions in rod bundles. Now, the coherent motions through a single gap are termed as "gap vortex street" and the coherent motions in a rod bundle together are termed as "rod bundle vortex network". The flow pulsations that leads to a gap vortex street is termed as "gap instabilities".

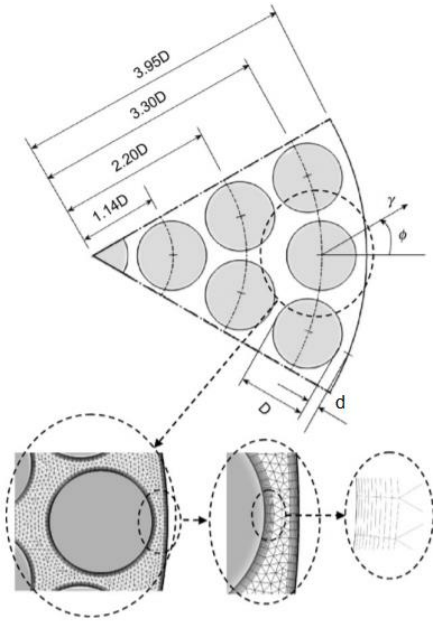

Figure 14 Cross section of the channel of the 60° sector of a 37-rod bundle and mash details. Source: [Chang and Tavoularis, 2007]

Merzari et al. (2008b) analysed the global linear stability in a laminar flow through an eccentric annuli and U-shaped channel. The discretization of the problem was made by using spectral collocation and it was employed Arnoldi-method and QZ algorithm to solve the eigenvalue problem. For the eccentric annular channel, it was identified a set of modes, consequence of the spanwise variation of the laminar velocity profile, that can be an additional cause of instabilities in this kind of channel and seems to increase for high eccentricities. In the case of the U-shaped channel, it was observed just a single mode, which is characterized by the propagation of an asymmetric wave in the streamwise direction.

Koched and Guellouz (2008) experimentally studied the formation of coherent structures in a compound channel with a floodplain. The work was conduced in a laminar flow with Reynolds number, based on the hydraulic diameter and bulk velocity, lower than 600. The geometric parameters used were l/h and δ/h. l is the width, δ is the gap width and h is the height of the flood plain. By a visualization experiment, it was possible to see the appearance of vortical structures associated to Kelvin Helmholtz instabilities. It was verified that the critical Reynolds number (when the structures start to appear) was influenced by the flow rate and the

geometry of the channel. They also found that the convection speed of the coherent structures increases with the Reynolds number, but less than the bulk velocity.

Piot and Tavoularis (2011) assessed the formation of instabilities in a laminar flow inside the narrow gap of an eccentric annular channel. The eccentricity studied was D_i/D_o = 0.282 and the Reynolds numbers, based on the bulk velocity and on the hydraulic diameter, considered were 470, 775 and 990. It was reported that the oscillation of the dye streak used in the experiment was stronger with eccentricity increasing, according to Fig. 15. Also, they reported that the critical Reynolds number for the narrow gap increased with the eccentricity. For the wider gap size, the critical Reynolds number was not influenced by small variation of the eccentricity.

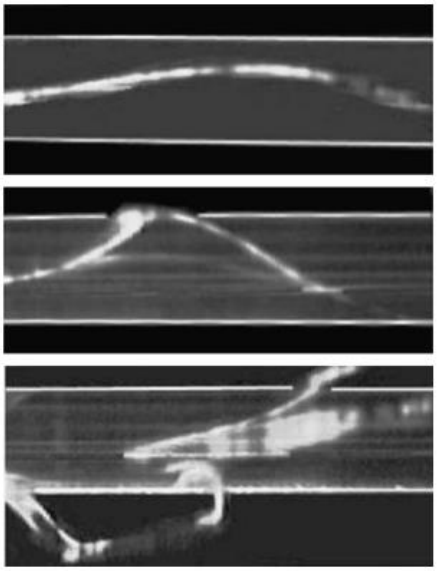

Figure 15 Oscillations of the dye streak injected in the middle of the narrow gap for a constant Re_{Dh} = 990 number and three different eccentricities. Source: [Piot and Tavoularis, 2011]

Goulart et al. (2014) studied experimentally the mean and fluctuant quantities of the turbulent flow in a rectangular compound channel containing two parallel plates attached on a side wall, forming a slot with width d and depth p (Fig. 16). The investigations were made considering a p/d ranging from 5.00 up to 12.5. The flow was considered incompressible turbulent air flow with Reynolds number, based on reference velocity U_{ref} and the hydraulic diameter D_h ranging from 7.30 x 10^3 up to 1.65 x 10^4. The authors also attempted to establish a relationship between the

results of this work and the mixing layer theory. Hot wire probes and a Pitot tube were employed as measurement techniques.

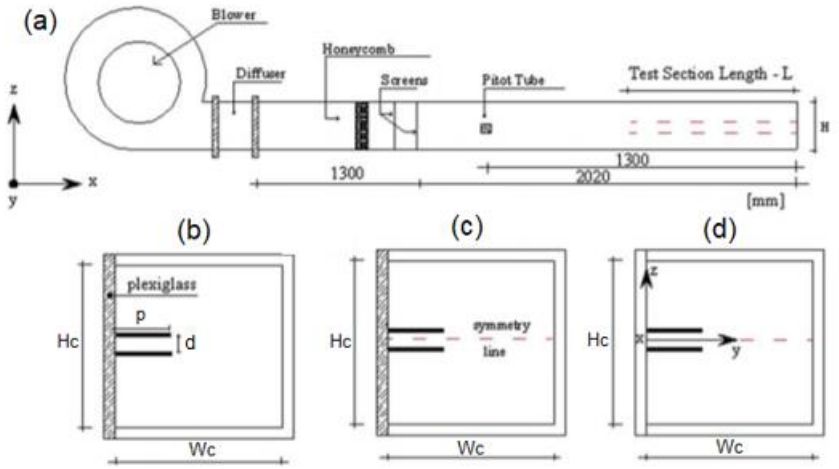

Figure 16 View of the test section. (a) Lateral view. (b) Cross-section geometrical parameters. (c) Cross-section symmetry line. (d) Coordinates system. Source: [Goulart et al., 2014]

Goulart et al. (2014)'s mean velocity measurements exhibited velocity profiles between the two plates that are very similar to the distributions in mixing layers. The mean and fluctuating quantities of the turbulent flow appear to be functions of the spanwise position. The Strouhal number, based on the average velocity of the edge of the plates, U_{ed}, and the mixing layer thickness $\delta_{(x)}$, was found to be equal to 0.17. The authors stated that the mixing layer thickness may be a linear function of the spanwise position. The power spectra showed pronounced peaks, indicating the periodical pattern of the velocity fluctuations. Also, Goulart et al. (2014) stressed the large-scale flow structures seems to no longer depend only on p/d ratio, but also $\delta_{(x)}/d$. They tested a new dimensionless geometric parameter, $\delta_{(x)}/d$. The main results showed that power spectra peaks were observed for $\delta_{(x)}/d > 2$.

Choueiri and Tavoularis (2014) carried out an experimental work to assess the velocity field in an annular channel as shown in Fig. 17. They performed a visualization of the flow by means of laser Doppler and stereoscopic particle image velocimetry techniques. The annular channel has a diameter ratio, D_i/D_o, of 0.5; an eccentricity, e, equal to 0.8 and a Reynolds number of 7300. The inner tube diameter is represented by D_i; D_o is the outer tube diameter; the eccentricity, e, is the distance

between the centers of the inner and outer tubes normalized by the outer tube radius; the Reynolds number is based on the bulk velocity, U_b, and on the hydraulic diameter, D_h. The general objective of their work was to check in detail the patterns of flow developing in eccentric annular channels under laminar, transitional and turbulent flow conditions and their dependence on the Reynolds number, the eccentricity, the inlet conditions and the inner-to-outer diameter ratio. In this sense, based on the observations of the mean velocity components for different azimuthal positions, the authors identified three different flow development regions: the entrance region, the fluctuation-growth region (FG) and the rapid-mixing (RM) region.

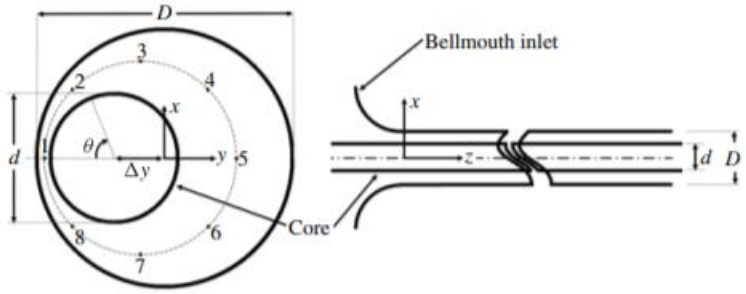

(a) (b)

Figure 17 (a) Cross section. (b) Lateral view. Source: [Choueiri and Tavoularis, 2014]

Figure 18 shows the time traces of the cross-flow velocity, U_x, and of the axial velocity, U_z, at the center of the gap at five downstream positions in the axial direction. In the cross-flow velocity case (Fig. 18a), close to the inlet, z/D_h = 1.4, the velocity signal appears to be random and unorganized. From z/D_h = 1.4, the velocity signal starts to show some kind of periodicity, but not very significant. This suggests that the periodicity begins somewhere in the entrance region. In the locations (FG) and (RM) the cross-flow signal shows a more pronounced periodicity than in the entrance region. In Fig. 18b, the axial velocity time-traces are seen to be qualitatively similar with corresponding positions for cross-flow velocity. However the first position has a less periodical signal in comparison with the last one. Furthermore, the axial velocity fluctuates at twice the frequency of the cross-flow component which is in agreement with the vortex street model proposed by Meyer and Rehme (1994).

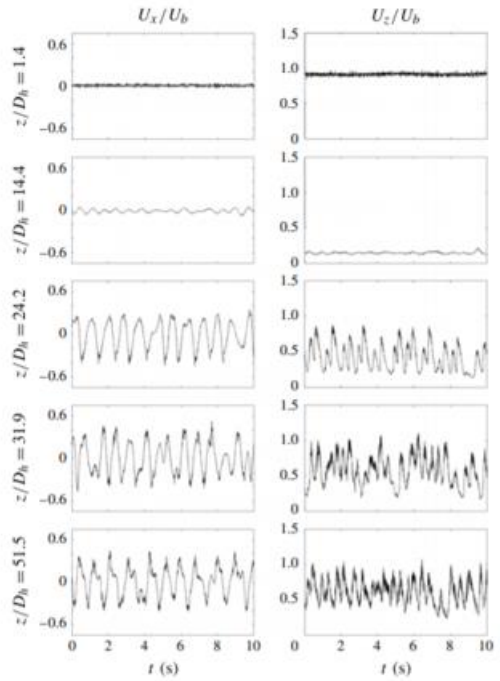

(a) (b)

Figure 18 Velocity time-traces. (a) Cross-flow component. (b) Axial component. Source: [Choueiri and Tavoularis, 2014]

In Fig. 19, it can be seen the vectors and the streamlines of the axial velocity in the gap. The vortices start to appear in the (FG) region and remain all along the channel.

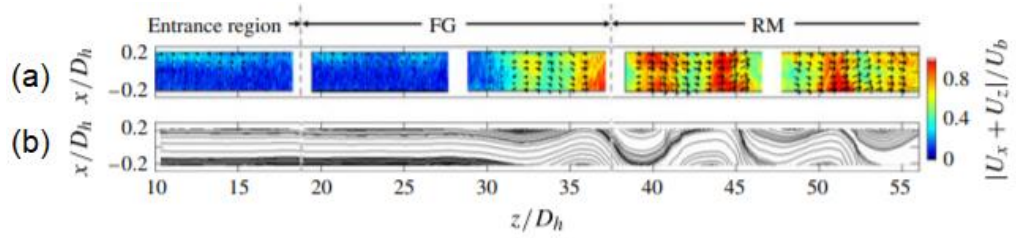

Figure 19 Axial velocity in the gap along the channel (*Re* ≈ 7800). (a) Vectors. (b) streamlines. Source: [Choueiri and Tavoularis, 2014]

Goulart et al., (2016) carried out a numerical simulation in order to predict the turbulent flow features in a rectangular channel containing a lateral slot, shown in Fig. 20. The work was aimed to provide quantitative data on the turbulence characteristic in the mentioned channel. A hybrid model Detached Eddy Simulation (DES) was used to model the incompressible turbulent flow, which uses LES/URANS approach to predict the turbulence. The Reynolds number, based on

the hydraulic diameter, the bulk velocity and in the kinematic viscosity in the channel is Re_{Dh} = 2.25x10^5. The dynamic results were compared with the experimental results of Meyer and Rehme (1994 and 1995).

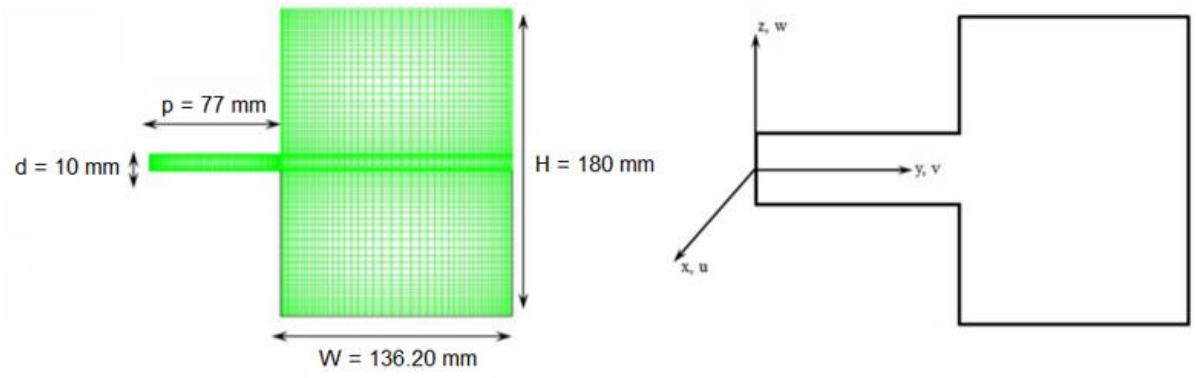

(a) (b)

Figure 20 Channel's cross section. Source: [Goulart et al., 2016]

In Fig. 21, the data of the streamwise velocity were gathered 30 *mm* upstream the outlet and was normalized by the bulk velocity, U_b. Due to the strong viscous effects inside the narrow slot, the lower maximum value of the streamwise velocity was found in that region and the highest occurs in the core of the main channel. The pronounced bulging in the streamwise velocity isolines towards the edges is likely to be caused by the secondary flows in the channel's edges. The velocity lines run almost parallel to the opposite wall of the channel, whereas near the slot a remarkable bending in the isolines towards the main channel can be seen. This is due to the strong component of the spanwise velocity emerging from the slot. The turbulent kinetic energy and the Reynolds stresses were made dimensionless using the square of the mean friction velocity, u^*, and the density of the fluid. The maximum values of the turbulent kinetic energy, k^+ and the normal Reynolds stresses occur in a location near the small slot. The turbulent kinetic energy was found 25% higher in comparison with the experimental results and the x-normal Reynolds stress, uu^+, is only 3% higher.

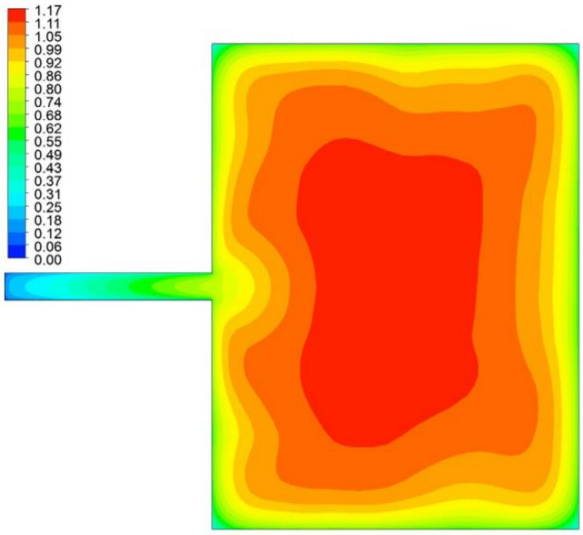

Figure 21 Isolines of the streamwise velocity componente at x/L = 0.95. Source: [Goulart et al., 2016]

Also, Goulart et al., (2016) observed that the velocity time-traces in the lateral slot showed a very periodical pattern, indicating the presence of large vortices in this region, as show in Fig. 22 through the *Q*-criterion visualization. The wavelength is the distance between two consecutive vortices with same vorticity sign and was assessed by determining how far the velocity signals are correlated. The wavelength, λ, found was in good agreement with the experimental results. The convection speed of the arrays of large counter-rotating votices, U_c, was determined by the product between the wavelength and the main frequencies of the large vortices, f. This value for the calculated convection speed was a slightly higher, by less than 10%, than the experimental results.

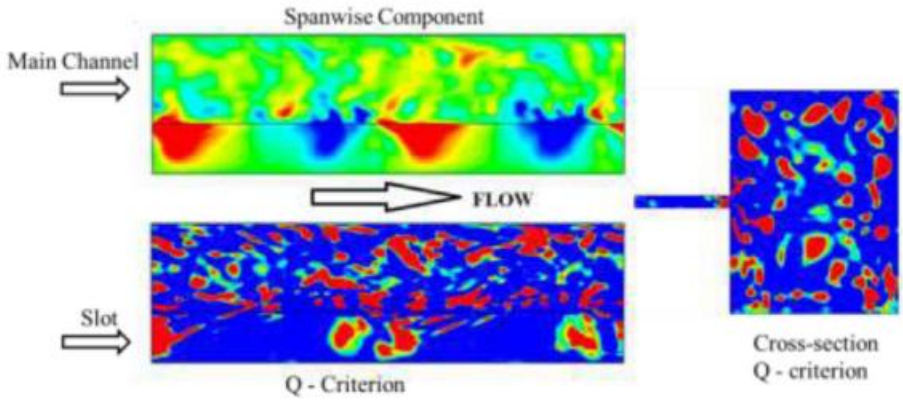

Figure 22 Visualization of large vórtices using *Q*-criterion. Source: [Goulart et al., 2016]

Melo et al., (2017) proposed to study experimentally the influence of the geometrical parameter of the channel over the dynamics of the turbulent flow. Single hot-wire probe was used to measure time-series velocities. The test section is a rectangular channel with two parallel plates attached on a side wall, according to Figure 23. Between the plates, there are gap with depth *P* and width *D*. It was studied twelve test sections with *P*/*D* ratio from 3.33 to 11.00. The Reynolds number considered was Re_{Dh} = 7.98x10^4. The authors aimed their work in order to identify the coherent structures which developed in channels containing a single slot. Furthermore, they also computed the spectral response of their velocity time-traces through Power Spectra Density (PSD) and wavelet analysis code. As a first approach PSD transform of the velocity signals was tried in order to identify vortices. Afterwards, the authors employed time-frequency tool (Wavelet Continuous Transform) in the vortices identification. Melo et al., (2017) was the first work to employ time-frequency analysis in this kind of problem with the purpose of showing intermittent and unsteady process of large vortices detection in compound channels.

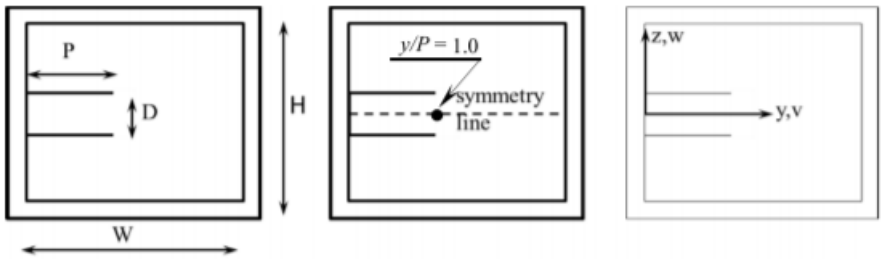

Figure 23 Channel's cross-section. Source: [Melo et al., 2017]

The authors concluded that both the *P*/*D* ratio and the length of the channel play an important role in the dynamics of the turbulent flow. The authors also found that periodic behaviour of the velocity time-series starts to appear only when $L > 56\sqrt{\boldsymbol{PD}}$, where *L* is the length of the domain. The Strouhal number values were different from those published by Meyer and Rehme (1995). However, when the L/D_h ratio increases, the Strouhal number moves closer to experimental values published in 1995. They found that the Strouhal number decreases when the gap width is increased, but increases when the channels's length increases too. By means the

Wavelet Continuous Transform, it was found that the broadness of the peak in the spectra is the effect of the unsteadiness of the main frequency whose value seems to wander in time.

Severino (2018) and Severino et al., (2018) studied the features of the turbulent flow and the formation of coherent structures in a rectangular channel containing a single rod (Figure 24). The authors used the numerical simulation and the experimental approaches. The rod diameter is D = 60 *mm* and the length is 33.33D. The narrow gap between the channel's wall and the rod is $d = 0.10D$. For the experimental part, hot-wire anemometry was employed to measure velocity fluctuations and frequencies. The experiments were carried out considering three different Reynolds numbers Re_{Dh} = 26500, 52100 and 86400, which are based on the hydraulic diameter, the bulk velocity and the kinematic viscosity of the air. In the numerical analysis, the k-ω-SST was employed to simulate the turbulent flow. In order to save computational resources translational periodicity between the channel's inlet and outlet was applied and the Reynolds number was reduced to Re_{Dh} = 8000. These numerical results were compared with the experiments of Guellouz and Tavoularis (2000a).

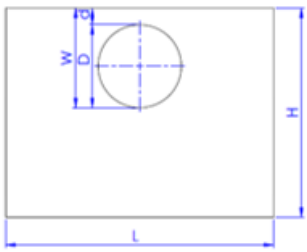

Figure 24 Cross-section of the channel studied by Severino et al., (2018).

The numerical simulation was able to predict the axial velocity distribution in relatively good agreement with the experimental results of Guellouz and Tavoularis (2000a). The maximum values were found in the widest region of the flow to reach U/U_b = 1.20, which was very close to the corresponding values published by Guellouz and Tavoularis (2000a) who found 1.17. The turbulent kinetic energy, $k^+ = k/U_b^2$, was also well predicted by the simulation. In fact, the values found near the lateral wall were respectively 0.012 and 0.010 by Severino et al., (2018) and

Guellouz and Tavoularis (2000a). The small difference between the numerical and experimental results might be attributed to the different Reynolds numbers.

The axial velocity time-traces were measured by hot-wire anemometry and computed through PSD analysis (Severino, (2018); Severino et al., (2018)). The velocity time-traces showed quasi-periodic behaviour, regardless of the Reynolds number used. The fundamental frequency of the velocity fluctuation signals increases with the bulk velocity. The highest peaks of the spectra were found for the lowest Reynolds numbers. The Strouhal number found for W/D = 1.10 was 0.15, which is a little lower in comparison to the measured value by Guellouz and Tavoularis (2000a). The author also found the length of the rod is important to the development of instabilities, significantly affecting the Strouhal number.

Moradi and Tavoularis (2019) performed a linear stability analysis of laminar flow in weakly eccentric annular channels. The main geometric parameters of the analysis were the eccentricity, ε, and the diameter ratio, $\gamma = D_i/D_o$. The Reynolds number, based on the bulk velocity and on the hydraulic diameter, was over 3000. The authors reported that the formation of instabilities at mid-gap is due to an inviscid mechanism, which is a consequence of the appearance of two inflectional points in the azimuthal base velocity profile. The critical Reynolds number minimum value was 529, reached at γ = 1.3 and ε = 0.01 (the most unstable values for ε and γ). Finally, the most unstable regions observed were at mid-gap and the aspect of the instabilities were in form of travelling waves.

Souissi et al., (2020) performed a linear stability analysis of a laminar flow in a rectangular channel with a rod inside and a channel formed by two rectangular ducts connected by a narrow slot, as shown in Fig. 25. The authors aimed to study the appearance of coherent structures, and the parameter for their onset, in the narrow regions of the mentioned channels. During the work, the eigenvalue problem was solved using the Tau-Chebyshev collocation method.

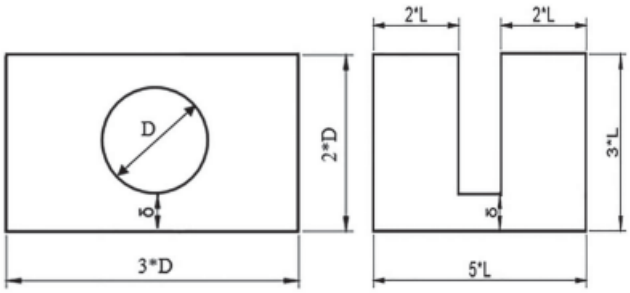

(a) (b)

Figure 25 Channels studied. (a) Rectangular channel with a single rod inside. (b) Channel formed by two rectangular ducts connected by a narrow gap. Source: [Souissi et al., 2020]

The variation of the critical Reynolds number found by Souissi et al., (2020) was in qualitatively good agreement with the results in Gosset and Tavoularis (2006) for a rectangular channel containing a cylindrical rod, according to Fig. 26. The differences in terms of values can be assigned to the fact that Souissi et al., (2020) used only the spanwise variation to predict the instabilities. Those values for the critical Reynolds number are the onset of instabilities in the narrow gap, not necessary the onset of instabilities for the entire channel. It was verified that large-scale vortical structures were formed in the narrow regions due to the presence of particular velocity profile. Also, the authors observed the appearance of two counter-rotating vortices in the narrow flow regions as a consequence of flow instabilities.

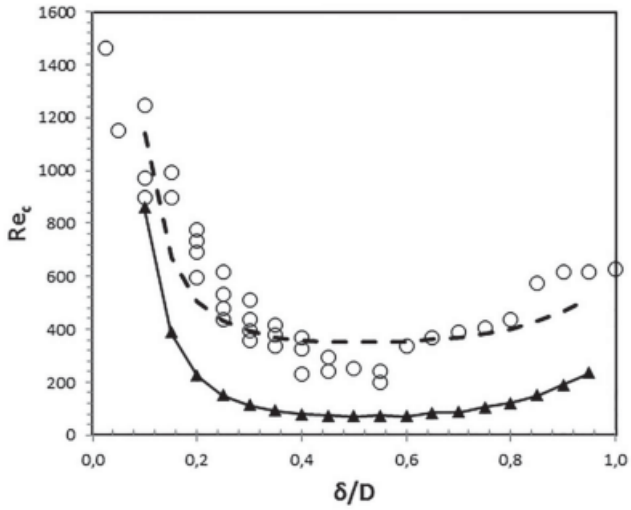

Figure 26 Variation of the critical Reynolds number (Re_C) for the rectangular channel containing a cylindrical rod. Numerical results by Souissi et al., (2019) (▲). Experimental results of Gosset and Tavoularis (2006) (○).

Candela et al., (2020) carried out a numerical simulation of the turbulent flow in an eccentric annular channel (Fig. 27). The Reynolds number, based on the hydraulic diameter, the bulk velocity and the kinematic viscosity of the air was Re_{Dh} = 7300. The eccentricity, e, and the radius ratio, D_i/D_o are 0.8 and 0.5, respectively. The channel's length is 1500 *mm*. They used the hybrid DES-SST model to model the turbulent flow. The results were compared with the experimental results of Choueiri and Tavoularis (2014).

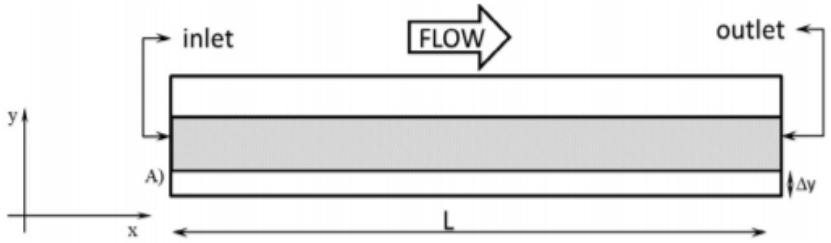

Figure 27 Annular test section. Source: [Candela et al., 2020]

The numerical results successfully predicted the three main regions considered by Choueiri and Tavoularis (2014). The velocity flow field was seen to oscillates and the mean average velocity starts to increase in the narrow gap from x/D_h > 30. The velocity time-traces showed that the fluctuation starts to decrease as it moves azimuthally. The Strouhal number and the speed of the vortices were in good agreement with the results presented by Choueiri and Tavoularis (2014). The fundamental frequency of the velocity time-traces in the gap is twice as high as the frequency found in the widest regions. This is because the wavelength in the narrow gap is half of that in the widest locations. By using the Q-criterion, Candela et al., (2020) found that the coherent structures spread from the narrow gap to the lateral subchannel.

3.2 Heat Transfer in Rod Bundles

Palmer and Swanson (1961) performed an experimental work to assess the average and local heat transfer coefficients in a seven-rod cluster arranged in a triangular array. The pitch-to-diameter ratio considered was 1.015. The working fluid was air and the Reynolds number ranged from 10000 to 60000. The rod heat flux

ranged from 385 *W*/*m²* up to 962 *W*/*m²* and the rod's surface temperature interval was 38°*C* to 71°*C*. The measured average heat transfer coefficients were similar to those for smooth round ducts. The variation of the azimuthal local heat transfer coefficients at *Re* = 20000 was 0.5 up to 1.3 of the average values. Palmer and Swanson (1961) did not consider any influence of the flow dynamics on the heat transfer.

Groeneveld (1973) carried out an extensive study about the convective heat transfer process. Taking into account the literature available at that time, he determined $I = \frac{\bar{h}_{bundle}}{\bar{h}_{tube}}$ and $J = \frac{\bar{h}_{min}}{\bar{h}_{bundle}}$ based on a compilation of the literature values. *I* is the ratio between the average convective heat transfer coefficient around a certain tube and the convective heat transfer in a circular tube, based on the same Reynolds and Prandlt number. Whereas *J* represents the ratio between the minimum convective heat transfer and the average coefficient around a rod. The *I* and *J* values ranged from 0.75 up to 1.0 and 0.80 up to 1.0, respectively. Both ratios increased as the gap-rod diameter becomes higher. The results obtained by Groeneveld (1973) showed to be in good agreement with those found by Palmer and Swanson (1961). Almost ten years later, Berger and Ziai (1982) obtained experimental results very similar to those found by Groeneveld (1973).

Seale (1979) performed a numerical and experimental work to assess the turbulent diffusion and secondary flow in a four-rod cluster. The pitch-to-diameter ratios studied were 1.100, 1.375 and 1.833. The Reynolds number, based on the rod's diameter *D* and on the mass flow rate, obtained from numerical integration of the measured velocity, ranged from 34369 up to 299603. In the numerical analysis, the *k*-ε turbulence model was employed. The author concluded that the temperature distribution in the channel's center is not related to secondary flows, but seems to be associated with the high mixing rates due to the significant anisotropy of the turbulent stresses in narrow gaps.

Guellouz and Tavoularis (1992) assessed experimentally the heat transfer characteristics and the flow temperature distributions around an outer central rod of a CANDU type 37-rod bundle model with the pitch-to-diameter ratio *P*/*D* = 1.149 (Fig. 28). This rod was heated locally by heated block that is powered by an electric

cartridge heater providing a nominal power of 1100 *W*. The corresponding Reynolds number, based on the hydraulic diameter of the 37-rod bundle, was 48000. The measurements of the local heat transfer coefficient were obtained for different angular positions around the central rod and for different rod-wall gaps, *W*/*D*.

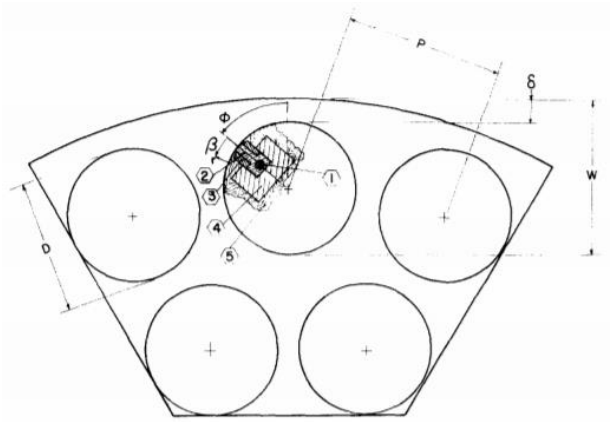

Figure 28 Cross-section of the rod-bundle. (1) electric cartridge. (2) block. (3) Fiberglass insulation. (4) Cement shroud. (5) wooden rod body. Source: [Guellouz and Tavoularis, 1992]

Guellouz and Tavoularis (1992) found that when the heated part of the rod is aligned with the narrow gap, the isocontours of the mean temperature and of the temperature fluctuations were essentially symmetric, but were strongly asymmetric bulging towards the rod-to-wall gap when the heated part was facing a wider region. They explained these observations by the inhomogeneity of the mean velocity and the turbulent kinetic energy in the adjacent subchannels, which cause heat diffusion in a non-uniform manner. We know now that this statistical inhomogeneity is due to the presence of the large-scale coherent structures. Figure 29, reproduced from Guellouz and Tavoularis (1992), show the variation of the local heat transfer coefficient, *h*, in the central rod of the rod bundle for different positions *W*/*D* as a function of the azimuthal position. The coefficient was normalized by the average value of the local coefficient $\hat{h}_{des}$ = 76 *W*/*m*²*K*. The minimum value of the heat transfer coefficient occurs near the gap regions and the maximum value is found in the widest regions of the channel. The central rod shows two regions of low values of *h*: rod-to-wall and rod-to-rod. Also, the heat transfer coefficient presents stronger variations for very narrow gaps, for example *W*/*D* < 1.04.

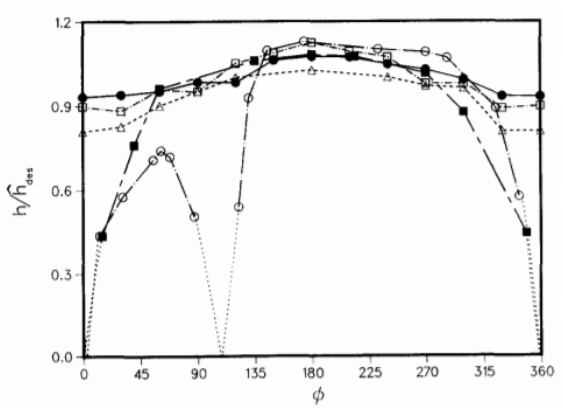

Figure 29 Variation of the local heat transfer coefficient as a function of the azimuthal postion in the central rod for different positions W/D: (●) 1.149. (□) 1.089. (Δ) 1.030. (■) 1.000. (○) rod-rod-wall contact. Source: [Guellouz and Tavoularis, 1992]

Krauss and Meyer (1996) performed an experimental campaign in a 37-rod bundle hexahedral arrangement with the aim of documenting the structure of the turbulence in different subchannels and to estimate the convective heat transfer, as well. They assessed the heat flux between an isothermal wall and a heated rod and compared it to the heated central rod of the same rod bundle. The channel's section is hexagonal with a total length of 11500 *mm* and rod diameters of 140 *mm*. The geometric parameters considered for the study were *P*/*D* = 1.12 and *W*/*D* = 1.06. The hydraulic diameter D_h, the bulk velocity U_b and the bulk temperature T_b were 48.8 *mm*, 19.4 *m*/*s* and 302.25 *K* respectively. The Reynolds number was 65000. Figure 30 shows the cross-section of the channel and some important geometrical parameters. The rods were made by epoxy reinforced with fiberglass, sheathed with 50 *μm* foil of monel metal, that serves as a resistance heating element. The rods were heated by low-voltage, high direct currents to temperatures in the range of 60-100°*C*.

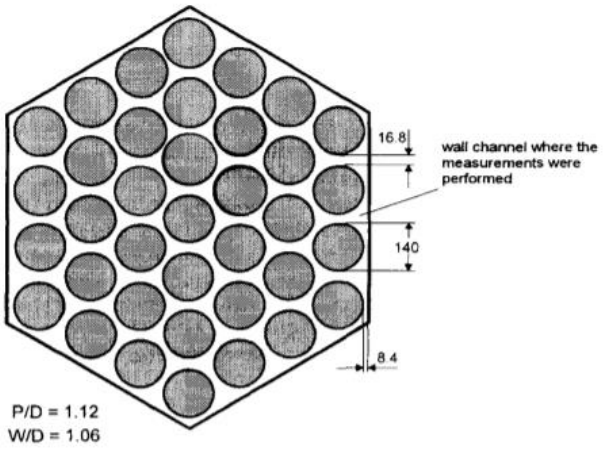

Figure 30 Cross-section studied by Krauss and Meyer (1996).

Figure 31a shows the temperature distribution between the isothermal wall and a heated rod as measured by Krauss and Meyer (1996). The temperature distribution between the isothermal wall and heated rod varies over a wider range in comparison with the case of the central heated rod. The maximum value of the temperature was found in the rod-to-rod gap region. Figure 31 b presents the turbulent heat flux distribution as a function of the azimuthal position. Its maximum value occurs in the narrow region rod-to-rod gap, where the intensity of the temperature fluctuation is also maximum. The variation of the turbulent heat flux in the azimuthal direction between the isothermal wall and the heated rod is larger in comparison with the central heated rod case. The authors also verified that the power spectra of the velocity and temperature fluctuations showed peaks that are characteristic of the quasi-periodic flow structures present in the regions of the narrow gaps.

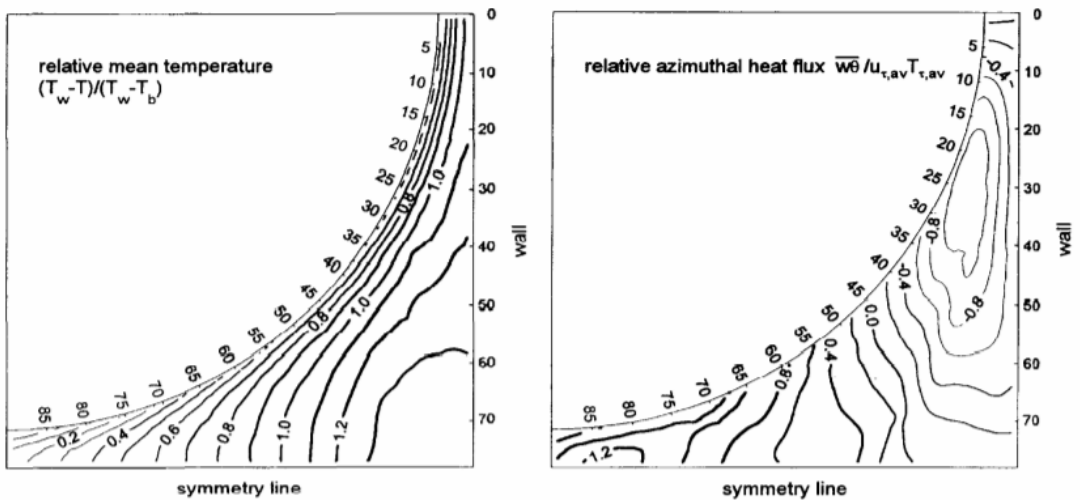

Figure 31 (a) Distribution of time-mean temperature. (b) Turbulent heat flux in the azimuthal direction. Source: [Krauss and Meyer (1996]

Guellouz (1998) studied experimentally the turbulent flow in a rectangular channel containing a single rod, the same channel shown in Fig. 12. Also, the author explained the implications of the flow dynamics on the mixing process and heat transfer in the mentioned channel. Further, the author was able to fit practical empirical correlations for the subchannel average and the gap local heat transfer coefficients to experimental results available in previous literature. A scattering that occurred among the fitted correlation and the experimental data was attributed, according to the author, to experimental uncertainties, different geometries and the conditions of the experiments. The channel has an aspect ratio of 2/3 and the rod's diameter is equal to half of the channel's cross-section height. The rod was positioned in order to form narrow gap with the lower wall. The Reynolds number, based on the hydraulic diameter and in the bulk velocity, was Re_{Dh} = 140000. The author employed hot-wire anemometry as velocity measurement technique.

The author verified that the coherent structures have strong influence on both the local heat transfer in the gap and the intersubchannel mixing. The large-scale structures transport momentum and heat, exchanging the warm fluid and the cooler one through the gap. The cooler fluid from the widest region is then transported to the narrow gap vicinity enhancing heat extraction. Guellouz (1998) also found that the coherent structures tend to reduce the velocity and temperature variations in the subchannels. This also was seen by Candela (2019). This indicates that the

presence of coherent structures increases the heat transfer in the gap and the intersubchannel mixing. To better characterize the effects of the coherent structures on the local heat transfer in the gap and the intersubchannel mixing, Guellouz (1998) pointed to the necessity to document the strength, the spacing, the convection speed and the lateral extent of the vortices in the narrow region. According to the fitted correlation for the experimental data, as expressed in eq. (1), the heat transfer seems to be relatively insensitive for values of *P*/*D* ratio higher than 1.1.

$$J = 0.741[1-e^{-97.90(P/D-1)}]+0.254[1-e^{-7.05(P/D-1)}] \quad (1.0 \le P/D \le 1.65) \qquad (1)$$

Holloway et al., (2005) studied experimentally the influence of the support grids of the rod-bundles on the azimuthal local heat transfer variation over the rod's surface. The supporting grid was used to keep the rods fixed in an array. The authors assessed three kinds of supporting grids, shown in Fig.32a, b and c. The standard grid, shown in Fig. 32a, is the simplest model and is formed just by supports to hold the rods. The disc grid, Fig. 32b, has blunt disc blockages attached to the downstream edge of the support grid. Finally, the split-vane grid is shown in Fig. 32c, which has split-vane pairs attached to the downstream edge of the support grid. Fig. 32d shows a schematic view of the rod-bundle used in the experiments. The hydraulic diameter D_h and the bulk temperature T_b were 11.78 *mm* and 20°*C*, respectively. The Reynolds numbers, based on the hydraulic diameter of the central subchannel were 28000 and 42000, with water as the working fluid. The location of the heat transfer measurements was around the circumference of the central rod in the axial postions 2.2, 6.5 and 36.7D_h downstream of the third grid support. They used the Particle Image Velocity (PIV) to gather the velocity and a hot film sensor to measure the azimuthal variation of the heat transfer.

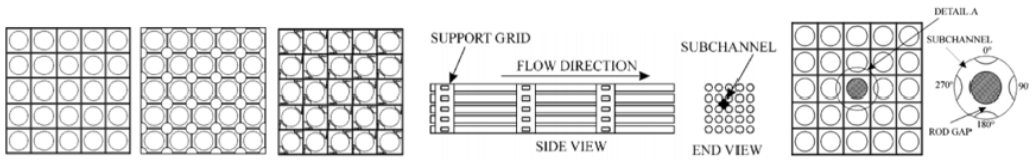

Figure 32 (a) Standard grid. (b) disc grid. (c) split-vane pair grid. (d) Schematic view of the rod-bundle. (e) Instrumental location. Source: [Holloway et al., 2005]

Figure 33a, b and c shows the azimuthal distribution of the Nusselt number for the three kinds of supporting grids for three downstream axial locations under the Reynolds number Re_{Dh} = 28000. The Nusselt number, based on the convective heat transfer coefficient h_θ, the hydraulic diameter D_h and the thermal conductivity of the working fluid k, was normalized according to eq. (2), being stressed as a function of the azimuthal position. $Nu_\theta(Z)$ is the azimuthal Nusselt number and $\overline{Nu_\theta(Z)}$ is the average azimuthal Nusselt number.

$$Nu = \frac{Nu_\theta(z) - \overline{Nu_\theta(z)}}{\overline{Nu_\theta(z)}} \tag{2}$$

In the standard grid case (Fig. 33 a), the peak-to-peak variation of the Nusselt number occurs at 2.2D_h downstream of the grid. The maximum value was found at an angle of 45°, adjacent to the subchannel flow area, whereas the minimum value occurs at 180° position, near the (narrow) gap region. As the flow develops, along its main axis, the peak-to-peak variation of the Nusselt number decreases. At 36.7D_h, where the flow is fully developed, the Nusselt variation is much smaller in comparison with the other upstream positions.

In Fig. 33b, the disc-type is tested, under the same boundary conditions. The variation of the Nusselt number for all the locations is similar to those observed for the standard case at 36.7D_h.

In the last case (Fig. 33c) i.e. for the split-vane pair grid, the peak-to-peak Nusselt variations were found at the axial locations 2.2D_h and 6.5D_h. For this type of grid, the maximum Nusselt number was found in the rod-to-rod gap at 90° and 270° angles and the minimum values was observed at many azimuthal positions. The flow in the split-vane pair grid is more complex due to flow separation from the rod, generating large variations of the Nusselt number. Also, Holloway et al., (2005) identified two vortices shed in the split-vane grid at the location 2.2D_h and a single vortex was documented at 25.5D_h

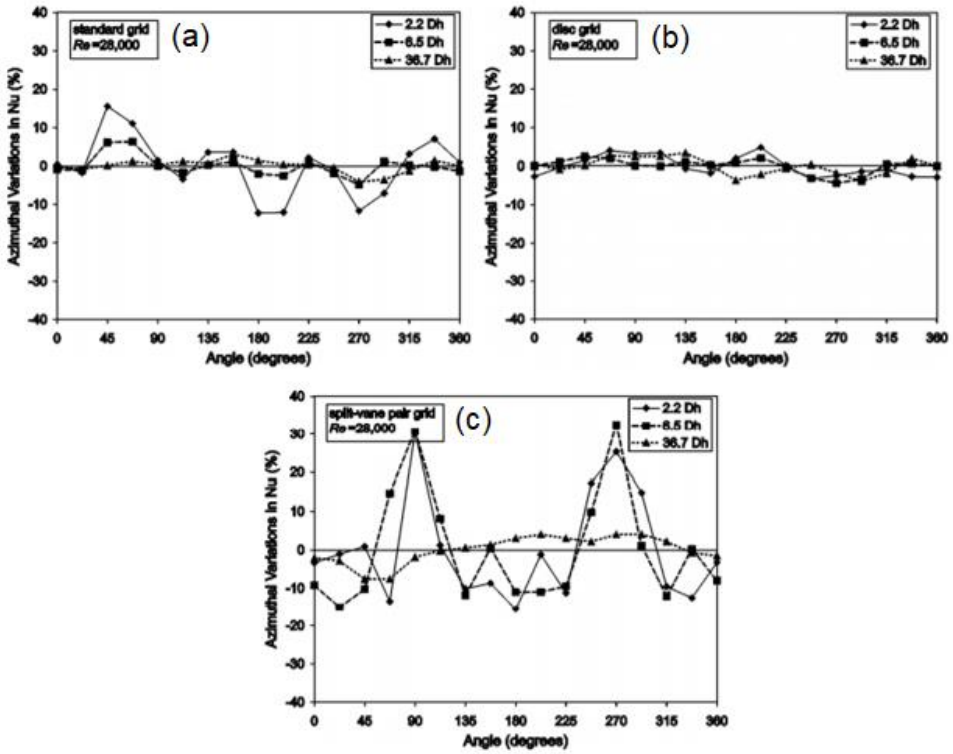

Figure 33 Variation of the azimuthal Nusselt number. (a) Standard grid. (b) Disc grid. (c) split-vane pair grid. Source: [Holloway et al., 2005]

Chang and Tavoularis (2006) conducted a numerical study in order to assess the influence of the coherent structures on the temperature field and heat transfer in a rectangular channel with a single rod in the core (Fig. 12) i.e. the same configuration as Guellouz and Tavoularis (2000a&b). The Reynolds number, based on the bulk velocity U_b ando n the hydraulic diameter D_h = 1.59D, was 108000. They considered W/D = 1.10 as the main geometric parameter. The unsteady velocity fields were computed by solving Unsteady Reynolds Average Navier-Stokes equations system – URANS. As turbulent models the authors used the Reynolds Stress Model (RSM). The authors concluded that the large-scale structures transport fluid across the narrow gap, moderating the time-average temperature rises in the gap, however producing significant local variations of the instantaneous temperature and heat transfer coefficient.

Two years later, Chang and Tavoularis (2008) investigated numerically the turbulent flow temperature fields in the same test section (Fig. 12). The authors focused on the implication of diminishing the gap size on the flow dynamics and heat

transfer in the narrow gap. The Reynolds number was based on the same scales from the earlier work, being set at 108000. The gap width was dimensionless using the rod's diameter, d/D, ranging from 0.01 up to 0.10. The Unsteady Reynolds-Averaged Navier-Stokes equations was used to discretize the time-dependent flow field, whereas the Reynolds Stress Model was employed to solve the additional momentum flux caused by the turbulence. Independently of the d/D investigated, the authors found Nusselt numbers (normalized by its average value around the rod) ranging from 0.6 in the gap and 1.2, reaching the highest values at about 60°, near the wider channel's region. Similar results were found later by Duan and He (2017). The Nusselt number variations were relatively large for the d/D = 0.10 and, 0.03 and vanished for d/D = 0.01. The authors found that the coherent temperature fluctuations substantially increased when the gap was decreased from d/D = 0.10 from d/D = 0.03, but when the gap was decreased to d/D = 0.01, the fluctuations disappeared. Thus, as $d/D \rightarrow 0$, the frequency of the temperature fluctuations decreases until the coherent structures completely disappear. This phenomenon was associated by the authors to the strong viscous effects in the gap.

Candela (2019) performed a numerical simulation in order to investigate the effects of the velocity fluctuations on the heat transfer in an eccentric annular channel, which can be seen in Fig. 34. The channel length, L, and the diameter ratio, D_i/D_o, were 1500 *mm* and 0.5, respectively. The eccentricity of the channel ranged from 0.7 up to 0.9, in intervals of 0.05. The Reynolds number, based on the hydraulic diameter, the bulk velocity and the kinematic viscosity was kept constant and equal to Re_{Dh} = 15000 and the Prandtl number was Pr = 0.7. The heat flux was prescribed at q'' = 2000 W/m^2 for the inner surface and the outer wall was considered insulated. The hybrid DES-SST model was used to compute the additional momentum flux caused by turbulence

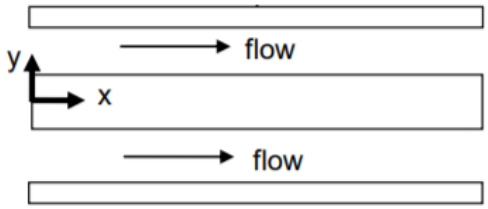

Figure 34 Schematic view of the annular channel's geometry. Source: [Candela, 2019]

The authpor, in her Master degree work, (Candela, 2019), showed that the surface of the inner rod is affected by the velocity fluctuations. The average temperature on the rod's surface starts to present oscillations just few hydraulic diameters downstream of the inlet as the gap becomes tighter and the eccentricity becomes higher. The average temperature suddenly decreases and gets closer to the concentric case at the same station where gap instabilities appear for the very first time. For the Nusselt number, it was seen when the streamwise velocity fluctuation intensities were strongly reduced at the narrow gap, the Nusselt number started to behave like in a concentric channel. This is due to the high velocity fluctuations intensities in the spanwise direction at the narrow gap vicinity. Then, the author concluded that the spanwise velocity fluctuation seems to play an important role in the heat transfer process, exchanging cold fluid, from the open areas, and warm fluid from the tighter spacer, through the narrow gap.

3.3 Concluding Remarks

This section will remind the main topics brought by the previous literature revised above. The bibliographic review was divided in two parts: the first discussed the flow dynamics for compound channels; in the second, it was presented works to understand how the heat transfer in those channels can be affected by flow dynamics and geometric parameters. The two parts of the bibliographic review will be presented in the following paragraphs.

At first, it was discussed the early observations of wavelike structures in compound channels almost sixty years ago up to studies of instabilities formation made nowadays. The most important topics mentioned in the first part of the bibliographic review, considering the scope of this work, is the dynamics of turbulent flows, formation of instabilities, the implications of the presence of coherent structures, some geometrical parameters studied in compound channels, spectral analysis, and experimental techniques of measurement.

The heat transfer in compound channels have been studied since a long time, but in the beginning, the effects of coherent structures were not considered. By the fact that coherent structures have a striking influence over the flow dynamics in narrow regions of compound channel, the researchers should consider this phenomenon in their work about heat transfer. In the second part of the bibliographic review, it was brought some important previous results about heat transfer, specially for the present work, such as variations of temperature and Nusselt number distributions in terms of some geometric parameter of the channel.

In conclusion, it was reviewed many works presenting studies for a variety of compound channels' geometries. Although the heat transfer in those channels have been extensively studied in the last decades, the topic still can be more deeply explored. In this sense, the present work will discuss about some differences between a channel containing a closed and hollow rod in terms of spectral analysis and determine the Reynolds-Colburn analogy using local bulk velocities.

4 EXPERIMENTAL PROCEDURE

4.1 Test Section

The experiment was carried out in a compound channel containing a single circular tube. This test section is the same geometry used by Guellouz and Tavoularis (2000a), Chang and Tavoularis (2006) and Severino (2018). Figure 35 shows a schematic view of the channel with the test section. The fan is responsible for producing air flow and is controlled by a frequency inverter, which was set at 50 *Hz* throughout the experimental campaign. Downstream of the fan there are a set of screens and a honeycomb to decrease the turbulence intensity level in the test section.

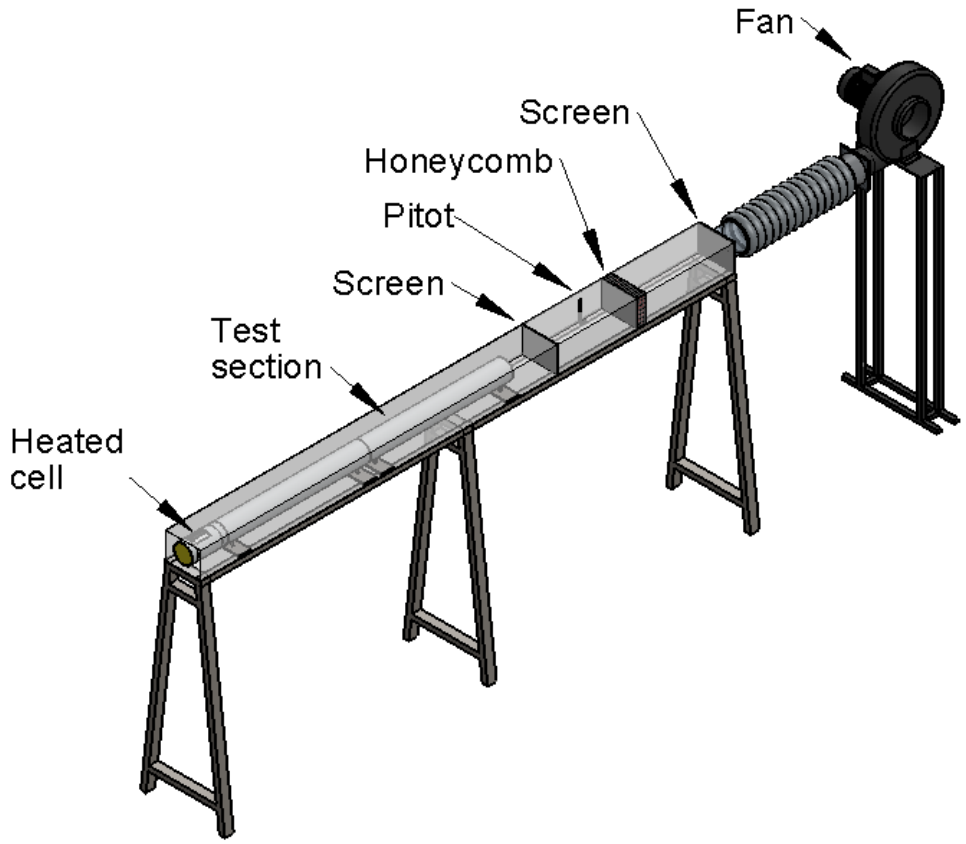

Figure 35 Schematic view of the channel with the test section.

Figure 36 shows a lateral view, a transversal section and half-channel's transversal area. The total length of the channel is 3000 *mm*, the test section length is 1800 *mm*. For the transversal section, W_C = 200 *mm*, H = 150 *mm* and D = 101 *mm*. Four gap spacings, namely W/D = 1.050, 1.100, 1,150 and 1.200 were used in these experiments.

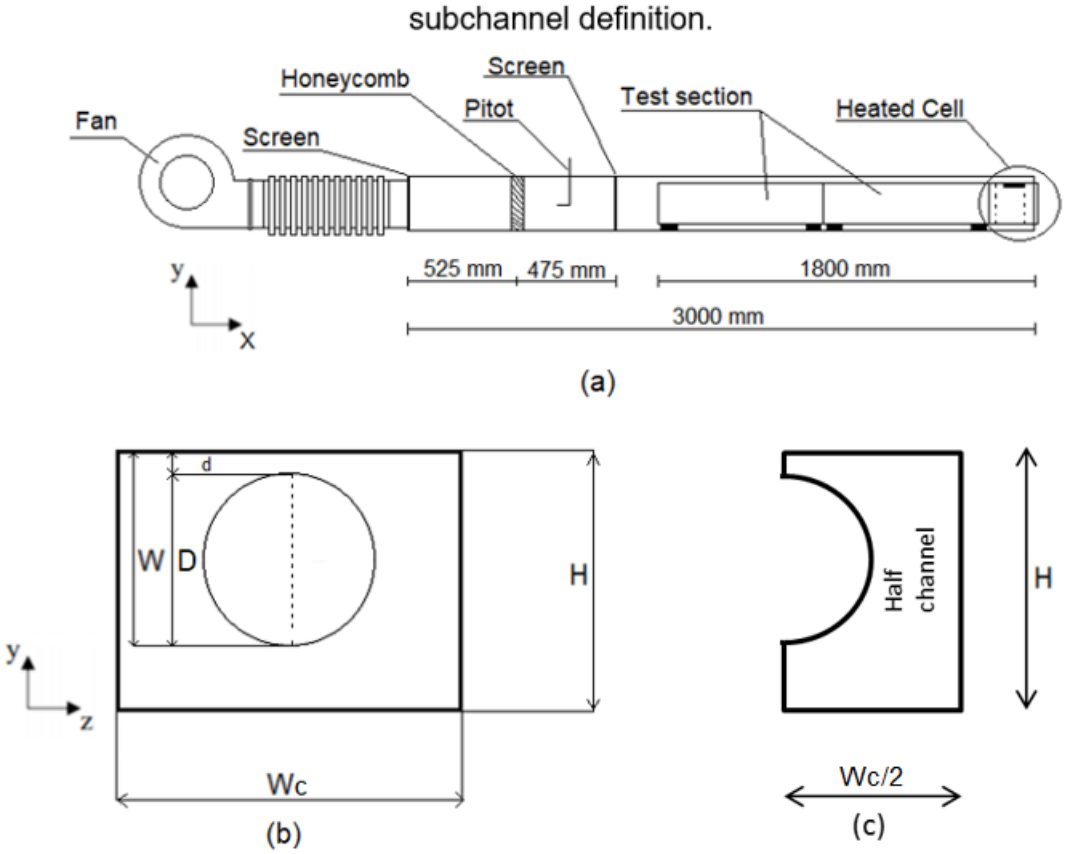

Figure 36 Channel dimensions. (a) Lateral view. (b) Transversal section. (c) Half channel's transversal area.

A Pitot tube is placed at the channel's half height at about 800 *mm* downstream of the channel's inlet. For the fan frequency inverter setting of 50 *Hz*, the reference velocity was, U_{ref} = 9.86 *m/s* for an empty channel. The bulk velocity, U_b, was obtained by measuring, integrating and mapping the mean average axial velocity in the half channel (Fig. 36 c). The integration process was done by creating small areas in the half channel's cross section, then dividing the sum of the flow rates for each of these areas by the total area of the half channel's area, as follows

$$U_b = \frac{\sum_{i=m}^{n} U_V A_V}{A_t} \tag{3}$$

where U_V is the velocity in the center of the small area, A_V is the small area and A_t is the total area of the half channel's cross section. Figure 37 shows the channel's cross section divided in small areas for the bulk velocity calculation. The bulk velocity for each test section, and, therefore, each W/D – ratio was computed as stressed above.

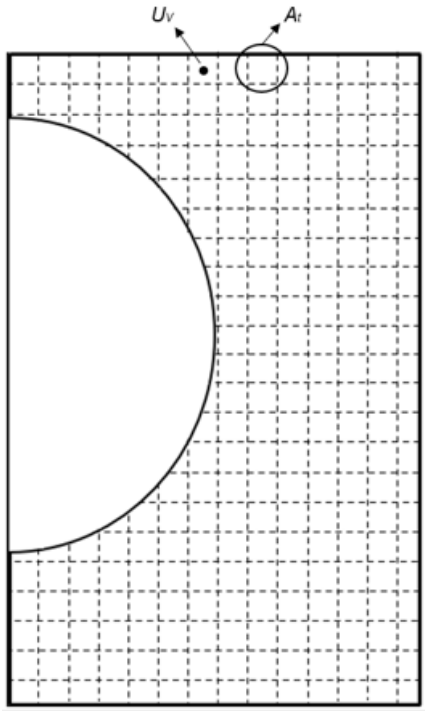

Figure 37 Half channel's cross section divided in small áreas for U_b calculation.

The Reynolds number, based on the bulk velocity (U_b), the hydraulic-diameter (D_h) and the kinematic viscosity (ν), was almost the same for all *W*/*D* – ratios. The hydraulic-diameter was calculated according to eq. (4). The reference velocities for each *W*/*D* - ratio, the bulk velocities and the Reynolds numbers of the experiments are summarized in Table 1.

$$D_h = \frac{4[WcH - ((\pi D^2)/4)]}{2(Wc + H) + \pi D} \tag{4}$$

Table 1 Main settings of the experiments.

n#	*W/D*	U_{ref} – *m/s*	U_b – *m/s*	D_h - *mm*	Re_{Dh}
1	1.050	8.52	8.48	87.35	4.78×10^4
2	1.100	8.75	7.76		4.37×10^4
3	1.150	8.49	8.32		4.69×10^4
4	1.200	8.42	7.71		4.34×10^4

4.2 Flow Measuring Instrumentation

4.2.1 Hot-wire Anemometry

The hot-wire anemometer has a thin metallic sensor heated by an electric current and cooled by the air flow (Comte-Bellot, 1976). Hot-wire anemometers are widely employed in measurements involving turbulent flows due to their very small thermal inertia which makes them a very good technique to gather the velocity fluctuations in such flows.

4.2.2 Constant-Temperature Anemometer

Constant-temperature anemometer works as an active Wheatstone bridge arm (Fig. 38) (Comte-Bellot, 1976). The probe temperature is kept constant and is subjected to cooling due to the flow. This process reduces the resistance, which is powered by the amplifier that increases or decreases the bridge's voltage in order to restore the resistance of the probe. Therefore, the variables related to the flow are gathered from the heat transfer between the probe and the flow (TSI probe catalog).

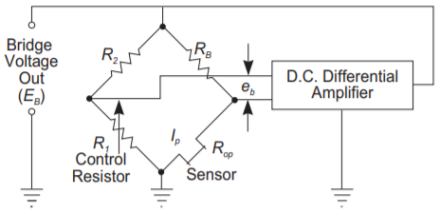

Figure 38 Wheatstone bridge of a hot-wire Constant-Temperature-Anemometer. Source: [TSI probe catalog]

The mean average velocity and the respective fluctuations were measured 20 *mm* upstream of the channel's outlet, using the probe showed in Fig. 39. The signals were sampled at 1 *kHz*, with an acquisition time of 10.242*s*, on the other hand, for spectral analysis the acquisition time was 65.536*s* and a low pass filter was set at 300 *Hz*. All these data were acquired and converted by a 12 bit A/D board. The velocity measurements were performed for an isothermal flow. The calibration data and the uncertainty associated to the hot-wire anemometry can be found in Appendix 1 and 3, respectively

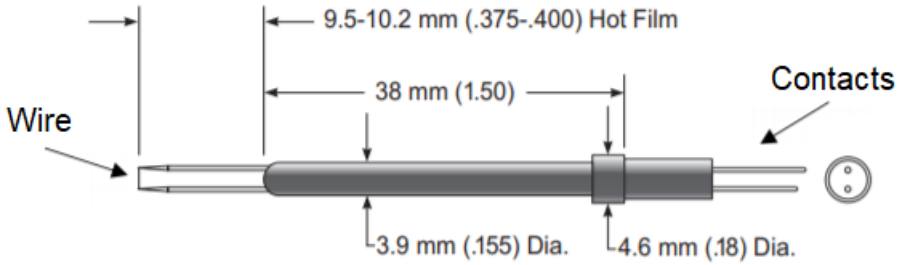

Figure 39 Probe model 1201. Source: [TSI probe catalog]

4.3 Heated Cell

The Heated cell was coupled at the end of the rod, about 200 *mm* of the channel's outlet, as shown in Fig. 40. The heated cell was built in our laboratory and consists of a small cartridge electrical resistance mounted into a copper casting. The heated cell has one side flush with a rod surface and facing the flow (Fig. 40a). The cell's heat exchange area is A_c = 10x40 = 400 mm^2. The other sides are insulated by a thermal blanket and polyurethane foam inside the rod, as seen in Fig. 40b. The cartridge resistance was powered by a MINIPA MPL-3305M electrical supply that, by adjusting the voltage and current, provided a power dissipation, q_f, about 1 *W*. The rod part, where the heated cell is placed, can be rotated around its own axis, then the heated cell was able to assume different angular position, being able to measure the azimuthal distribution of the convective heat transfer.

The temperatures were gathered by five thermocouples placed on the heated cell's surface and in the adjacent region, as shown in Fig. 40a. One thermocouple denominated (1-S) is positioned on the heated cell's surface and four others in the

insulated regions around of the cell. According to Fig. 40, thermocouples are distributed as: right side (2-RS), left side (3-LS), front (4-F), and inner part (5-I). The latter thermocouple is positioned in the bottom of the thermal blanket, about 15 *mm* deep. However, only (1-S) was necessary to determine the convective heat transfer coefficient, the others were used to assess the heat losses by conduction through insulations. The thermocouple (1-S) is an Ômega SA1XL-T-72 and is a band-aid-like. The rest of the thermocouples are all K-type 5TC-GG-K-20-72. The thermocouples locations are indicated by red dots in Fig. 40. All thermocouples were connected to a Novus FieldLogger module, which transfer the temperature data to a computer by a USB cable. The fluid temperature, T_{∞}, was monitored by a K-type thermocouple during all the experiments. The air-conditioning in the laboratory kept the room temperature constant throughout the measurements.

The convective heat transfer coefficient around the rod is determined by,

$$h_{\phi} = \frac{q_{conv}}{A_C\,(T_{(1-S)} - T_{\infty})} \tag{5}$$

where q_{conv}, A_c, $T_{(1\text{-}S)}$ and T_{∞} are respectively the convective heat flux from the cell area exposed to the flow, the cell surface temperature and the fluid temperature. The temperatures were obtained as mentioned above. The convective heat flux, q_{conv}, is related to the heat produced by the cartridge resistance, q_f. Although, q_{conv} is not equal to q_f due to the heat losses (discussed in the next section).

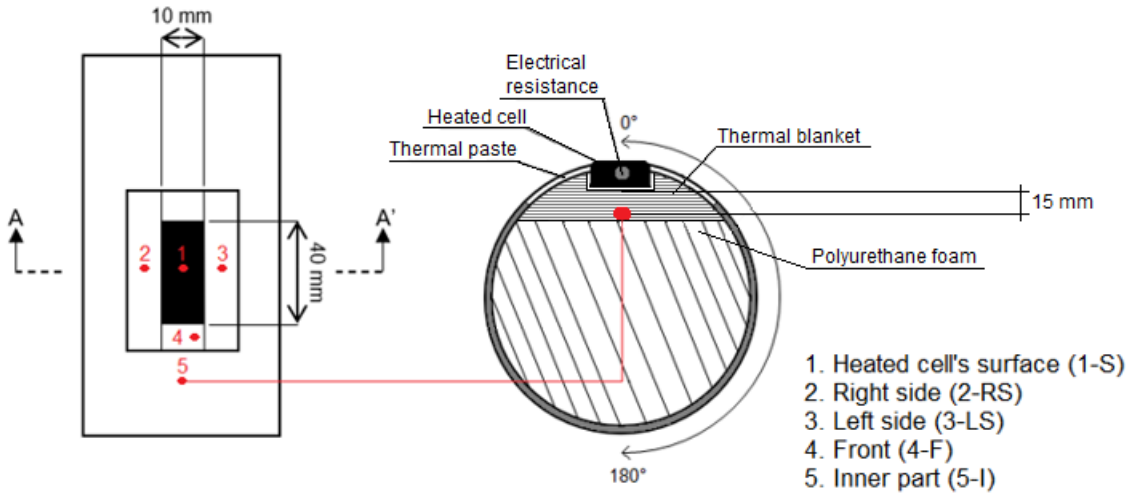

Figure 40 Heated cell. (a) Superior view. (b) Cross section (A-A').

Figure 41 shows the time variation of the temperature for each thermocouple position. In the beginning of the temperature measurement, all thermocouples were reading the room temperature. At 939 *s*, the heater was put on and the temperatures started to rise exponentially. The temperature increasing on the cell's surface (1-S) was the most significant, this occurred due to the high conductivity of the cell's copper body. The other thermocouples showed a much reduced temperature increasing, indicating the efficiency of the insulations around the heated cell. The transitional behaviour of the temperatures started to disappear at about 7038 *s*. At this point, the fan was turned on and the temperatures started to decrease abruptly. The system reaches a new constant temperature at about 8977 *s*. Thus, in order to ensure that the measurements correspond to the steady state, the measurements were read at least 9000 s after starting the heater and the fan. Moreover, an interval of, at least, 2000 *s* between the measurement of temperatures for each change of the heated cell angular position, was considered. The measurements for each *W*/*D* - ratio took about 9 hours.

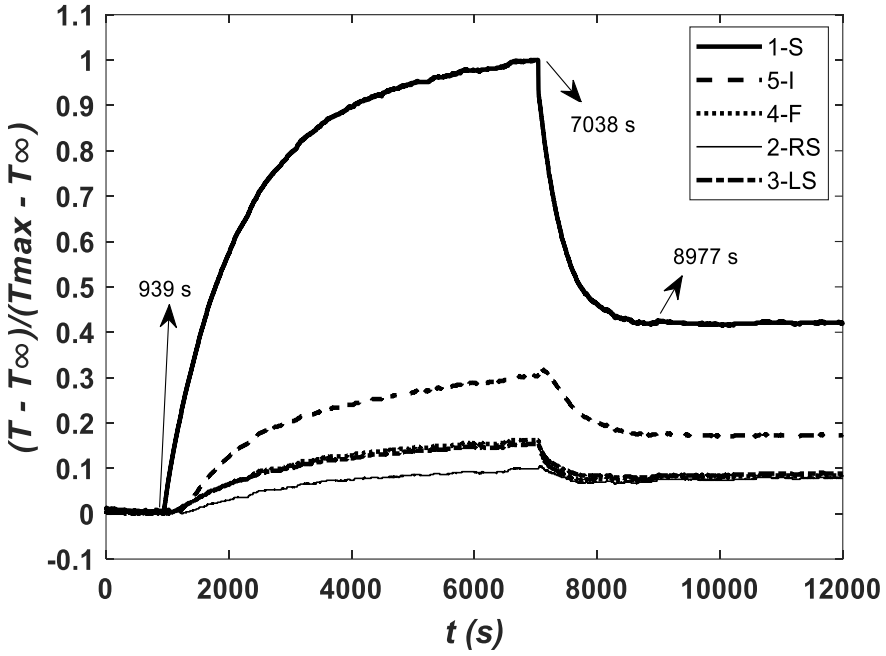

Figure 41 Temperature time-traces measured around the heated cell and it's surface.

The convective heat transfer coefficient around the rod, h_Φ, can be expressed in terms of Nusselt number, based on the on the hydraulic-diameter, D_h, and the air thermal conductivity, k_{air}, as presented by (Guellouz and Tavoularis, 1992, Chang and Tavoularis, 2007 and 2008). Then, the Nusselt number at each angular position, Nu_θ, is scaled by using the average Nusselt number around the rod, $\overline{Nu_\theta}$, providing a spatial Nusselt number variation, ΔNu_θ, as follows:

$$Nu_\phi = \frac{h_\phi D_h}{k_{air}}$$
$$\Delta Nu_\phi = \frac{Nu_\phi}{\overline{Nu_\phi}} \qquad (6)$$

4.3.1 Heat Losses

It was necessary to assess the heat flux at the heated cell's surface in order to evaluate the convective heat transfer coefficient represented by Eq. (5). The heat flux was obtained by the difference between the heat produced by the cartridge

resistance, q_f, calculated using the cartridge voltage and current, and the heat losses by conduction to the heated cell surrounding materials. As shown in Fig. 41, the lateral and frontal thermocouples (2-RS, 3-LS and 4-F) readings were only about 4°C above the room temperature, whereas the cell's surface thermocouple (1-S) showed a temperature difference of 20°C. Simultaneously, the thermocouple placed in the thermal blanket bellow the cell (5-I) showed a temperature around 8.8°C above the room temperature. These temperature distributions, considering the surfaces for the corresponding heat fluxes, indicate that the heat flux is nearly one dimensional. Part of the heat provided by the electrical cartridge is transferred to the flow by convection and the rest, the heat loss, is mainly transferred by conduction through the thermal blanket, as illustrated in Fig. 42.

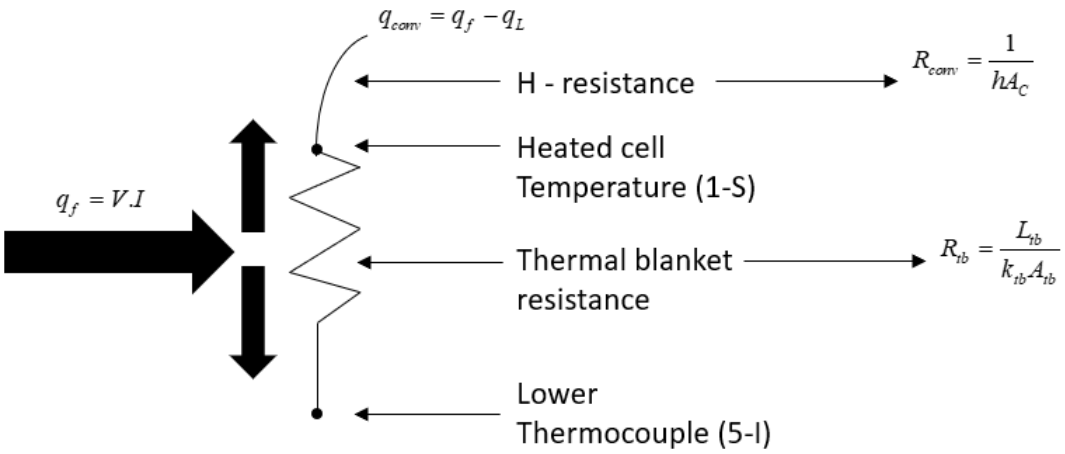

Figure 42 Heat loss model.

Considering the heat loss scheme shown in Figure 42, convective heat transfer is given by

$$q_{conv} = q_f - q_L \tag{7}$$

where q_L is the heat lost by conduction through the cell to the thermal blanket. It is given by

$$q_L = \frac{T_{(1-S)} - T_{(5-I)}}{R_{tb}} \tag{8}$$

$T_{(1\text{-}S)}$ and $T_{(5\text{-}I)}$ are the temperatures at the cell's surface and at the thermal blanket bottom, respectively. R_{tb} is the thermal resistance between the thermal blanket and the heated cell, given by

$$R_{tb} = \frac{L_{tb}}{k_{tb} A_{tb}} \tag{9}$$

where k_{tb} = 0.04 *W/mK*, is the thermal conductivity of the thermal blank, A_{tb} = 0.0004 m^2, is the contact area between the heated cell and the thermal blank and $L_{tb.}$ = 15 *mm* is the thermal blanket thickness (distance from the cell's bottom surface up to the thermocouple).

In this sense, Rconv is the thermal resistance between the heated cell and the air flow, given by

$$R_{conv} = \frac{1}{h_{\phi} A_C} \tag{10}$$

where h_{Φ} and A_c are as defined in Eq. (4).

Equation (10) is a combination of eqs. (5) to (10). It yields the convective heat transfer coefficient in terms of the measured temperatures and heat generation.

$$h_{\phi} = \frac{q_f}{A_C \left(T_{1-S} - T_{\infty}\right)} \left(1 - \left[\frac{k_{tb} A_{tb} \left(T_{1-S} - T_{5-I}\right)}{q_f L_{tb}} \right] \right) = \frac{q_f}{A_C \left(T_{1-S} - T_{\infty}\right)} \left(1 - r_L\right) \tag{11}$$

The fraction of the generated heat lost by conduction is expressed between square brackets and is represented by r_L. The assessment of this term for all performed measurements (Fig. 43) shows that its variation with the angular position, for all *W/D* – ratios, is between 0.98% and 1.28%, with an average about 1.1% of q_f. These values are substantially smaller than the uncertainty calculated for the convective heat transfer measurements, about 20%, as shown in Appendix 3. Moreover, it can be supposed that the losses are a constant percentage of the generated power due to the small values of r_L. So, in this sense, ΔNu_{θ} does not need

correction for the losses, because the average and local values are affected in the same way.

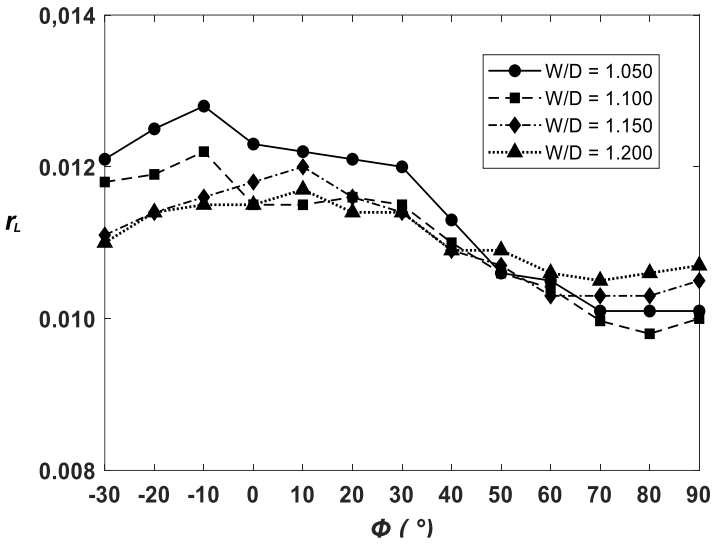

Figure 43 Heat loss ratio (r_L) estimate for all measured *W*/*D* – ratio.

4.4 Skin Friction Coefficient

The skin friction coefficient around the rod was experimentally measured for *W*/*D* = 1.050, 1.100, 1.150 and 1.200, and was assessed in order to verify its relationship with the convective heat transfer. In this sense, the wall shear stress was measured using a Preston tube with a diameter d_p= 2 *mm* and a length of 170 *mm* and the calibration process was performed following the methodology found in Ota et al. (2013). The pressure difference data was gathered by using a Dwyer DM-2000 Pressure Transmitter and a POL-79C bench multimeter. The skin friction measurements were performed for an isothermal flow.

For the calibration procedure brought by Ota et al. (2013) is necessary to use a circular pipe to perform the Preston's tube calibration. So, in the present work, for the calibration process, the rod inside the rectangular channel used in the experiments was removed and replaced by a pipe of D_P = 52 *mm* diameter, with a total length of L_T = 2700 *mm*, as shown in Fig. 44. The static pressure drop, ΔP, along the pipe was obtained by using two points pressure measurements (termed as P1 and P2) separated by a distance L_{SP} = 1180 *mm*. The distance between the pipe inlet and P1

is 1040 *mm* ($20D_P$), the distance necessary to have a fully developed turbulent flow in a circular pipe for a Reynolds number order of 10^4, according to White (1999). Figure 44 also shows the Preston's tube positioned at 30 *mm* upstream the pipe's outlet and the locations of measurement of the difference between the Preston's tube and the static pressure in the pipe, $\Delta P_{Preston}$.

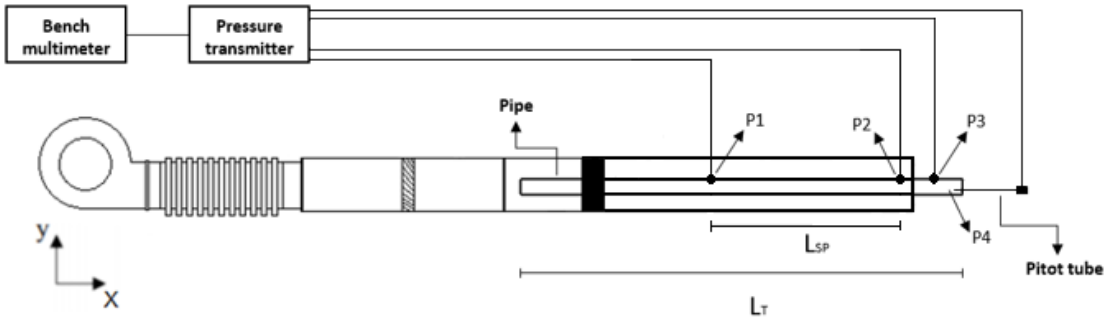

Figure 44 Scheme of the Preston's tube calibration.

Firstly, the pressure drop, ΔP, between P1 and P2 in the pipe was obtained, from which the reference values for the wall shear stress, τ_w, was calculated. The normalized wall shear stress, τ^+, was then determined.

After the measurements in the pipe, it was performed the measurement of the difference between the Preston's tube and the static pressure in the pipe, $\Delta P_{Preston}$, between the points P3 and P4 (Fig. 44). So, by using this $\Delta P_{Preston}$, the normalized pressure difference, ΔP^+, was computed. The calibration fitted equation of τ^+ as a function of ΔP^+ can be found in appendix 2, as well as the equations used, measurements and calibration curve.

5 RESULTS

5.1 Mean Velocity and *u*-RMS

The mean axial velocity and the u-RMS were measured experimentally in order to assess the influence of the narrow gap on the mean flow field and the velocity fluctuation distribution. Figure 45 a-d shows the distribution of the mean average axial velocity in half channel's cross section, whereas Fig. 46 a-d shows the corresponding *u*-RMS distribution. The isocontour of the mean velocity and the *u*-RMS were scaled by the bulk velocity, U_b, and are denoted $\overline{U}/U_b$ and $\sqrt{\overline{u'^2}}/U_b$, respectively.

The mean axial velocity distributions, for all *W*/*D* cases, are in qualitatively good agreement with the isocontours found in Wu and Trupp (1993), Guellouz and Tavoularis (2000a), Goulart et al. (2016) and Severino et al. (2018). Furthermore, as effect of the secondary flows, the isovels of the valocity's maps bulges towards the corners, something that normally happens in corners of noncircular channels.

Moreover, strong velocity gradients were observed in the gap vicinity for all *W*/*D* – ratios, as shown by the bending of the isocontours towards the main channel. In spite of this, no substantial differences were found in the mass distribution in the center of the subchannel. The maximum value for the axial velocity is around $\overline{U}/U_b$ = 1.30 for *W*/*D*=1.050, 1.100 and 1.200. It is found in the central region of the subchannel, near the dashed equidistant line between the rod and the channel wall at about 60°. For *W*/*D* = 1.150, the maximum velocity was $\overline{U}/U_b$ = 1.20, a little smaller in comparison to the other *W*/*D* – ratios. These results are in fair agreement with the values obtained by Guellouz and Tavoularis (2000) and Severino et al. (2018). The minimum values of the average axial velocity occur in the gap region and increase with the gap width, promoting changes in the mass flow distribution in the narrow gap.

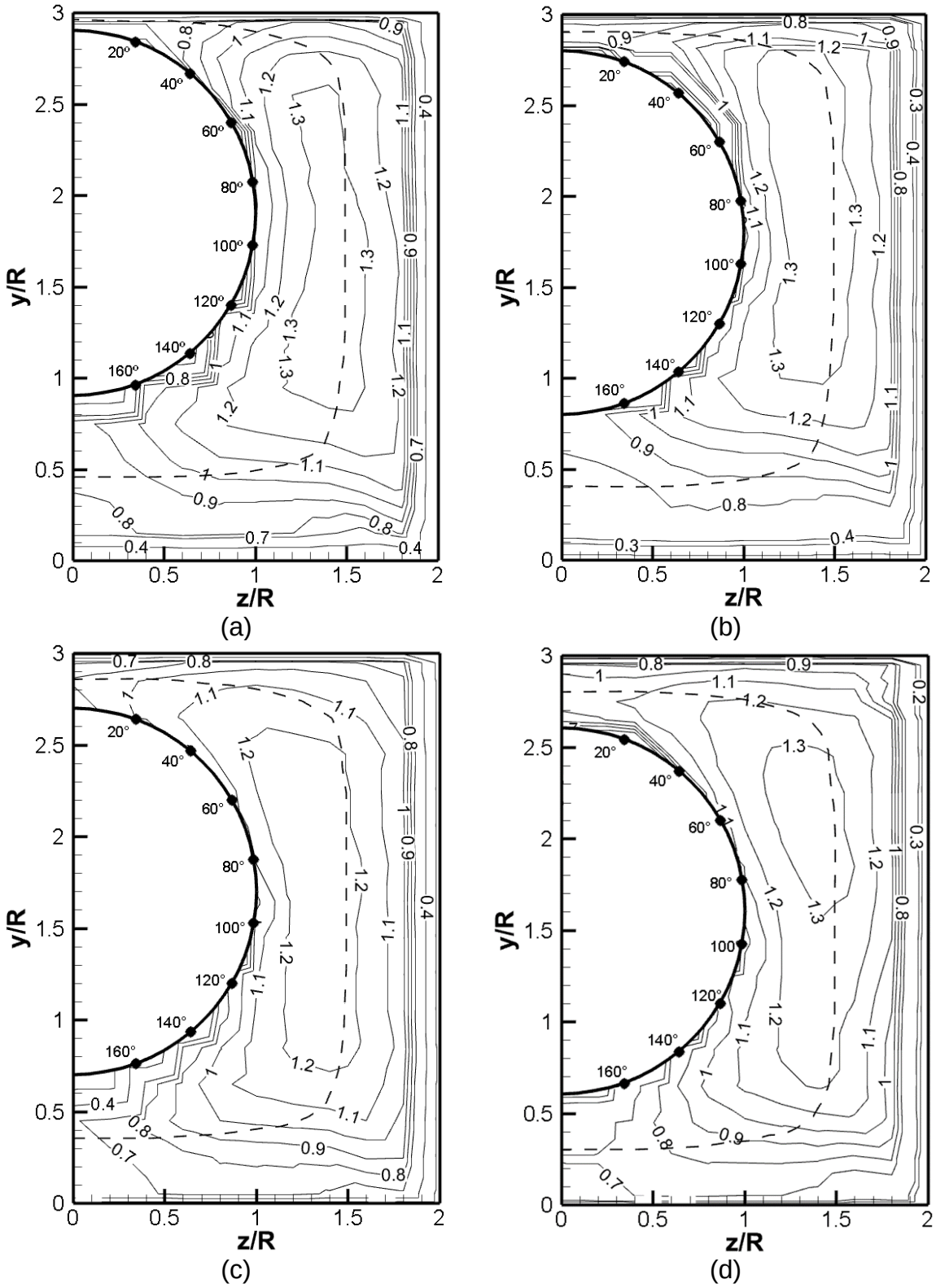

Figure 45 Isocontours of the average axial velocity, $\bar{U}/U_b$. (a) *W*/*D* = 1.050. (b) W/D = 1.100. (c) *W*/*D* = 1.150. (d) *W*/*D* = 1.200.

The experimental *u*-RMS results show very different distributions, Fig. 4 6a-d. The gap width seems have a strong influence on the fluctuant velocity field distribution.

Far from the narrow gap, for all *W*/*D* – ratios, the minimum value of *u*-RMS, $\sqrt{\overline{u'^2}}/U_b$ = 0.05, is found at almost the same position of the highest mean axial velocity, which takes place at about 60°. Furthermore, in open areas the velocity gradients are very small, promoting, therefore, lower Reynolds stresses. The presence of a closed contour maxima near the gap region is the remarkable feature of the *u*-RMS distribution, especially for *W*/*D* = 1.050 and 1.100. The maximum values of the fluctuating field for *W*/*D* = 1.050 and 1.100, at about 40°, are around 0.14 and 0.12. For the highest gaps, *W*/*D* = 1.150 and 1.200, the maximum *u*-RMS are 0.8 and 0.85, also around 40°. The peak values of the *u*-RMS near the gap region are currently reported by many authors who carried out numerical and/or experimental studies of the fluctuating flow field intensity in several different configurations of compound channels (Meyer and Rehme (1994), Home et al., (2009), Merzari et al., (2008), Home and Lightstone (2014), Candela et al., (2020)).

Quantitatively, excellent agreement was also observed with the results for the fluctuations presented by Guellouz and Tavoularis, (2000a) and Severino et al. (2018), who performed the same kind of measurements for *W*/*D* = 1.100. The mentioned authors obtained values ranging from 0.06 up to 0.014, with the same maximum value at almost the same position.

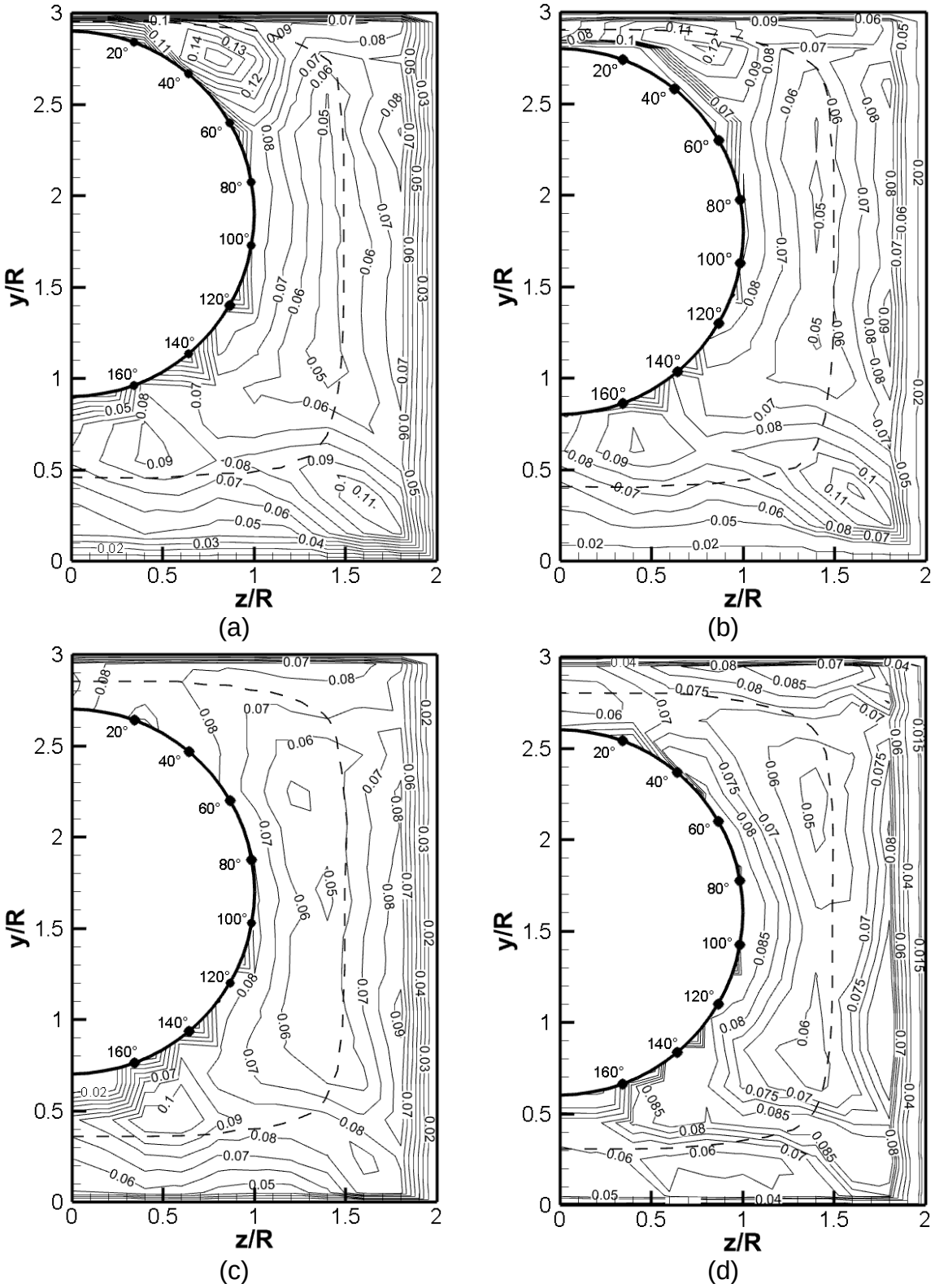

Figure 46 Isocontours of the *u*-RMS, $\sqrt{\overline{u'^2}}/U_b$. (a) *W*/*D* = 1.050. (b) *W*/*D* = 1.100. (c) *W*/*D* = 1.150. (d) *W*/*D* = 1.200.

5.2 Frequency and Reference Velocity Correlation

In this section, a verification of the relationship between the main frequency of the velocity fluctuation signals and the reference velocity (U_{ref}) was carried out. This verification and the frequency maps of the next section were made only for *W*/*D* = 1.050 and 1.100, because large-scale coherent structures are more associated to small gap spacings. The hot-wire probe was placed in the test section according to Fig. 47 (a) and (c). These locations were selected, because in these regions, near the gap, Möller (1991) and Severino (2018) found large turbulent structures, confirmed by the quasi-periodic signals shown in Fig. 47 (b) and (d). For the *W*/*D* = 1.050, the reference velocities considered were 2.25 *m*/*s*, 5.72 *m*/*s* and 9.10 *m*/*s*; and the related Reynolds numbers, obtained used the mentioned reference velocities, were 23676, 60191 and 95758. In the *W*/*D* = 1.100 configuration, the reference velocities were 2.12 *m*/*s*, 5.91 *m*/*s* and 9.52 *m*/*s*; corresponding to the Reynolds numbers 22308, 62190 and 100180. The data were sampled at 1000 *Hz*, low pass filtered at 300 *Hz*, with a number of points of the signal of 65536, corresponding to an acquisition time of 65.536 *s*.

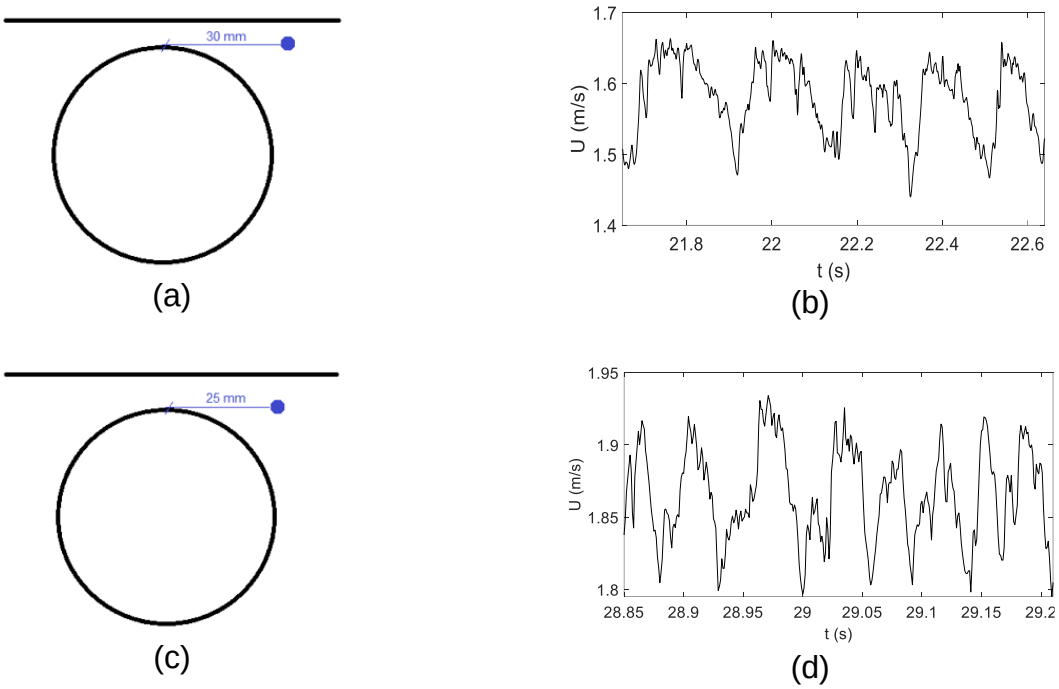

Figure 47 *W*/*D* = 1.05: (a) Probe location. (b) Axial velocity time-trace. *W*/*D* = 1.10: (c) Probe location. (d) Axial velocity time-trace.

Figure 48 shows the relationship between the main frequency from the spectral analysis and reference velocity for *W*/*D* = 1.050 and *W*/*D* = 1.100 cases, respectively. It is obvious, at first glance, that the frequency of the coherent structures was raised as the reference velocity was increased. This finding is consistent with the results presented by Möller (1991) and Rowe et al. (1974). For the first arrangement, *W*/*D* = 1.050, the frequencies were ranged from 3.91 *Hz* up to 30.27 *Hz*, whereas in the second one, *W*/*D* = 1.10, the frequencies were found to range from 4.84 up to 30.27 *Hz*. The frequency for the highest velocities did not change with the gap. This fact does not completely agree with the literature, which shows that the frequency decreases with increasing gap widths.

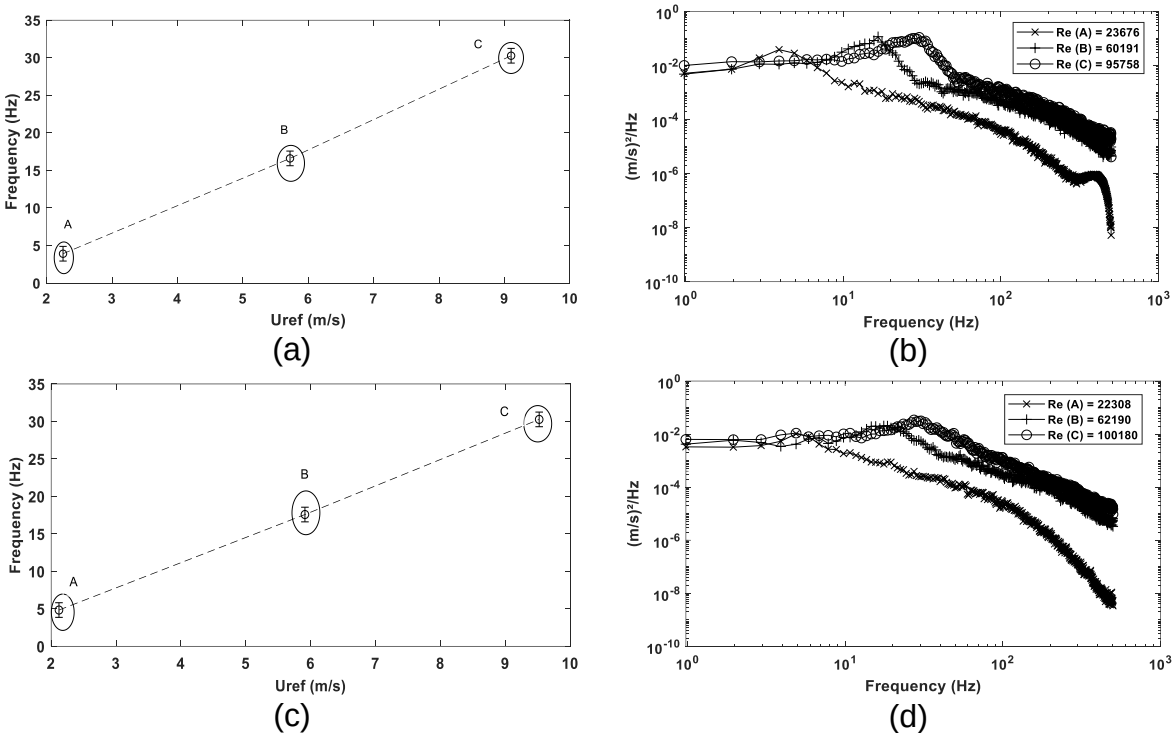

Figure 48 *W*/*D* = 1.05: (a) Correlation between frequency and reference velocity. (b) Power spectra density. *W*/*D* = 1.10: (c) Correlation between frequency and reference velocity. (d) Power spectra density.

5.3 Frequency Map

Now, a frequency map of the same channel section will be presented. This kind of map is important to find out the locations where the dominant frequencies of the velocity fluctuations are most pronounced. In the narrow gap, due to instabilities,

large scale coherent structures form, and produce quasi-periodic patterns in the velocity time-traces (Rowe et al., (1974); Möller (1991); Melo et al., (2017) and Severino et al., (2018). The periodical behaviour of the velocity signals are then the footprints of these coherent structures and can be seen in the dominant frequencies of the velocity fluctuations. This frequency depends on the gap geometry and the flow velocity (Möller (1991) and (1992)).

Figure 49 shows the axial velocity time-traces for three kinds of spectra observed in the frequency maps of Figs. 50. These velocity signals are presented in order to show the presence of the large-scale coherent structures in the regions of the channel where the spectra of the frequency map was measured. As can be seen in Figure 49, three kinds of signals were gathered for W/D = 1.050 and W/D = 1.100, indicating three different spectra found in channel's interest section. The fluctuation pattern in Fig 49 (e) have the signal with the most regular periodicity for W/D = 1.050 and (f) shows a similar behaviour of the axial velocity fluctuation for W/D = 1.100. This denotes the existence of dominant frequencies. On the other hand, the signals in Fig. 49 (a) and (b) present a random behaviour, it means, diffuse turbulent motion only. These signals are representative of regions with no dominant frequencies in the velocity fluctuation. The velocity time traces shown in Figure 49 (c) and (d), for W/D = 1.050 and W/D = 1.100, are the intermediaries in terms of the periodicity of the signal. These velocity signals show the significant influence of the W/D on the flow dynamics, especially the contribution to the formation of instabilities characterized by the well-defined periodicity observed in the signals of the smaller gap (W/D = 1.050).

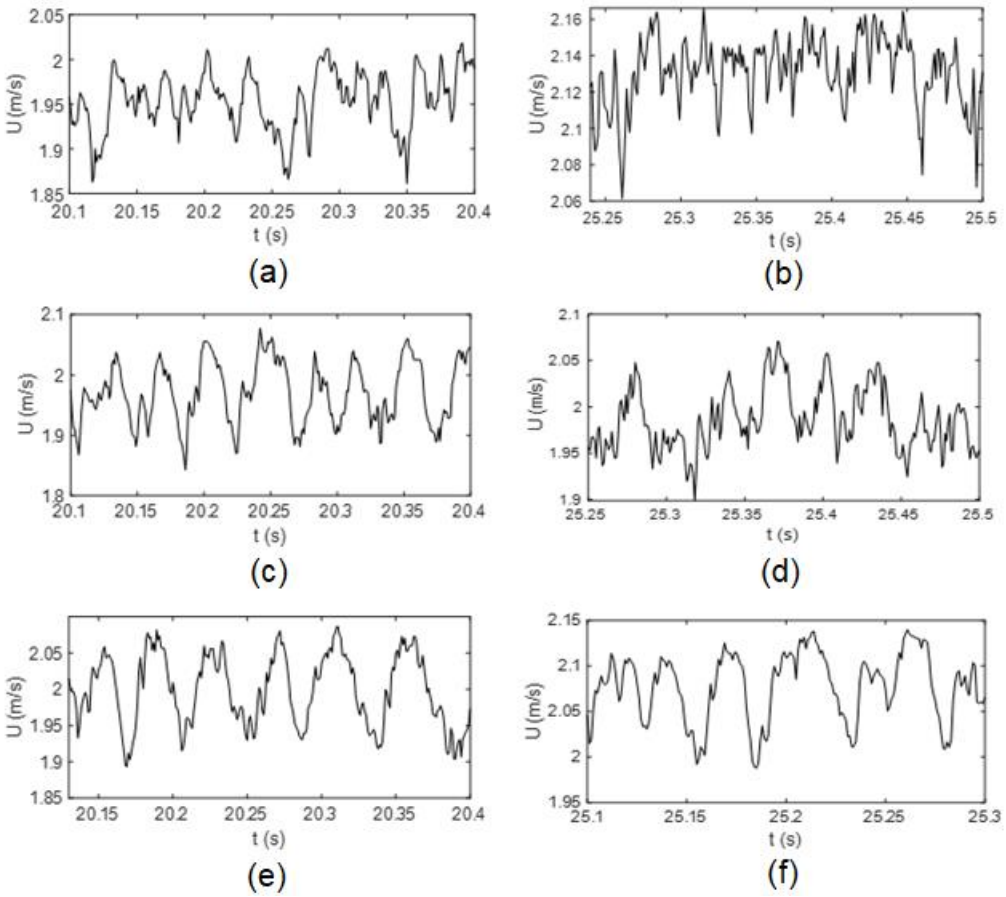

Figure 49 Axial velocity time-traces for *W*/*D* = 1.050 (a-c-e) and 1.100 (b-d-f).

In Fig. 50 (a) shows the region of the channel where the spectra were measured in 26 points and (b) presents the three kind of spectra found in that region of the channel for *W*/*D* = 1.050. The bandwidth for these three spectra types was 0.97 *Hz*. The points were measured according to grid spacing with 10 *mm* in the vertical direction, *Δy*, and horizontal direction, *Δx*. In Fig.50 (a), the spectra with the highest frequency peak, type (3) in Fig. 50 (b), is more common in regions near the tight gap, where the instabilities take place, in agreement with the literature (see authors mentioned in the beginning of the present section). The type (1) spectra shown in Fig. 50 (b) has no frequency peak and are present mostly away from the gap i.e. in the widest region of the flow. For the *W*/*D* = 1.050 case, the peak frequencies for the type (3) spectra were 28.32 *Hz*.

Figure 50 (c) shows the measuring spectra points in the interest region of the channel for *W*/*D* = 1.100 and in (d) are plotted the spectra kinds seen in that region.

A total of 30 points was measured. The grid points are spaced in the vertical direction, Δy = 10 *mm* between, whereas for the horizontal direction, Δx, the points are spaced 5 mm from each other. As expected, the spectra with highest peak, type (3), are found essentially in the regions near the gap, around 5 *mm* up to 10 *mm* away from the gap center, and sometimes right in the middle of the gap. The spectra with no peak, type (1), was observed far from the gap region, around 60°. The peak frequency for the type (3) spectra was 29.30 *Hz*.

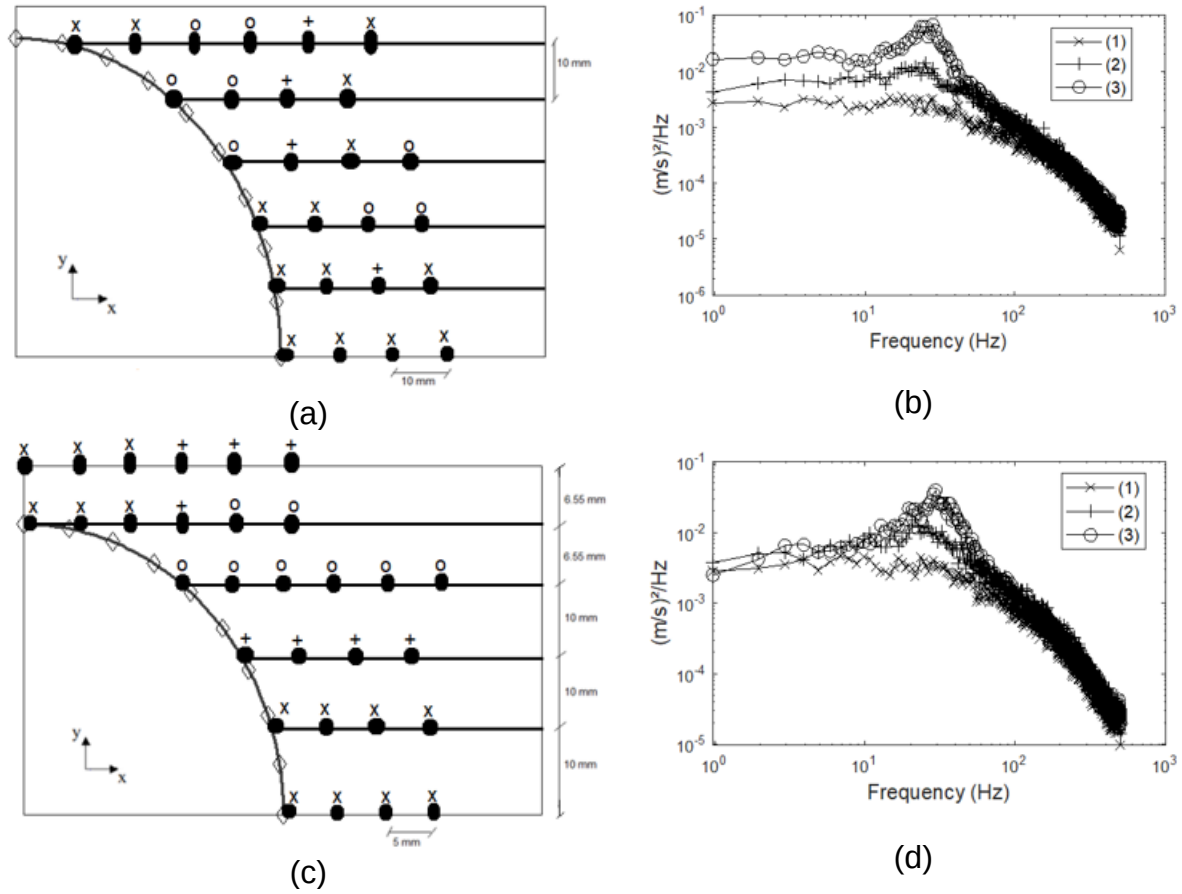

Figure 50 Frequency map. *W*/*D* = 1.050: (a) Points in the section. (b) Points corresponding spectra. *W*/*D* = 1.100: (c) Points in the section. (d) Points corresponding spectra.

5.4 Spectral Analysis

The appearance and behaviour of the large-scale coherent structures can be studied through the spectral analysis and the autocorrelation of the streamwise velocities. The spectral density functions for all investigated *W*/*D* – ratios are shown

in Fig. 51 (a-c) where the frequencies (*Hz*) are represented in the x-axis, while the specific power per bandwidth (m^2/s) is in the y-axis and is determined by eq. (12).

$$P_{xx(f)} = \left| \frac{1}{2\pi} \sum f_{(t)} e^{-ift} \right|^2 \tag{12}$$

Figure 51 (d) shows the spectral density plotted against a non-dimensional form of the frequency, represented by the Strouhal number, based on the rod diameter (D) and on the bulk velocity (U_b) and the fundamental frequency (f). In the y-axis, ψ is the specific power per bandwidth and was also made dimensionless by using the same scales, as follow in eq. (13),

$$St = \frac{f\,D}{U_b}$$
$$\psi = \frac{P_{xx(f)}}{DU_b} \tag{13}$$

The power spectra for different position in the channel for all *W*/*D* – ratios are shown in Fig. 51 (a-b). Some of these spectra show peaks. The sharpest ones are at the vicinity of the narrow gap region (Fig. 51 (a)), but not right inside of it. For positions near the subchannel central region (Fig. 51 (b)), the magnitude of peaks starts to decrease and vanish. The *z*/*D* ratio is the position where the spectra of the streamwise velocity were measured, *z* is the transversal coordinate and *D* is the rod's diameter.

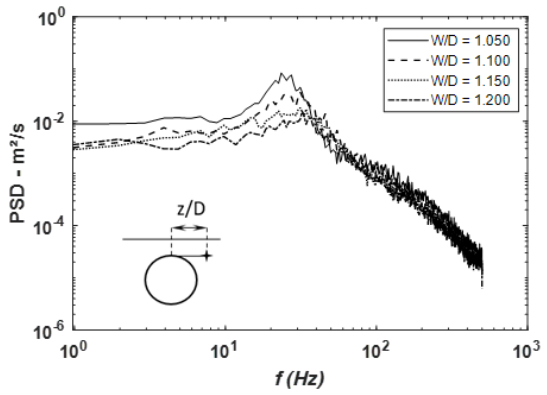

(a)

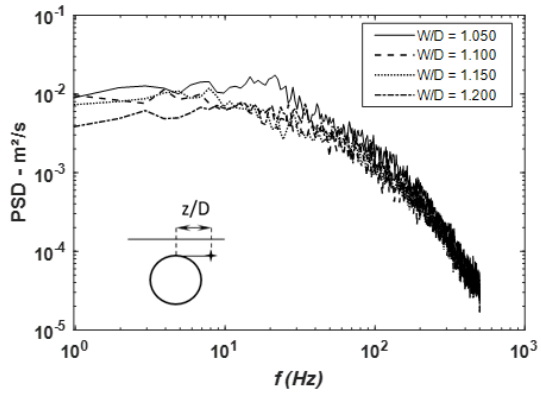

(b)

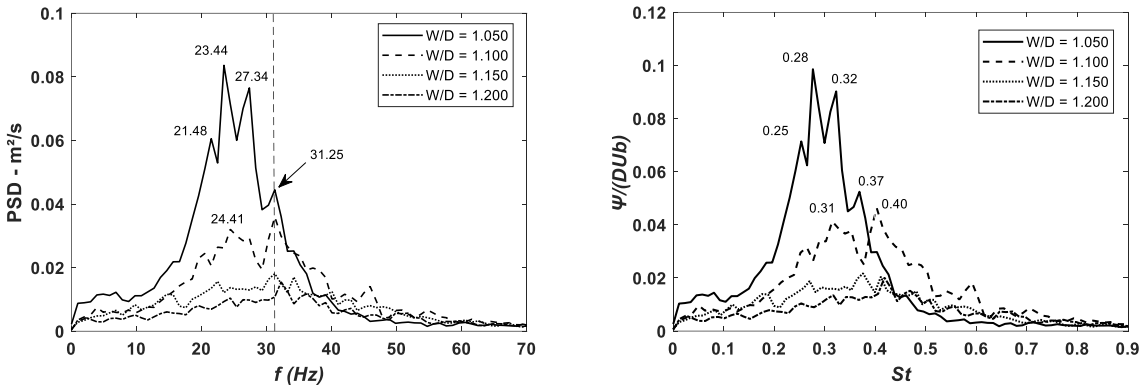

(c) (d)

Figure 51 Spectral response of the axial velocity fluctuation for *W*/*D* = 1.050, 1.100, 1.150 and 1.200 and respectively at positions: (a) *z*/*D* = 0.25, 0.30, 0.30 and 0.30. (b) *z*/*D* = 0.35, 0.40, 0.40 and 0.40. c) Linear plot for *z*/*D* = 0.25, 0.30, 0.30 and 0.30. (d) Dimensionless spectra for *z*/*D* = 0.25, 0.30, 0.30 and 0.30.

Figure 51 (a) shows sharp and broad peaks. They were observed in the symmetry line of the narrow gap near the rod at *z*/*D* = 0.25, 0.30, 0.30 and 0.30 from the central region. No peaks were seen right inside the gap center. Möller (1991) observed the same behaviour for the spectra of the axial velocity in his results. The positions where the most prominent peaks were found near the regions of the highest values of *u*-RMS (Fig. 46 (a) and (b)) and, also, correspond to the locations where the large-scale vortices have their velocities in the streamwise direction, according to the model proposed by Guellouz and Tavoularis (2000b). The mentioned authors presented a model for the coherent structures that occurs in the narrow gap between a cylinder and a plane wall, which is characterized by a street of three-dimensional counter-rotating vortices with the axis alternating between the sides of the symmetry plane.

The observation of the main frequency in the log-log spectra graph is not so easy for *W*/*D* = 1.050 and 1.100 due to the broad peaks observed in these cases. In order to better observe the main frequencies, it was decided to show the spectra in linear form, Fig. 51 (c). From this figure, at first sight, it can be noticed that the frequency peaks were not present for the largest W/D - ratios (1.150 and 1.200). The energy of the signal at the bandwidth for *W*/*D* = 1.100, 1.150 and 1.200 is almost one order lower in comparison with *W*/*D* = 1.050. The most prominent peaks were observed for *W*/*D* = 1.050 and 1.100. Figure 51 (c), if carefully observed, shows

different peaks containing different amount of energy occurring at almost the same frequency. In spite of some scattering of the frequencies, with high levels of energy, the frequencies related to quasi-periodic motions were found about 24 *Hz* for *W*/*D* = 1.050 and 1.100. It is important to note that, as the *W*/*D* – ratio increases, the energy peaks seem to broaden and become less prominent. According to previous works, the peaks become smaller as the relative strength of the structures decreases. The broadening of the peak can be associated with the size variation of the vortices that become more pronounced for larger *W*/*D*, as explained by Guellouz and Tavoularis (2000a).

The spectra for the locations *z*/*D* = 0.35, 0.40, 0.40 and 0.40 (far from the gap) are shown in Fig. 51 (b). These spectra did not show any peak, indicating no evidence of periodic motions. Figure 51 (d) presents the non-dimensional spectra, showing the Strouhal numbers for different W/D – ratio. The Strouhal number was determined using Eq. (11). According to Tavoularis and Chang (2007), the rod diameter (*D*) is more appropriate to calculate the Strouhal number than the hydraulic diameter (D_h). The scattering observed in the frequency values also affected the Strouhal number. For *W*/*D* = 1.050 and 1.100, the Strouhal number was about 0.30, however, small sided peaks were found in the spectra. It is important to mention that the calculated Strouhal numbers are significantly higher than the values found in the literature, where the presented Strouhal number was around *St* ~ 0.20. An alternative way to estimate the fundamental frequency of the coherent structures can be obtained from the velocity autocorrelation functions shown in Fig. 52. The autocorrelation coefficients were found by using eq. (14).

$$Coeff\,(t) = \frac{u(t)u(t+\Delta t)}{u^2(t)} \tag{14}$$

The autocorrelation coefficient was significant higher for *W*/*D* = 1.050 in comparison to the other gap spacings. This behavior, according to Goulart et al., (2016), implies that the large-scale structures strongly dominate the flow in the narrow regions of the channel. Also, for the lowest gaps, especially for *W*/*D* = 1.050, a more periodic behavior with high exponential decays was observed. This

characteristic, according to Rowe et al., (1974), indicate that the power spectra have a dominant frequency, as shown in Fig. 51 (a) and (c) for *W*/*D* = 1.050 and 1.110. The frequencies obtained from the autocorrelation functions were 26.31 *Hz*, 30.30 *Hz*, 31.25 *Hz* and 32.25 *Hz* for *W*/*D* = 1.050, 1.100, 1.150 and 1.200, respectively.

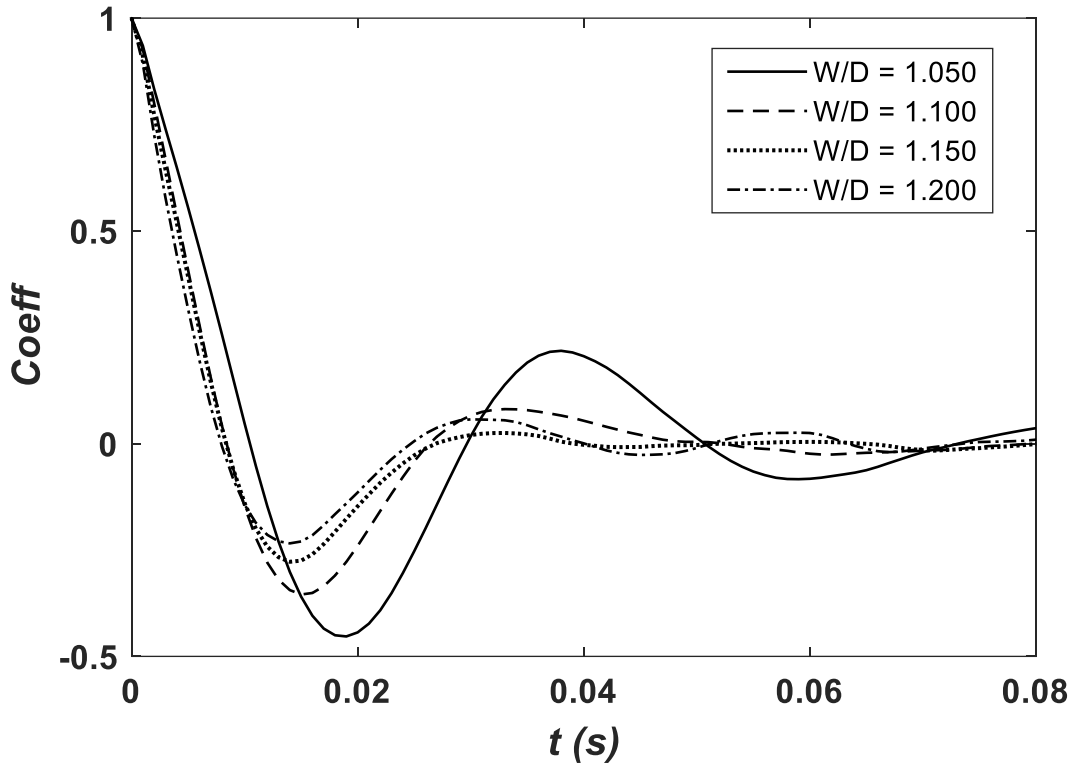

Figure 52 autocorrelation functions of the axial velocity fluctuation for different gap sizes, evaluated at *y*/*D*=*d*/2*D* and *z*/*D* = 0.30.

The Strouhal number, based on the bulk velocity, obtained using the frequencies from the autocorrelation function are 0.31, 0.39, 0.38 and 0.42 for respectively *W*/*D* = 1.050, 1.100, 1.150 and 1.200. These values are significantly higher than the values found by previous researchers, about *St* ~ 0.20. The most similar configurations to the present flow geometry are those studied by Guellouz and Tavoularis (2000a) and Severino et al. (2018). The former used geometry with different aspect ratio from the present with a rectangular channel height equal to 2*D* and width equal to 3*D*, whereas the latter performed the experiments in the exactly same channel geometry as the present, although using a hollow cylinder instead of the full rod. The Strouhal number differences could be explained by the differences in the flow distribution in

the channel producing larger flow velocities in the narrow gap region and therefore higher frequencies for the vortices. This hypothesis was corroborated by an observation of the isovels the gap vicinity, which have values higher than the obtained by Guellouz and Tavoularis, (2000a) and Severino et al., (2018). Taking this into account, it was decided to perform a new experimental campaign in order to obtain the spectral response of the flow, but now using the empty rod (hollow rod bundle) instead, as used by Severino et al. (2018) and Severino (2018). Figure 53 (a-c) shows the spectra for all *W*/*D* – ratio, considering the same *z*/*D* of Fig. 51, but this time using a hollow rod.

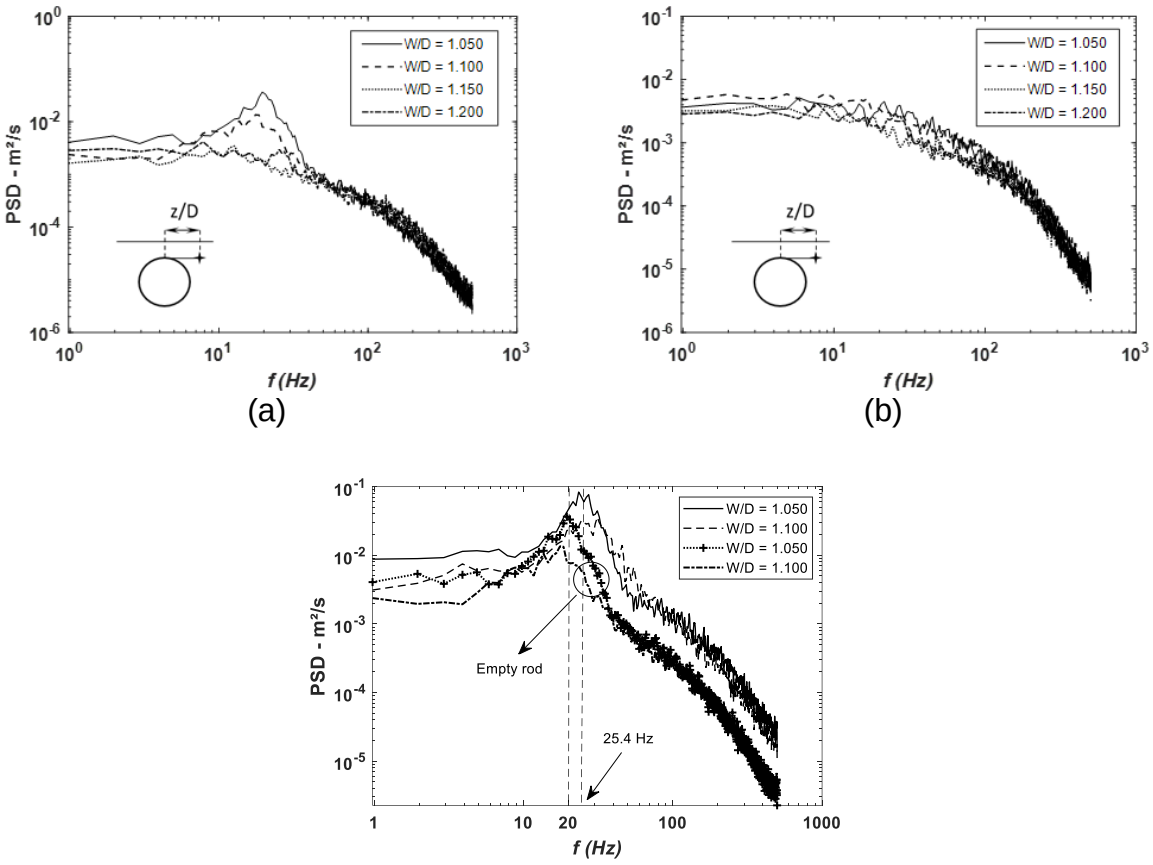

Figure 53 Spectral analysis of the axial velocity fluctuation for a hollow rod. a) *z*/*D* = 0.25, 0.30, 0.30 and 0.30. b) *z*/*D* = 0.35, 0.40, 0.40 and 0.40. c) comparison between the spectral response hollow and non-empty rod.

Firstly, the same spectra features are obtained in this case as in the channel with the non-empty rod. For *W*/*D* = 1.050 and 1.100, prominent peaks can be

observed, whereas for *W*/*D* = 1.150 and 1.200, no peaks can be seen in the spectra. The fundamental frequencies for *W*/*D* = 1.050 and 1.100 were 19.53 *Hz* and 18.55 *Hz*, respectively. The frequency and the height of the peak decreases as the gap width (*W*/*D*) increases, as also presented by Rehme (1987) and Wu and Trupp (1993). The Strouhal numbers obtained in the new experimental campaign were 0.23 and 0.20 for *W*/*D* = 1.050 and 1.100, respectively. These values are in agreement with those provided in the literature (Guellouz and Tavoularis (2000a), Severino (2018) and Severino et al., (2018)). These differences in terms of Strouhal number in comparison to the found for the closed rod, can be associated to a mass flow redistribution that change the frequency values.

5.5 Temperature and Nusselt Number Distribution Around the Rod

The distribution of the wall temperature around the rod from 0° (narrow gap) up to 90° (horizontal position) is shown in Fig. 54 (a). The wall temperature was scaled by the difference between the average temperature around the rod, $\overline{T}$, and the room temperature, $\overline{T}$-$\overline{T}_\infty$, according to Eq. (15).

$$T_\phi = \frac{\overline{T_{w(\phi)}} - \overline{T_\infty}}{\overline{T} - \overline{T_\infty}} \tag{15}$$

As mentioned before, the rod can be rotated around its own axis, then the band-aid-like thermocouple can be positioned at different angular positions in order to allow the measurements of the distribution of the heat transfer coefficient around the rod's circumference. After each change to a new angular position of the heated element, a waiting period of about 2000 *s* was allowed before gathering the first reading. This is to ensure that the new stationary thermal condition had been achieved at the new position. The temperature of the flow, T_∞, was monitored by a thermocouple positioned inside the channel and was essentially constant for all measurements. The temperature of the flow for *W*/*D* = 1.050, 1.100, 1.150 and 1.200 were 22.97°*C*, 22.89°*C*, 23.02°*C* and 23.04°*C*, respectively. The heat provided by the cartridge of the heated element, q_f, was kept constant during all the experiments.

In order to verify the symmetry of the flow and the heat transfer, the temperature distribution was taken for negative angles (i.e. in the opposite subchannel). Figure 54 (a) shows that the temperature distribution presents a good symmetry over the interval of -30°< ϕ < 30° for all *W*/*D* studied. The highest values of the temperature are near the narrow gap, regardless of gap spacing. As the angular position increases, the temperature decreases. The local Reynolds number increases as the narrow gap becomes wider (Groeneveld, 1973, Chang and Tavoularis (2008)), which increases the local convective heat transfer and, therefore, decreases the temperature around the rod's wall.

It is important to note that the maximum temperature does not take place in the central region of the narrow gap (0°), but very close to it. For *W*/*D* = 1.050 and 1.100, the highest values of the temperature were around ϕ =10° (also at -10°). It must be noticed that the locus of the lowest temperature does not coincide with the region that present the highest energy of the fluctuant field (around 40°), however the temperature starts a substantially decreasing at this point.

The maximum value of the normalized local heat transfer coefficient, $h_\phi/\bar{h}$, or its equivalent ΔNu_θ appears at the same location as the minimal temperature (Fig. 54 (b)). The position of the maximum of the $h_\phi/\bar{h}$ (or ΔNu_θ) is around ϕ = 80°. Chang and Tavoularis (2008) obtained similar results in their numerical study for a single-rod in a rectangular channel. The lowest temperatures take place about 70° and 80° (far from the gap vicinity, 0°), the same regions where the maximum Nusselt number is found. This can be explained by observing the average axial velocity distributions (Fig. 45 a-d), whose its maximum values coincide with the angular position of the highest Nusselt numbers and, therefore, the lowest temperature. The maximum values for ΔNu_θ ranged from 1.05 up to 1.10 for *W*/*D* = 1.050 between 1.200. Moreover, the present results are in quite good agreement with the numerical results provided by Chang and Tavoularis (2007) and (2008), in spite of the Reynolds number difference between their computations and this work. The uncertainty associated to the convective heat transfer is in Appendix 3.

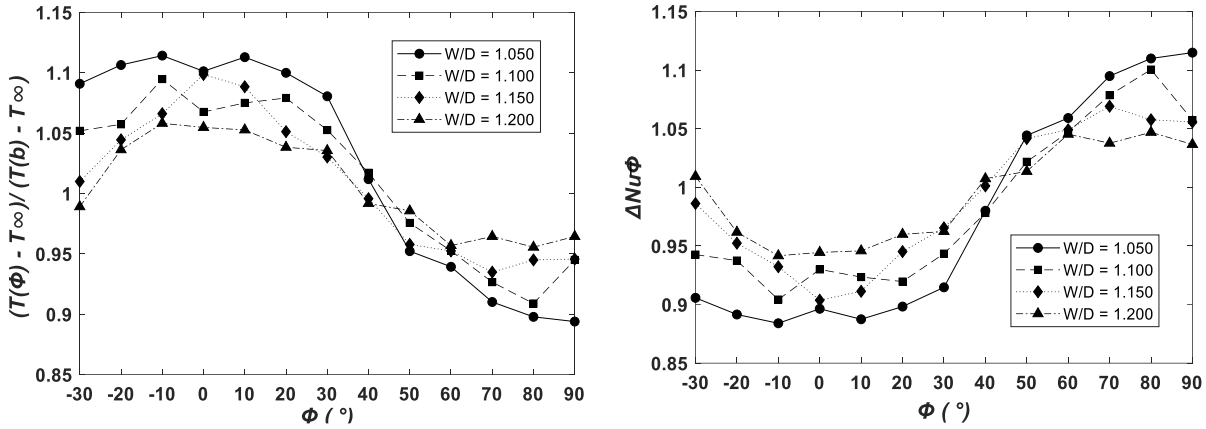

(a) (b)

Figure 54 (a) Circumferential distribution of the wall temperature. (b) Nusselt number as a function of the angular position.

Groeneveld (1973), Guellouz and Tavoularis (1992) and Guellouz (1998) presented their measurements and/or compilation of measurements in the form of *J*-factor defined as $J = h_{min}/\bar{h}$, where h_{min} is the minimum heat transfer coefficient around the rod for a rod bundle type arrangement and $\bar{h}$ is the average convective heat transfer around the rod. Figure 55 shows the *J*-factor obtained from the measurements of the present work, along with the results provided by Guellouz and Tavoularis (1992) (also shown in the *J* format in Guellouz, 1998), the experimental data of Markoczy (1966), Hoffman et al., (1970) and Berger & Ziai (1982). The present *J*-factor results are in good agreement with those brought by the authors mentioned above. Moreover, considering the approach in Guellouz (1998), an exponential function (eq. 16) of the *W*/*D* – ratio was fitted through all the *J*-factor points, including the measurements of the present work, where *C1* = 0.8718; *C2* = -0.4133; *C3* = -0.2596 and *C4* = -41.2. This exponential function, as shown in Fig. 55, is a good representation of the data points. The *J*-factor, as shown in Fig. 55, increases with the W/D.

$$J = C_1 e^{C_2[(W/D)-1]} + C_3 e^{C_4[(W/D)-1]} \tag{16}$$

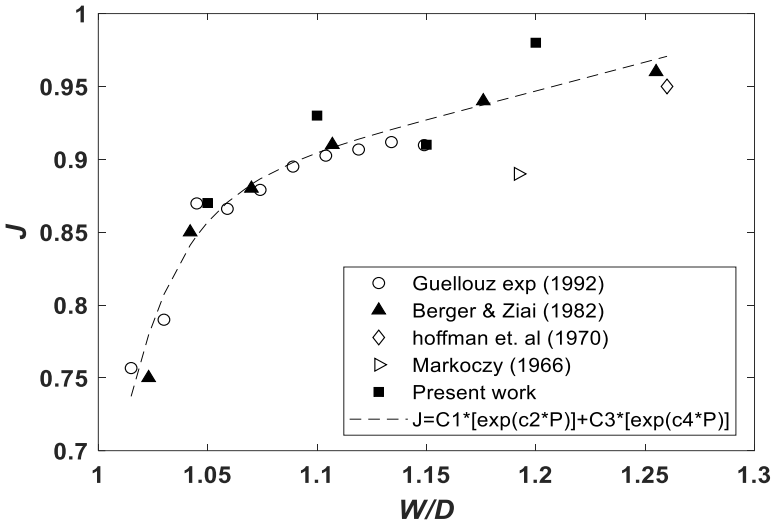

Figure 55 *J*-factor in terms of the *W*/*D* – ratio.

5.6 Skin Friction Distribution

Shear stress, τ_w, was experimentally obtained. These values were normalized by the dynamic pressure, using the air density, ρ, and the bulk velocity, U_b, to determine the Skin friction coefficient, C_f, shown in eq. (17).

$$Cf = \frac{\tau_w}{\frac{1}{2}\rho U b^2} \tag{17}$$

Figure 56 shows the skin friction distribution around the rod. The uncertainties associated to the skin friction are in Appendix 3.

The shear stress was measured starting from the opposite subchannel to verify the symmetry over the interval -30°< ϕ < 30°, similar to what was done for the temperature and the convective heat transfer coefficient. This symmetry could be demonstrated, as shown in Fig. 56. The Skin friction coefficient, C_f, varied monotonically with the gap width, although with different rate of changes. The skin friction coefficient, for all angular positions, decreases as the *W*/*D* – ratio decreases. This behavior was also observed by Guellouz and Tavoularis (2000a). The difference between the measurements of *W*/*D* = 1.100 and 1.150 is much smaller in comparison with the difference between the widest gap sizes. The highest values of

C_f are located far from the gap, between 70° and 80°, while the lowest values can be found around -10° and 0° (exactly inside the narrow gap). The maximum C_f observed was for W/D = 1.200, at 80°, and is 47% higher than the maximum occurred for W/D = 1.050. The lowest C_f of all the experiment was observed for W/D = 1.050 at -10° (gap vicinity).

The C_f values of the present work found in the narrow gap for W/D = 1.050 and 1.100 are 0.0042 and 0.0047, respectively. These values are in good agreement with the results of Guellouz and Tavoularis (2000a) and Chang and Tavoularis (2008) for the same gap spacings, who found values around 0.004 and 0.005. For the highest gaps, W/D = 1.150 and 1.200, the C_f of this work was 0.0062 and 0.0081, respectively. Guellouz and Tavoularis (2000a) found C_f of 0.0058 and 0.006 in the narrow gap for W/D = 1.150 and 1.200, respectively, what is a little smaller than the data of the present work.

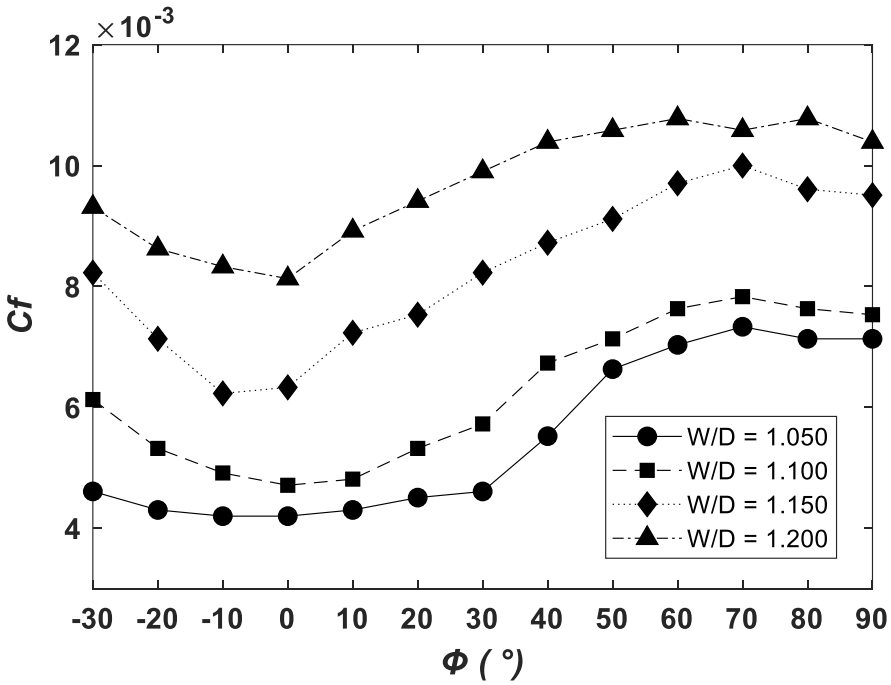

Figure 56 Skin friction (C_f) around the rod for W/D = 1.050, 1.100, 1.150 and 1.200.

5.7 Stanton Number and the Reynolds-Colburn Analogy

The Reynolds-Colburn analogy is based on the relationship between the turbulent momentum and the heat transfer, as explained by Çengel and Ghajar (2011), and is expressed in terms of the Stanton number, the skin friction coefficient and the Prandlt number, as follows

$$Stn_{\phi} = \frac{h_{\phi}}{\rho C_p U b}$$

$$Stn_{\phi}\,\mathrm{Pr}^{2/3} = \frac{C_{f\phi}}{2} \tag{18}$$

Pr is the Prandlt number, equal to 0.71 for air at the experimental conditions, and C_p is the specific heat of the fluid at 22°*C*. The Reynolds-Colburn analogy was computed in order to present an alternative way to assess the convective heat transfer.

A linear relationship between the local Stanton number and the local skin friction (C_f) for all studied *W*/*D* – ratios was observed in Fig. 57. However, it is possible to see the data scattering as the gap size becomes wider. The R^2 for *W*/*D* = 1.050, 1.100, 1.150 and 1.200 was 0.98, 0.89, 0.92 and 0.78, respectively. This parameter demonstrates the scatter increasing as the *W*/*D* becomes wider and shows that in the worst case, *W*/*D* = 1.200, 78% of the variation is explained by the relationship between the Stanton number and the Reynolds-Colburn analogy. The values of the slope and the intercept are different from those given by the analogy, who should be 1.0 and 0.0, respectively. Figure 57 also showed that the slope decreases as the *W*/*D* – ratio increases. This difference can be due to the fact that the entire channel bulk velocity is used to determine the skin friction coefficient and the Stanton number. So, a local velocity, at the respective angular position, could be more appropriate. However, these results are important, because the local skin friction coefficient is much easier to measure than the local heat transfer, h_{Φ}. If a reliable fit is used, the local heat transfer can be easily determined from the skin friction data.

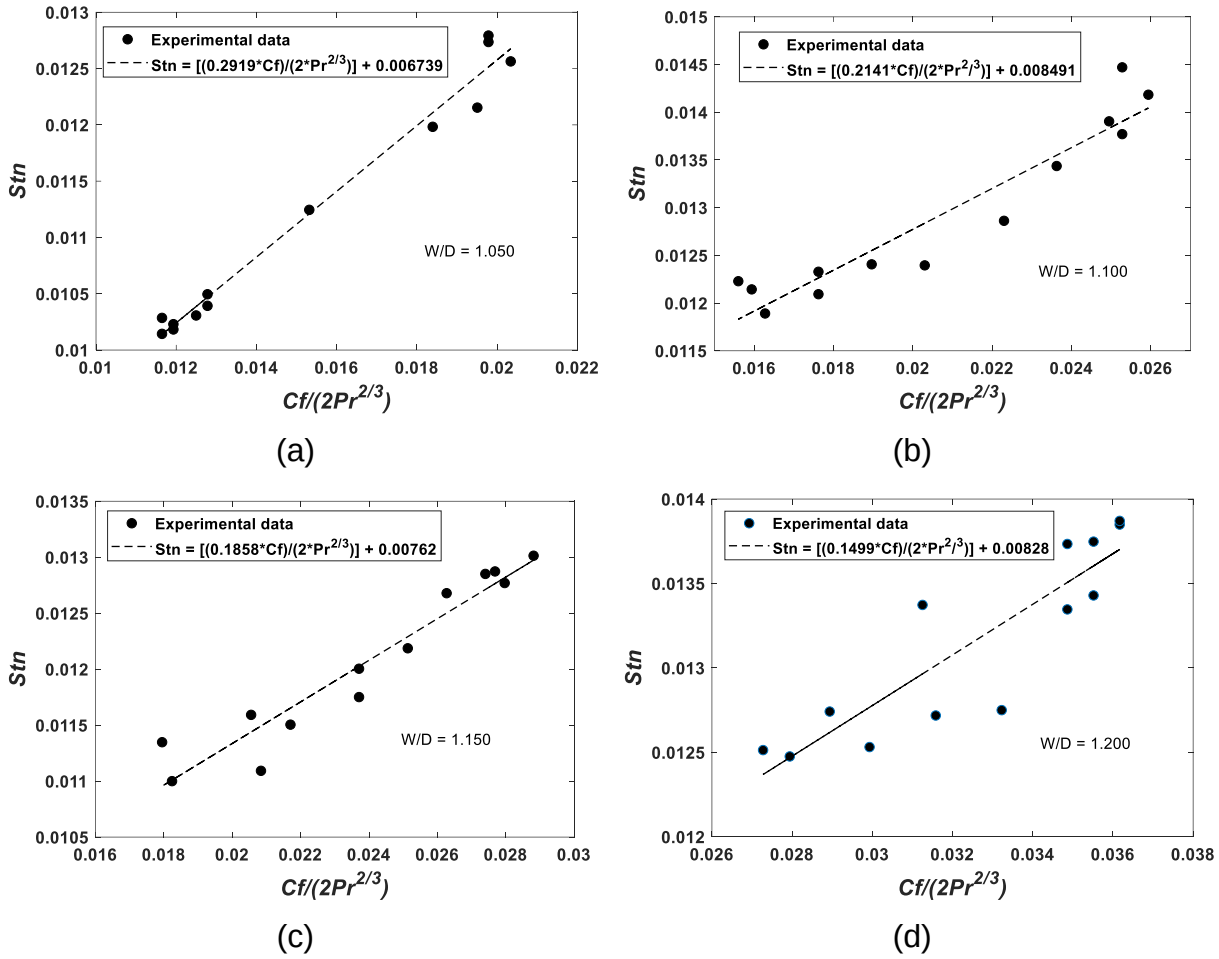

Figure 57 Reynold-Colburn analogy based on the half channel's bulk velocity. (a) *W*/*D* = 1.050. (b) *W*/*D* = 1.100. (c) *W*/*D* = 1.150. (d) *W*/*D* = 1.200.

As an attempt to obtain a more faithful representation, local bulk velocities were obtained for the position 0° up to 90° to recalculate the Stanton number and the Reynolds-Colburn analogy. In this sense, the half channel's cross section was divided from 0° up to 90°, afterwards, the corresponding local bulk velocities, associated to different angular positions, are calculated. The scheme of how the channel was divided is shown in Fig. 58.

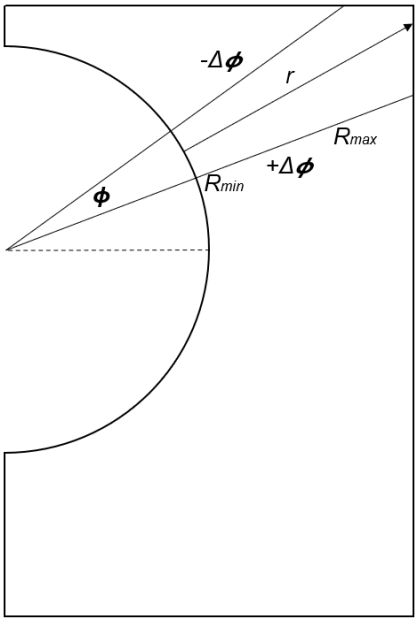

Figure 58 Scheme of division for each angular position.

The points of velocities obtained for each angular position (Fig. 58) were fitted using eq. (19), as follows

$$\frac{u}{U_{\max}} = a\left(\frac{r - R_{\min}}{R_{\max} - R_{\min}}\right)^{(1/n)} \tag{19}$$

where u is the local velocity of a determined angular position, $U_{\max}$ is the maximum velocity of a determined angular position, r is the locus of a determined velocity, R_{min} and R_{max} are the locus of the minimum and maximum velocities for a specific angular position, respectively. The a ranged from 0.9451 up to 1.027 and n from 7 up to 156.27. The eq. (19) form was chosen to fit the velocity points, because the velocity profile for a circular pipe presented by Schlichting (1974) has the same form, as follows

$$\frac{u}{U} = \left(\frac{y}{R}\right)^{(1/n)} \tag{20}$$

So, by integrating eq. (19), the local bulk velocities, U_{bL}, can be obtained, as follows

$$U_{bL} = \frac{2U_{\max} a}{R_{\max} + R_{\min}} \left[\frac{n}{2n+1} (R_{\max} - R_{\min}) + \frac{n}{n+1} R_{\min} \right] \quad (21)$$

The mathematical manipulation to find eq. (18) is detailed in Appendix 4. Figure 59 shows the Reynolds-Colburn analogy for the positions 0° up to 90° calculated using the local bulk velocity, U_{bL}. The new values of the analogy reinforced the linear relationship between the Stanton number and the skin friction, especially for wider gaps, *W*/*D* = 1.100, 1.150 and 1.200. The data scattering was seen using the bulk velocity no longer appears, mainly in wider gaps (Fig. 57). This improvement in the scattering is corroborated by the increasing of R^2, which was 0.99, 0.99, 0.94 and 0.93 for *W*/*D* = 1.050, 1.100, 1.150 and 1.200, respectively. Further, the slope of the curves increases as *W*/*D* decreases, however, a puzzling result can be observed in the cases of *W*/*D* = 1.050 and 1.100. The slope of the fitted curves is higher in comparison to the previous analogy (Fig. 57) and the intercept is still not 0.0. Despite that, it could be observed some improvement of the analogy, mainly in the scattering of the data. All the local bulk velocities calculated are summarized in Appendix 4.

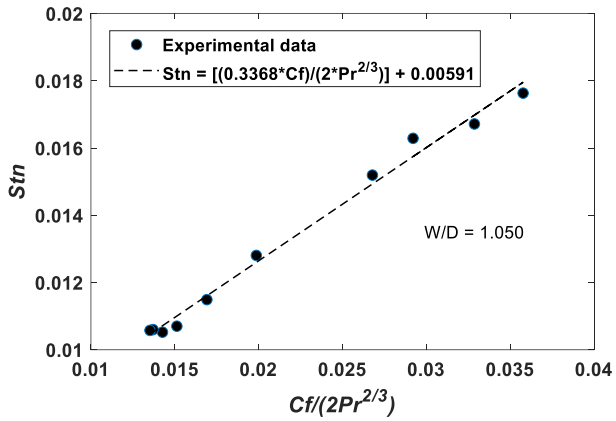

(a)

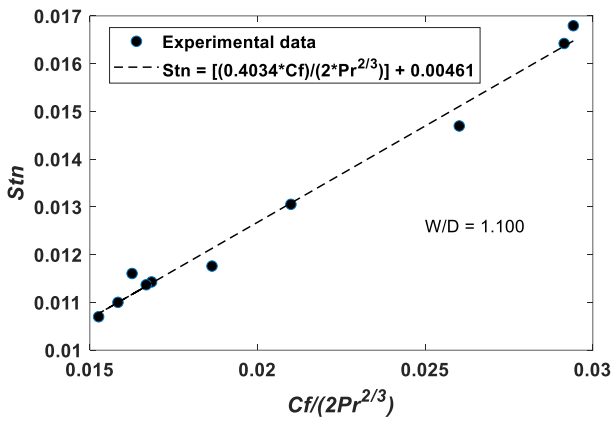

(b)

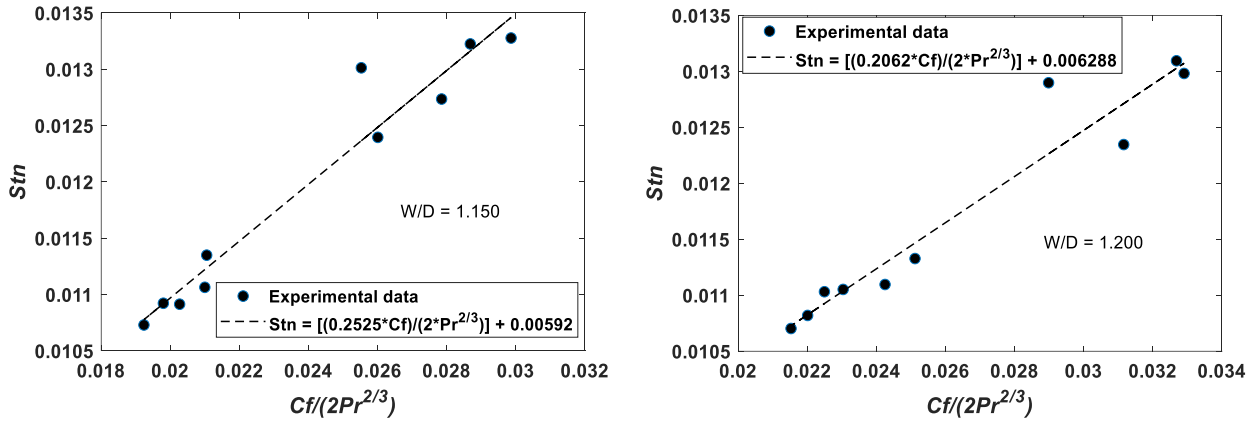

Figure 59 Reynolds-Colburn analogy calculated using U_{bL} .a) *W*/*D* = 1.050. a) *W*/*D* = 1.100. a) *W*/*D* = 1.150 a) *W*/*D* = 1.200.

6 CONCLUSION

The present work aimed to investigate the influence of the gap spacing, *W*/*D*, on the flow dynamics and on the convective heat transfer in a compound channel containing a cylindrical rod inside. Therefore, the temperature distributions and Nusselt number around the rod's surface were assessed. The mean axial velocity, velocity's fluctuations and the spectrum of the flow were also target of this work. The test section consisted in a main rectangular channel containing a rod inside. The rod was heated by a cell powered by a cartridge electrical resistance. The hot-wire anemometry was the measurement technique to gather the average axial velocity and its fluctuations. It was possible to investigate the wall temperature, Nusselt number and the skin friction for *W*/*D* = 1.050, 1.100, 1.150 and 1.200. Also, it was allowed to examine the Reynolds-Colburn analogy. The experiments were performed for Reynolds numbers around 40000 the work fluid was air.

The mean axial velocity distributions are in qualitatively good agreement with those obtained by previous authors. The maximum value observed in *W*/*D* = 1.050, 1.110 and 1.200 was $\overline{U}/U_b$ = 1.30. However, for *W*/*D* = 1.150, the maximum value was a little lower in comparison to the values found for the other gaps, $\overline{U}/U_b$ = 1.20. The lower velocity values were found around the gap vicinity and the highest velocities occurred at the subchannel's widest region. The isocountours were seen to bulge towards the corners, as a consequence of the secondary flows. These characteristics are normally seen in compound channels.

The *u*-RMS distributions were measured for all *W*/*D* – ratios. The lowest value observed for *u*-RMS was $\sqrt{\overline{u'^2}}/U_b$ ~ 0.06, taking place in the subchannel's centre due to the fact that the fluctuation filed is no longer affected by *W*/*D* – ratio nor the lateral walls. The maximum values occurred near the narrow gap and were around $\sqrt{\overline{u'^2}}/U_b$ ~ 0.12 and 0.14, roughly at 40°, this have been already reported in the previous literature. The presence of a closed contour in *u*-RMS near the narrow gap is a striking characteristic of the presence of coherent vortices, especially for *W*/*D* = 1.050 and 1.100. In the narrow gaps of the of *W*/*D* = 1.150 and 1.200, it was not observed contours with high *u*-RMS.

The spectral analysis was performed at different distances from the gap centre (z/D), showing that the dynamic of the flow presented very pronounce peaks in the spectra, assigning a very well-marked frequency at the gap vicinity.

For the closed rod, pronounced peaks were observed in the spectra up to z/D = 0.30 for W/D = 1.050 and 1.100. This indicates the presence of large-scale coherent structures in the region. These turbulent structures are strongly responsible for the mixing process and energy transport in subchannels connected by narrow gaps. However, no significant frequency peaks were found for W/D = 1.150 and 1.200. The Strouhal numbers calculated for the measurements in the closed rod are higher than those found in the open literature. However, experiments using a hollow rod yielded, for W/D = 1.050 and 1.100, Strouhal numbers equal to 0.20 and 0.23. These values are closer to the literature values. The differences in terms of frequency and Strouhal numbers between the non-empty rod and the hollow rod may be associated to reduction of the flow passage promoted by the non-empty rod, producing a mass flow redistribution and, therefore, affecting the dynamics of the flow filed.

The measured temperature and Nusselt number distributions showed excellent agreement with previous researchers. The temperatures presented a significant decreasing at 40° (location of the highest energy of the fluctuant field). The Nusselt number showed an essentially symmetric behaviour and, regardless the W/D – ratio, had its lowest value near the narrow gap centre and its highest facing the core of the subchannel, around 80°. As the W/D decreases, the Nusselt number also decreases, mainly near the gap region. The J-factor calculated from the experimental results of the present work was in fair agreement with the data presented by other authors.

The distribution of the skin friction (C_f) coefficient was quite similar to that the Nusselt number. The skin friction seems to be very sensitive to the increase of gap spacing. The maximum C_f for W/D = 1.200 is 47% higher than the maximum value for W/D = 1.050.

Based on these values of the skin friction and the measured values of the heat transfer, the Reynolds-Colburn analogy was examined. Regardless of the gap width, a linear relationship between the Stanton number and the skin friction was obtained. The Reynolds-Colburn analogy may be used as an alternative way to determine the

Nusselt number, once the local skin fricition coefficient is easier to measure than the convective heat transfer coefficient.

The Reynolds-Colburn analogy calculated using local bulk velocities showed a substantial reduction in the scatter of the data in comparison to the values computed using a bulk velocity for the entire channel. However, slope of the curve was not improved, getting closer to the expected value. The improvement in the data scattering is a clear indication that the flow dynamics in the gap vicinity is strongly influenced by local variables.

7 REFERENCES

Biemüller, M., Meyer L., Rehme, K. 1996. “Large eddy simulation and measurement of the structure of turbulence in two rectangular channels connected by a gap”. In: Heraklion, G.R., Rodi, W. (Publ.), *Proc. 3rd Internat. Symp., Eng. Turbulence Modelling and Experiments*, Elsevier, Amsterdam [u.a.], 249–258.

Berger, F.P. and Ziai, A. 1982. “The effect of displacement and bowing in rod clusters on local heat transfer characteristics”. “Proc Conf “Gas Cooled Reactors Today”. 3. P 217-222.

Candela, D. C. S., 2019. “Numeric simulation of developing turbulent flow in eccentric channels – effect of the velocity fluctuations on the convective heat transfer”. *Dissertação de Mestrado em Integridade de Materiais da Engenharia, Faculdade UnB/FT/Universidade de Brasília*, DF, 83 p.

Candela, D. S., Gomes, T. F., Goulart, J. N. V., Anflor, C. T. M., 2020. “Numerical simulation of turbulent flow in an eccentric channel”. *European Journal of Mechanics / B Fluids*. (83), 86-98.

Carajilescov, P., Todreas, N.E. 1976. “Experimental and analytical study of axial turbulent flows in an interior subchannel of a bare rod bundle”. *J. Heat Transfer, Trans*. ASME, 262–268 p-p.

Chang, D., Tavoularis, S., 2005. “Unsteady numerical simulations of turbulence and coherent structures in axial flow near a narrow gap”. *Trans*. ASME 127, 458–466.

Chang D., & Tavoularis, S. 2006. “Convective heat transfer in turbulent flow near a gap”. *Journal of Heat Transfer*, Vol. 128, 701-708.

Chang, D., & Tavoularis, S. 2007. “Numerical simulation of turbulent flow in a 37-rod bundle”. *Nuclear Engineering and Design*, 237(6), 575-590.

Chang, D., Tavoularis, S. 2008. “Simulations of turbulence, heat transfer and mixing across narrow gaps between rod-bundle subchannels”. *Nuclear Engineering and Design*, 238(1), 109-123 p-p.

Choueiri, G., & Tavoularis, S. 2014. “Experimental investigation of flow development and gap vortex street in an eccentric annular channel. Part 1. Overview of the

flow structure". *Journal of Fluid Mechanics,* Vol 752, 521-542. doi:10.1017/jfm.2014.343.

Comte-Bellot, G. 1976. "Hot-wire anemometry". *Annual review of fluid mechanics*, 8(1), 209-231.

Çengel, Y. A. & Ghajar, A. J. 2011. "Heat and mass transfer: Fundamentals and applications". 4th Ed. The McGraw-Hill Companies. New York, USA.

Dittus, F.W., Boelter, L. M. K. 1930. "Heat Transfer in automobile radiators of the tubular type". Univ. Ca. Berkley Publi Eng. 2 443-461.

Duan, Y., & He, S. 2017. "Heat transfer of a buoyancy-aided turbulent flow in a trapezoidal annulus". *International Journal of Heat and Mass Transfer*, 114, 211-224.

Gosset, A., & Tavoularis, S. 2006. "Laminar flow instability in a rectangular channel with a cylindrical core". *Physics of Fluids*, 18 (4), 0441081-8.

Goulart, J., Noleto, L., & Möller, S. V. 2014. "Experimental study of mixing layer in a closed compound channel". *Journal of the Brazilian Society of Mechanical Sciences and Engineering*, 36(2), 411-420.

Goulart, J., Wissink, J.G., Wrobel, L.C. 2016. "Numerical of turbulent flow in a channel small slot". *Int. Journal of Heat and Fluid Flow*. (61), 343-354.

Guellouz, M.S., Tavoularis, S. 1992. "Heat transfer in rod bundle subchannels with varying rod-wall proximity". *Nucl. Eng. Des*. 132, 351–366.

Guellouz, M. S., 1998. "Turbulent flow and heat transfer in rod bundles". *PhD. thesis, University of Ottawa*, Canada.

Guellouz, M.S., Tavoularis, S. 2000a. "The structure of turbulence flow in a rectangular channel containing a cylindrical rod – Part 1: Reynolds-averaged measurements". *Exp. Thermal and Fluid Sci*, Vol 23, 59-73.

Guellouz, M.S., Tavoularis, S. 2000b. "The structure of turbulence flow in a rectangular channel containing a cylindrical rod – Part 2: phase-averaged measurements". *Exp. Thermal and Fluid Sci*, Vol 23, 75-91.

Groeneveld, D.C. 1973. "Forced convective heat transfer to superheated steam in rod bundles". *AECL Report, AECL – 4450*, Chalk River, Ontario. Canada.

Harbaoui, M., & Guellouz, M.S. 2006. “Large scale structures in laminar flow through two parallel fins”. *Proceedings of the 3rd International Conference on Advances in Mechanical Engineering and Mechanics*, Hammamet, Tunisia.

Hofmann, G. 1964. “Qualitative investigation of local heat transfer coefficients in a 7-rod bundle”. *Report No. 13*, Institüt für Reaktorbauelemente, Kernforschungzentrum Karlsruhe, Germany, June, (in German – unpublished).

Hoffman, H. W., Kidd Jr, G. J., Lynch, F. E., Stelzman, W. J., Wantland, J. L., & Sogin, H. H. 1970. “Experimental studies of the heat transfer and fluid dynamic characteristics of rod-cluster-type nuclear reactor fuel elements” (No. ORNL-4356). Oak Ridge National Lab., Tenn.

Holloway M., Conover T., McClusky H., Beasley D., Conner M., 2005. “The Effect of Support Grid Design on Azimuthal Variations in Heat Transfer Coefficient for Rod Bundles”. *Journal of Heat Transfer*, vol. 127, 598-605.

Hooper, J.D., 1980. “Developed single-phase turbulent flow through a square-pitch rod cluster”. *Nucl. Eng. Des*. 60, 365–379.

Hooper, J.D., Rehme, K. 1984. “Large-scale structural effects in developed turbulent flow through closely spaced rod array”. *J. Fluid Mech*. 145. 305-337.

Koched, A., & Guellouz, M.S. 2008. “Large scale coherent structures in laminar compound open channel flows”. *Proceedings of the 4thInternational Conference on Advances in Mechanical Engineering and Mechanics*, Sousse, Tunisia.

Krauss, T., and Meyer, L. 1996. “Characteristics of Turbulent Velocity and Temperature in a Wall Channel of a Heated Rod Bundle”. *Exp. Therm. Fluid Sci*., 12, 75–86.

Krauss, T., Meyer, L., 1998. “Experimental investigation of turbulent transport of momentum and energy in a heated rod bundle”. *Nucl. Eng. Des*. 180, 185–206.

Markoczy, G. 1966. “Heat Transfer in gas cooled clusters”. *EAES Heat Transfer Symposium on Superheated Steam or Gas.* Bern, Switzcrland.

Melo, T., Goulart, J. N., Anflor, C. T., Santos, E. 2017. “Experimental investigation of the velocity time-traces of the turbulent flow in a rectangular channel with a lateral slot”. *European Journal of Mechanics-B/Fluids*, 62, 130-138.

Merzari, E., Wang, S., Ninokata, H. & Theophilis, V. 2008b. “Biglobal linear stability analysis for the flow in eccentric annular channels and a related geometry”. *Physics of Fluids*, 20, 104-114.

Meyer, L., 1991. “Measurements of turbulent velocity and temperature in a central channel of a heated rod bundle”. Kernforschungszentrum.

Meyer, L., Rehme, K. 1994. “Large scale turbulence phenomena in compound rectangular channels”. *Exp. Thermal Fluid Sci*. 8, 286–304.

Meyer, L., Rehme, K. 1995. “Periodic vortices in flow through channels with longitudinal slots or fins”. *10th Symp. Turbulent Shear Flows*, The Pennsylvania State University, vol. 1, University Park, PA, August 14–16, 1–55.

Moffat, R. J. 1988. “Describing the uncertainties in experimental results”. *Experimental thermal and fluid science*, 1(1), 3-17.

Möller, S.V. 1991. “On phenomena of turbulent flow through rod bundles”. *Exp. Therm. Fluid Sci*. V 4, 25-35.

Möller, S.V. 1992. “Single-phase turbulent mixing in rod bundles”. *Experimental Thermal and Fluid Science*, Vol 5, 26-33 p-p, ISSN 0894-1777.

Moradi, H. V. & Tavoularis, S. 2019. “Flow instability in weakly eccentric annuli”. *Phys. Fluids*, 31, 044104; https://doi.org/10.1063/1.5088992.

Ota, T., Kimura, S., Kiwata, T., Komatsu, N. & Kono, T. 2013. “Experimental confirmation of the calibration curves for Preston’s Method”. *4th International Conference on Jets, Wakes and Separated Flows*. Nagoya, Japan.

Palmer, L. D., & Swanson, L. L. 1961. “Measurements of heat-transfer coefficients, friction factors, and velocity profiles for air flowing parallel to closely spaced rods”. (No. GA-1787). General Dynamics Corp., San Diego, CA (United States). General Atomic Div.

Piot, E. & Tavoularis, S. 2011. “Gap instability of laminar flows in eccentric annular channels”. *Nuclear Engineering and Design*, 241 (11), 4615-4620.

Rowe, D.S., 1973. “Measurement of turbulent velocity, intensity and scale in rod bundle flow channels”. *PhD. Thesis, Oregon State University*, BNWL-1736, Battelle Pacific Northwest Laboratories, Richland, Washington.

Rowe, D.S., Johnson, B.M. & Knudsen, J.G., 1974. “Implications concerning rod bundle crossflow mixing based on measurement of turbulent flow structure”. *Int. J. Heat Mass Transfer*. V 17, 407- 419.

Schlichting, H. 1974. “Boundary-Layer Theory”. 6th Ed. McGraw-Hill. Taiwan, Republic of China.

Seale, W.J., 1979. “Turbulent diffusion of heat between connected flow passages. Part 1 and 2”. *Nucl. Eng. Des*. 54, 183–209.

Seale, W. J. 1981. “The effect of subchannel shape on heat transfer in rod bundles with axial flow”. *International Journal of Heat and Mass Transfer*, 24(4), 768-770.

Severino, H. A. M. 2018. “Caracterização numérica/experimental do escoamento turbulento em um canal contendo um duto circular”. *Dissertação de Mestrado em Integridade de Materiais da Engenharia, Faculdade UnB/FT/Universidade de Brasília*, DF, 102 p.

Severino, H. A. M., Melo, T. & Goulart, J.N.V., “Hot wire anemometry and numerical simulation applied to the investigation for the turbulence in a gap flow”. *6th European Conference on Computational Mechanics (ECCM 6) and 7th European Conference on Computational Fluid Dynamics (ECFD 7) – ECCOMAS 2018*. Glasgow, UK.

Souissi, F., Guellouz, M. S., Ben Salah, N. & Kaddeche, S. 2020. “The flow structure in the narrow gaps of compound channels: a linear stability analysis”. *International Journal of Computational Fluid Dynamics*, 34:1, 14-24, DOI: 10.1080/10618562.2019.1690141.

Tavoularis, S. & Chang, D. 2007. “Inter-subchannel mixing across vary narrow gaps in rod bundles”. *15th International Conference on Nuclear Engineering*. Nagoya Japan.

Tavoularis, S. 2011. “Rod bundle vortex networks, gap vortex streets, and gap instability: A nomenclature and some comments on available methodologies”. *Nuclear engineering and design*, 241(7), 2624-2626.

Trupp, A.C. & Azad, R.S. 1975. “The structure of turbulent flow in triangular array rod bundles”. *Nucl. Eng. Des*. 32, 47–84.

Van der Ros, T. & Bogaardt, M., 1970. “Mass and heat exchange between adjacent channels in liquid-cooled rod bundles”. *Nucl. Eng. Des*. 12, 259–268.

White, F. M. 1999. “Fluid Mechanics”. 4th Ed. McGraw-Hill. USA.

Wu, X. & Trupp, A. C. 1993. “Experimental study on the unusual turbulence intensity distributions in rod-to-wall gap regions”. *Experimental thermal and fluid Science*. 6 (4), 360- 370.

Wu, X., Trupp, A. C. 1994. “Spectral measurements and mixing correlations in a simulated rod bundles subchannels”. *Int. J. Heat Transfer*. 6 (4), 1277- 1281.

8 FUTURE WORKS

In this section will be suggested some new tasks to be done in the future in order to deepen the analysis:

- Find a way to use the hot-wire probe the measure in the azimuthal direction
- Measure the azimuthal component of the mean average velocity and *u*-RMS velocities. This can give more detailed explanation about heat transfer in the narrow gap
- Perform the temperature, convective heat transfer coefficient and skin friction measurements for the hollow rod, the same done for the closed rod.

APPENDIX 1 – HOT-WIRE ANEMOMETRY CALIBRATION

Table 2 shows the data gathered during the calibration of the hot-wire probe. The reference velocity was measured by a Pitot tube (Fig. 35) and a pressure transducer. The Table shows in addition to the reference velocity, the anemometer voltage, the data necessary for King's Law, the calculated velocity and its corresponding error. The maximum error between the measured velocity and the calculated velocity was 2.903%. Figure 60 shows the voltage, E, and the measured velocity, U_r. These variables allowed to determine B and n from King's Law.

Table 2 Hot-wire probe calibration.

Eo = 1.2601	B = 0.793031565
	n = 0.525007023

Ur (m/s)	E (V)	ln (E^2-E_0^2)	ln (Ur)	Uc (m/s)	Error (%) 100*((1-Uc)/Ur)
2.249	1.668	0.1781	0.811	2.184	2.903
3.516	1.768	0.4323	1.257	3.544	0.770
4.800	1.845	0.5983	1.569	4.862	1.277
6.137	1.911	0.7248	1.814	6.186	0.813
7.384	1.968	0.8264	1.999	7.507	1.670
8.775	2.022	0.9176	2.172	8.932	1.786
9.974	2.061	0.9788	2.300	10.037	0.625
11.196	2.101	1.0400	2.416	11.276	0.718
12.590	2.137	1.0928	2.533	12.470	0.955
13.865	2.171	1.1405	2.629	13.655	1.511
15.069	2.201	1.1808	2.713	14.744	2.159

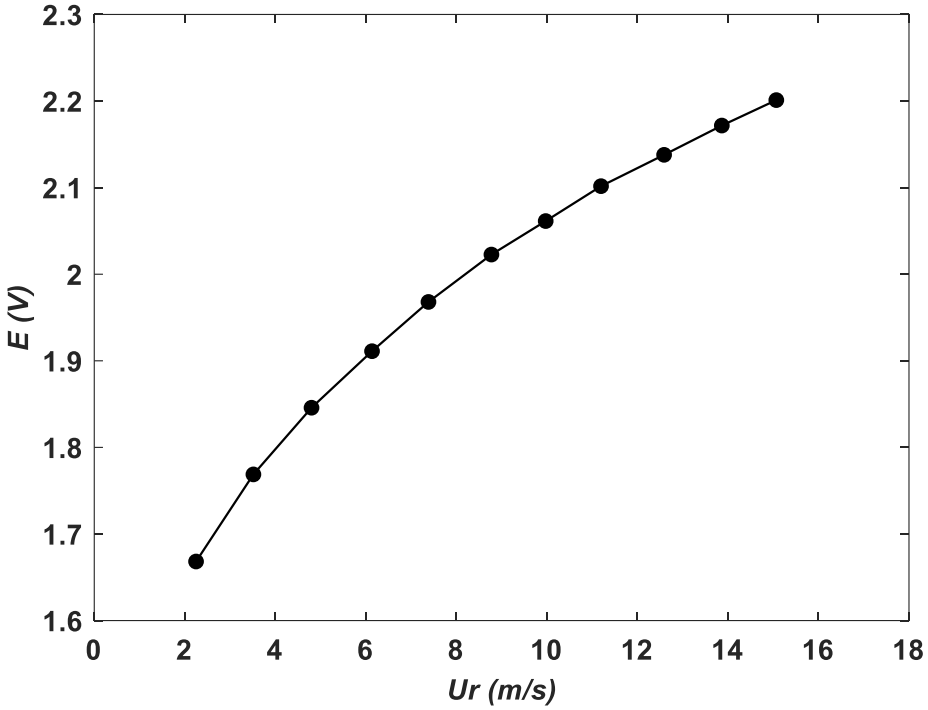

Figure 60 Relationship between voltage (*E*) and measured velocity (*Ur*) obtained during the calibration process.

APPENDIX 2 – PRESTON'S TUBE CALIBRATION

Table 3 presents the equation used in the calibration process and Table 4 shows the values measured and calculated from the calibration. It was measured the pressure drop, ΔP, the normalized pressure drop, ΔP^+, the normalized wall shear stress, τ^+, and the wall shear stress, τ_W. Figure 61 shows the calibration curve, where the normalized wall shear stress is a function of the normalized pressure drop.

Table 3 Equations used in the Preston's tube calibration process.

Pressure drop (ΔP) / Differece between the Preston's tube and the static pressure (ΔP^+)	$\Delta P, \Delta P_{Preston} = 29.308(3.94 - I)$ [Pa]
Balance equation between the wall shear and pressure drop. (Fully developed and incompressible flow)	$\frac{\tau_w d_p}{4\rho\upsilon^2} = f\left(\frac{\Delta P_{Preston} d_p^2}{4\rho\upsilon^2}\right)$ [Pa]
Wall shear stress (τ_w)	$\tau_w = \frac{D_p \Delta P}{4L_{SP}}$ [Pa]
Normalized wall shear stress (τ^+)	$\tau^+ = \frac{\tau_w d_p}{\rho\upsilon^2}$ [Dimensionless]
Normalized pressure difference (ΔP^+)	$\Delta P^+ = \frac{\Delta P d_p^2}{\rho\upsilon^2}$ [Dimensionless]

Table 4 Measured and calculated values from the Preston's tube calibration.

f (Hz)	(Pipe) *I (mA)*	*ΔP (Pa)*	(Preston's tube) *I (mA)*	$\Delta P_{Preston}$ *(Pa)*	ΔP^+	τ_w	τ^+
7.15	4.14	5.8616	4.05	3.22388	5.49E+04	0.064576949	1.10E+03
14.3	4.31	10.84396	4.2	7.62008	1.30E+05	0.119467356	2.04E+03
21.45	4.54	17.5848	4.41	13.77476	2.35E+05	0.193730847	3.30E+03
28.6	4.92	28.72184	4.72	22.86024	3.90E+05	0.316427051	5.39E+03
35.75	5.22	37.51424	5.02	31.65264	5.39E+05	0.413292475	7.04E+03
42.9	5.62	49.23744	5.4	42.78968	7.29E+05	0.542446373	9.24E+03
50	6.08	62,71912	5.86	56.27136	9.59E+05	0.690973356	1.18E+04

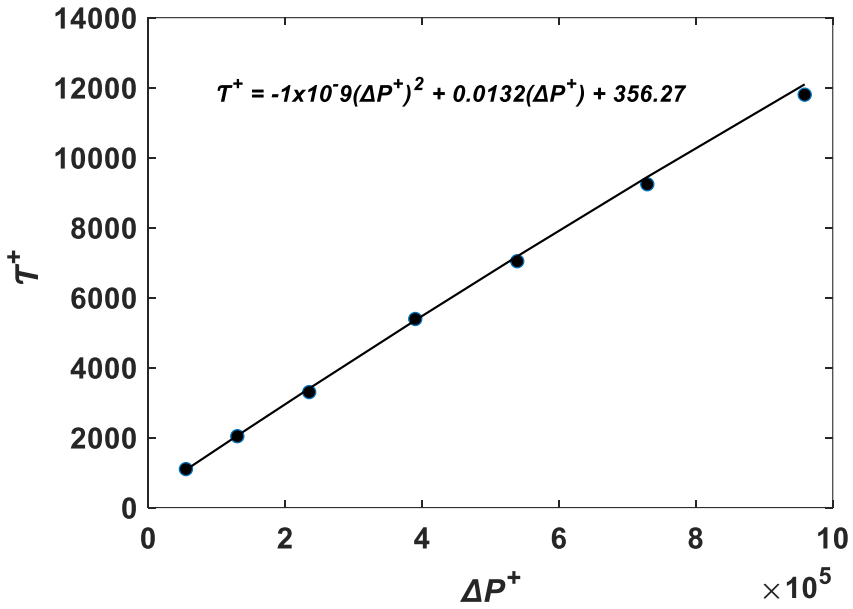

Figure 61 Relationship between the normalized wall shar stress (τ^+) and the normalized pressure drop (ΔP^+) resulted from the Preston's tube calibration process.

APPENDIX 3 – EVALUATION OF THE UNCERTAINTIES

In this work the uncertainties of the experimentally measured results were assessed. The equation due to Moffat (1988), that allow the determination of the contribution of each variable on the uncertainty of the measurements, was used. The equation is given by

$$\delta R = \left\{ \sum_{i=1}^{n} \left(\frac{\partial R}{\partial x_i} \delta x_i \right)^2 \right\}^{1/2} \tag{22}$$

Where $R = R(x_1, x_2, x_3, \ldots, x_n)$ is the analysed results and δx_i is the uncertainty associated with the involved variables x_i. $\frac{\partial R}{\partial xi}$ is the R partial derivative related to x_i, that provides the sensitivity coefficient of R related to x_i.

Evaluation of the Hot-wire anemometry uncertainties

The relationship between the velocity and the anemometer voltage is given by King's Law and is expressed in eq. (23).

$$U = \left(\frac{E^2 - E_o^2}{B} \right)^{1/n} \tag{23}$$

Thus, the hot-wire probe uncertainties would be given by

$$\delta U = \left[\left(\frac{\partial U}{\partial n} \delta n \right)^2 + \left(\frac{\partial U}{\partial B} \delta B \right)^2 + \left(\frac{\partial U}{\partial E_o} \delta E_o \right)^2 + \left(\frac{\partial U}{\partial E} \delta E \right)^2 \right]^{1/2} \tag{24}$$

Based on the uncertainties associated with the different variables, this would yield uncertainties for the velocity ranging from 3.40% up to 15.24%.

Evaluation of the Strouhal number uncertainties

The Strouhal number was determined using eq. (13) and its uncertainty was determined by eq. (25).

$$\delta St = \left[\left(\frac{\partial St}{\partial f} \delta f \right)^2 + \left(\frac{\partial St}{\partial U_b} \delta U_b \right)^2 + \left(\frac{\partial U}{\partial D} \delta D \right)^2 \right]^{1/2} \tag{25}$$

The Uncertainties found for the Strouhal number is 1.13% up to 3.77%.

Evaluation of the Power Spectra Density (PSD) Uncertainties

The mean average statistical error of the spectra is given by,

$$error = \left(\sqrt{\frac{1}{\frac{F_a}{B_e} t_s}} \right) .100\% \tag{26}$$

Table 5 summarizes the variables employed to obtain the signal treatment by PSD.

Table 5 Data emplyed on the signal treatment by PSD.

Acquisition frequency (F_a)	1000 *Hz*
Number of points	65536
Acquisition time (t_s)	65.536 *s*
PSD block points (B_e)	1024
Bandwidth (F_a/B_e)	0.98 *Hz*
Mean average statistic error (%)	12.5

Evaluation of the Convective heat transfer coefficient uncertainties

Applying eq. (22) to eq. (5) gives the convective heat transfer coefficient uncertainty expression, as follows

$$\delta h_{\phi} = \left[\left(\frac{\partial h_{\phi}}{\partial q_{conv}} \delta q_{conv} \right)^2 + \left(\frac{\partial h_{\phi}}{\partial A_C} \delta A_C \right)^2 + \left(\frac{\partial h_{\phi}}{\partial T_{(1-S)}} \delta T_{(1-S)} \right)^2 + \left(\frac{\partial h_{\phi}}{\partial T_{\infty}} \delta T_{\infty} \right)^2 \right]^{1/2} \quad (25)$$

This yields an uncertainty for the convective heat transfer coefficient of about 20%.

Evaluation of the Skin friction coefficient Uncertainties

The skin friction uncertainty is given by

$$\delta C_f = \left[\left(\frac{\partial C_f}{\partial \tau_w} \delta \tau_w \right)^2 + \left(\frac{\partial C_f}{\partial \rho} \delta \rho \right)^2 + \left(\frac{\partial C_f}{\partial U_b} \delta U_b \right)^2 \right]^{1/2} \quad (26)$$

The uncertainties are calculated to range 6.15% up to 23%.

APPENDIX 4 – LOCAL BULK VELOCITY (U_{BL}) MATHEMATICAL FORMULATION AND DATA

The process to obtain eq. (18) is detailed, as follows

$u^* = \frac{u}{U_{\max}}$ and $\eta = \frac{r - R_{\min}}{R_{\max} - R_{\min}}$

Then: $r = \eta(R_{\max} - R_{\min}) + R_{\min}$ and $\frac{d\eta}{dr} = \frac{1}{R_{\max} - R_{\min}}$

Assume: $u^* = a\eta^{1/n}$ (normally a = 1)

$$U_{bL} = \frac{1}{A}\int_{-\frac{\Delta\phi}{2}}^{+\frac{\Delta\phi}{2}}\int_{R_{\min}}^{R_{\max}} urdrd\phi$$

Where: $A = \iint rdrd\phi = \frac{1}{2}(R_{\max}^2 - R_{\min}^2)\Delta\phi$

$$\iint urdrd\phi = \Delta\phi\int_{R_{\min}}^{R_{\max}} urdr$$

$$= \Delta\phi U_{\max}\int_0^1 u^*[\eta(R_{\max} - R_{\min}) + R_{\min}]d\eta(R_{\max} - R_{\min})$$

$$= \Delta\phi U_{\max}(R_{\max} - R_{\min})a\int_0^1 [\eta^{\left(1+\frac{1}{n}\right)}(R_{\max} - R_{\min}) + \eta^{1/n}R_{\min}]d\eta$$

$$= \Delta\phi U_{\max}(R_{\max} - R_{\min})a\left[\frac{n}{2n+1}(R_{\max} - R_{\min})\eta^{\left(\frac{2n+1}{n}\right)} + \frac{R_{\min}n}{n+1}\eta^{\left(\frac{n+1}{n}\right)}\right]$$

$$= \Delta\phi U_{\max}(R_{\max} - R_{\min})a\left[\frac{n}{2n+1}(R_{\max} - R_{\min}) + \frac{R_{\min}n}{n+1}\right]$$

$$U_{bL} = \frac{\Delta\phi U_{\max}(R_{\max} - R_{\min})a}{\frac{1}{2}(R_{\max} - R_{\min})(R_{\max} + R_{\min})\Delta\phi}\left[\frac{n}{2n+1}(R_{\max} - R_{\min}) + \frac{R_{\min}n}{n+1}\right]$$

Finally: $$U_{bL} = \frac{2U_{\max} a}{R_{\max} + R_{\min}} \left[\frac{n}{2n+1} (R_{\max} - R_{\min}) + \frac{n}{n+1} R_{\min} \right]$$

The local bulk velocities calculated by eq. (18) are summarized in Table 6.

Table 6 Local bulk velocities (U_{bL}) for each *W*/*D* – ratio from 0° up to 90°.

W/*D* = 1.050		*W*/*D* = 1.100		*W*/*D* = 1.150		*W*/*D* = 1.200	
ϕ (°)	Ub_L (m/s)	ϕ (°)	Ub_L (m/s)	ϕ (°)	Ub_L (m/s)	ϕ (°)	Ub_L (m/s)
0	5.35	0	5.65	0	7.03	0	7.48
10	4.90	10	5.74	10	6.95	10	7.38
20	5.23	20	6.39	20	7.23	20	7.55
30	5.86	30	7.37	30	7.67	30	7.96
40	7.45	40	8.49	40	8.18	40	9.08
50	8.84	50	9.48	50	9.29	50	9.33
60	9.63	60	9.99	60	9.60	60	9.66
70	10.12	70	9.63	70	9.92	70	9.90
80	10.19	80	9.66	80	9.98	80	9.88
90	10.26	90	9.49	90	9.79	90	9.90

APPENDIX 5 – CONGRESS PAPERS

Full paper published in the 18th Brazilian Congress of Thermal Sciences and Engineering.

APPENDIX 6 – JOURNAL PAPERS

ISSN 2447-6102

Article

Measurements of convective heat transfer around a single rod bundle for three gap spacing

Kayser, F.M. [1,*], Ferrari, J.M.S. [2] and Goulart, J.N.V. [3]

[1] Group of Experimental and Computational Mechanics — GMEC, University of Brasilia; fabio_mk_66@hotmail.com
[2] Group of Experimental and Computational Mechanics — GMEC, University of Brasilia; jalusaferrari@gmail.com
[3] Group of Experimental and Computational Mechanics — GMEC, University of Brasilia; jvaz@unb.br

* Correspondence: fabio_mk_66@hotmail.com

Received: 06/11/2020; Accepted: 05/12/20; Published: 31/12/2020

Abstract: This work aims to evaluate the experimentally the convective heat transfer coefficient around a single rod bundle under turbulent flow. The single rod bundle is part of a compound channel that is mainly characterized by their dimensionless numbers such as the Reynolds number, and the *W/D* - ratio. The gap width, *δ*, is the distance between the rod and the upper part of the channel. During the experimental campaign, the gap *δ* was changed its width to 5, 10 and 15 mm, yielding a *W/D* = 1.05, 1.10 and 1.15, respectively. The dimension *W* is the sum of the gap width, *δ*, and the cylinder's diameter. The test section length was kept constant, 1800 *mm*. Special heated cell, controlled by a Minipa 3305 Power Supply, was designed in order to keep cell`s surface heated. The temperature on the cell`s surface was acquired through a set of special thermocouples on it. Afterwards, the wall temperature and the local minima in terms of convective heat transfer coefficient around the tube was determine and compared with those ones from the open literature. The J-data were found in fair agreement with those previously published. Moreover, the J-data location was not found in the narrow gap for the smallest W/D studied, but for locations away the gap (0°). When the gap becomes wider, the lowest local $\bar{h}$ returned to the narrow gap position. Hot-wire probe was employed to measure the mean average and the turbulent velocity time traces at the gap vicinity. Coherent structures were seen to dominate the flow at such region, affecting the J-data locus.

Keywords: Nusselt number, Heated cell, Compound channel, Rod bundle, Coherent structures.

Full paper published in RIPE – Revista Interdisciplinar de Pesquisa em Engenharia.
https://periodicos.unb.br/index.php/ripe/article/view/35376

ISSN 2447-6102

Article

Numerical Study of Aerodynamic Coefficients of a Ground Vehicle

Ferrari, J.M.S. [1], Kayser, F.M.[2], Noleto, L.G.[3] and Goulart, J.N.V.[4]

[1] GMEC, Universidade de Brasília; jalusaferrari@gmail.com
[2] GMEC, Universidade de Brasília; fabio_mk_66@hotmail.com
[3] Universidade de Brasília; lucianonoleto@gmail.com
[4] GMEC, Universidade de Brasília; jvazgoulart@gmail.com

Received: 06/11/2020; Accepted: 05/12/2020; Published: 31/12/2020

Abstract: The objective of the present paper is to evaluate the turbulent flow around the Ahmed body immersed in air and to determine its aerodynamic coefficients for different slant angles. The bidimensional non-stationary analysis of an incompressible flow around the Ahmed body is carried out for three different rear angles which are 0°, 10° and 25°. The numerical simulations were performed under the same Reynolds number, Re_L = 94 000, based on the free streamwise velocity, u_∞, the longitudinal length of the Ahmed body, L, and the kinematic viscosity of the work fluid, v. The additional diffusivity caused by the turbulent motion was approached using the Boussinesq's idea through the k-ω SST. In the paper, aerodynamic coefficients of drag and the pressure and velocity fields are presented to characterize the Ahmed body for such slant angles, as well as the flow detachment point, determined through the dimensionless skin friction factor distribution on the body's surface. The results showed that the slant presence affects the skin friction and pressure coefficients. As the slant angle was increased, the portion of pressure drag became more significant in total drag. Skin friction coefficient distribution was first presented for this body. As numerical simulations were compared with available results in open literature and showed agreement, we concluded that it was possible to simulate a problem notably tridimensional with a bidimensional simulation, leading to savings in simulation time and computational cost.

Keywords: Ahmed body. CFD. k-ω SST . Q-criterion. skin friction factor.

Full paper published in RIPE – Revista Interdisciplinar de Pesquisa em Engenharia.
https://periodicos.unb.br/index.php/ripe/article/view/34820/28637

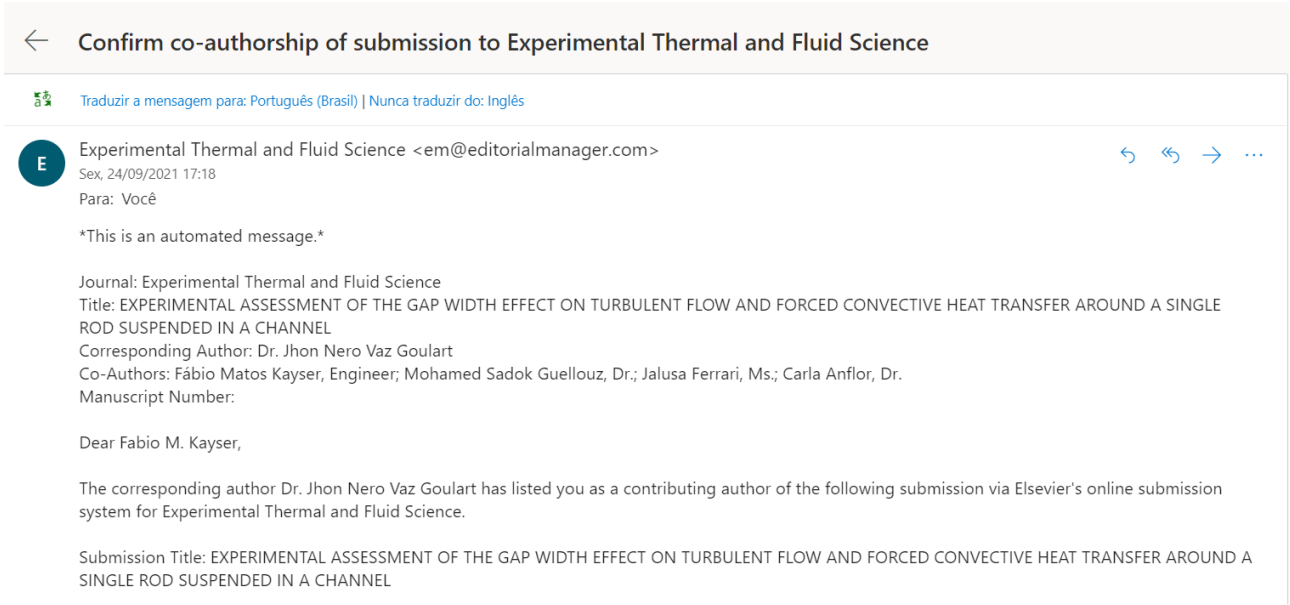

Confirm co-authorship of submission to Experimental Thermal and Fluid Science

Traduzir a mensagem para: Português (Brasil) | Nunca traduzir do: Inglês

E

Experimental Thermal and Fluid Science <em@editorialmanager.com>
Sex, 24/09/2021 17:18
Para: Você

This is an automated message.

Journal: Experimental Thermal and Fluid Science
Title: EXPERIMENTAL ASSESSMENT OF THE GAP WIDTH EFFECT ON TURBULENT FLOW AND FORCED CONVECTIVE HEAT TRANSFER AROUND A SINGLE ROD SUSPENDED IN A CHANNEL
Corresponding Author: Dr. Jhon Nero Vaz Goulart
Co-Authors: Fábio Matos Kayser, Engineer; Mohamed Sadok Guellouz, Dr.; Jalusa Ferrari, Ms.; Carla Anflor, Dr.
Manuscript Number:

Dear Fabio M. Kayser,

The corresponding author Dr. Jhon Nero Vaz Goulart has listed you as a contributing author of the following submission via Elsevier's online submission system for Experimental Thermal and Fluid Science.

Submission Title: EXPERIMENTAL ASSESSMENT OF THE GAP WIDTH EFFECT ON TURBULENT FLOW AND FORCED CONVECTIVE HEAT TRANSFER AROUND A SINGLE ROD SUSPENDED IN A CHANNEL

Full paper submitted to Experimental Thermal and Fluid Science.